

LATERAL CHANNEL CONFINEMENT, TRIBUTARIES, AND THEIR IMPACT ON
CHANNEL MORPHOLOGY

by

AARON ZETTLER-MANN

A DISSERTATION

Presented to the Department of Geography
and the Graduate School of the University of Oregon
in partial fulfillment of the requirements
for the degree of
Doctor of Philosophy

June 2019

DISSERTATION APPROVAL PAGE

Student: Aaron Zettler-Mann

Title: Lateral Channel Confinement, Tributaries, and Their Impact on Channel Morphology

This dissertation has been accepted and approved in partial fulfillment of the requirements for the Doctor of Philosophy degree in the Department of Geography by:

Dr. Mark Fonstad	Chairperson
Dr. Patricia McDowell	Advisor
Dr. Andrew Marcus	Core Member
Dr. Joshua Roering	Institutional Representative

and

Janet Woodruff-Borden	Vice Provost and Dean of the Graduate School
-----------------------	--

Original approval signatures are on file with the University of Oregon Graduate School.

Degree awarded June 2019

© 2019 Aaron Zettler-Mann
This work licensed under a Create Commons
Attribution-NonCommercial-NoDerivatives 4.0 International License



DISSERTATION ABSTRACT

Aaron Zettler-Mann

Doctor of Philosophy

Department of Geography

June 2019

Title: Lateral Channel Confinement, Tributaries, and Their Impact on Channel Morphology

Humans have had a ubiquitous influence on fluvial systems worldwide (Wohl, 2013). Landscape modifications such as lateral channel confinement and flow modifications frequently result in changes to channel morphology including width, depth, channel slope, unit stream power, and particle size distributions (PSD). Morphologic changes can be directly measured, but may also be reflected in the patterns of water surface roughness. This research builds on downstream hydraulic geometry (Leopold and Maddock, 1953) and the sediment links concept (Rice, 1998) to examine anthropogenic and natural controls on channel form across spatial scales. It also develops a method for mapping water surfaces with the same resolution we measure channel form.

This research examines how anthropogenic and natural mechanisms control channel form along a 200-kilometer section of the Rogue River in Southern Oregon. I use a combination of remote sensing and field data to create a hyperscale data set containing width, slope and depth data. I use Structure-from-Motion to create particle size distributions for all exposed gravel bars in the study area. With these data I conducted a number of non-parametric statistical analysis to examine how natural and anthropogenic forces influence longitudinal trends in channel morphology.

I find that the Rogue River is a highly heterogenous river. At basin-wide scales it does not conform to our traditional views of downstream hydraulic geometry. At smaller spatial scales, the role of local geology triggers an alteration between the commonly observed trends in downstream hydraulic geometry and trends that do not match theory. At scales of 10s of kilometers anthropogenic controls on channel form trigger statistically significant modification of channel form as compared to natural channel reaches. Tributary and non-tributary sediment sources do not consistently result in a statically significant change to channel morphology. However, evidence of persistent delivery of sediment through alluvial and colluvial processes does appear to play an important role in channel morphology. This research supports the claim that intensive and extensive data collection of fluvial systems will further out understanding of how external and autogenic processes control channel morphology; allowing the combination and improvement of current theory which exist and distinct spatial scales.

CURRICULUM VITAE

NAME OF AUTHOR: Aaron Zettler-Mann

GRADUATE AND UNDERGRADUATE SCHOOLS ATTENDED:

University of Oregon, Eugene, Oregon
University of Denver, Denver, Colorado
University of Colorado, Boulder, Colorado
Cabrillo College, Aptos, California

DEGREES AWARDED:

Doctor of Philosophy, Geography, 2019, University of Oregon
Masters of Arts, Geography, 2015, University of Denver
Bachelor of Arts, Geography, 2010, University of Colorado
Associate of Arts, Geography, 2006, Cabrillo College

AREAS OF SPECIAL INTEREST:

Structure-from-Motion
Close-range remote sensing
Fluvial geomorphology
Remote sensing of rivers
Human-river-landscape interactions

PROFESSIONAL EXPERIENCE:

Postdoctoral Fellow, Department of Geography, University of Oregon, Eugene,
Oregon, 2019 – 2020
Field Technician, InterFluve River Restoration and Water Resources Engineering,
Hood River, 2018 - 2019
Doctoral Teach Fellow, Department of Geography, University of Oregon,
Eugene, 2015 – 2019
Graduate Teaching Assistant, Department of Geography, University of Denver,
Denver, 2013 – 2015

GRANTS, AWARDS, AND HONORS:

EAGER Grant. Next-generation Riverscape Mapping and Monitoring. National
Science Foundation, 2019.

Sandra Pritchard Mather Graduate Fellowship, University of Oregon Department
of Geography, 2018

Doctoral Dissertation Research Improvement Award, Lateral Channel
Confinement, Tributaries, and Their Impact on Channel Morphology,
National Science Foundation, 2017

ACKNOWLEDGMENTS

I would like to express my appreciation for everyone who has helped me through this process. Both of my parents for encouraging and supporting my curiosity about the way the world works for as long as I can remember, and teaching me *science* as a way of exploring the world. Mark Fonstad for being an excellent advisor who helped me turn my love of rivers into a dissertation. Patricia McDowell for the opportunity to spend so many summers working and learning on the Middle Fork of the John Day. Andrew Marcus and Josh Roering for the enthusiasm for my work and the fun, interesting and intellectually challenging conversations throughout the process.

The Bureau of Land Management (BLM) for their support with research special-use permits for sections of the Rogue River. The National Science Foundation for the funding they provided through a Doctoral Dissertation Research Improvement grant. I would also like to thank a number of field assistants who helped collect data, navigate rivers and did much of the data processing: James Major, Clay Schmitt, Priscilla Macy, Josh Spector, and Laura Gravelle. James Dietrich for help with the programming and the hyperscale graph code, originally from Patrice Carbonneau.

Everyone who I have spent time on a river with. The roots of this dissertation begin with watching sand bars change on the Middle Fork of the American River over many years as a raft guide for All Outdoors. They extend through conversations with Clinton Begley and others over the last five years while driving and kayaking across the Pacific Northwest.

The River Rats group for the support and sense of comradery as we all try to navigate graduate school. And to my sister and the rest of my family for their enthusiasm and curiosity, regardless of whether they understand anything I'm talking about.

To my wife, Laura.

Thank you for your love and support on this journey. And making sure I always saved
time to play on rivers.

TABLE OF CONTENTS

Chapter	Page
I. INTRODUCTION	1
II. THE IMPACT OF ANTHROPOGENIC LATERAL CHANNEL CONFINEMENTS ON CHANNEL FORM	7
Introduction.....	7
Study Area	11
Methods.....	12
GIS Processing.....	13
Field Data.....	18
Analysis.....	21
Results.....	21
Channel Morphology and Confinement.....	21
Gravel Bars	24
Discussion.....	25
Geomorphic Variables	27
Gravel Bar Analysis.....	29
Conclusion	30
Bridge.....	41

Chapter	Page
III. A RIVERSCAPE MAPPING APPROACH TO THE SEDIMENT LINKS	
CONCEPT	42
Introduction.....	42
Study Area	47
Methods.....	49
Methodologic Approach	50
GIS Processing.....	50
Field Data.....	53
Analysis.....	56
Results.....	57
Hyperscale Analysis.....	61
Discussion.....	64
Digital Photoseiving Calibration.....	66
Spatial Patterns of Gravel Bars	67
Sediment Links	68
Relative Depth	71
Historic Anthropogenic Context.....	72
Additional Geomorphic Controls.....	74
Hyperscale Graphs	76
Conclusion	77
Bridge.....	90

Chapter	Page
IV. VIDEO STRUCTURE-FROM-MOTION: DEVELOPING A METHOD FOR CONTINUOUS MAPPING OF WATER SURFACES.....	92
Introduction.....	92
Research Design.....	95
Methods Development Strategy.....	95
Camera Synchronization.....	96
Static Surface and Scale Tests	97
Dynamic Surface Tests	99
Point Cloud Post-Processing.....	101
Results.....	102
Camera Timing	103
Flat and Horizontal Surface Results	103
Dynamic surface Results.....	104
Discussion.....	105
Image composition.....	106
Point Cloud Post-processing.....	107
Scale	108
Surface Tests.....	109
Future Work	110
Conclusion	111
V. SUMMARY	122
REFERENCES CITED.....	124

LIST OF FIGURES

Figure	Page
 CHAPTER II	
1. The Rogue River sits in the Southwest corner of Oregon. The study area encompasses the two orange areas. The study area consisted of roughly 200 kilometers of river encompassing wide unconfined alluvial valleys with low anthropogenic activity, anthropogenically confined alluvial valleys and naturally confined reaches.	33
2. An example of an incised channel in the Rogue River. This photo taken at approximately river kilometer 50. Smoke from nearby forest fires is clearly visible.	34
3. Scatter plot of D_{50} and D_{84} gravel size thresholds as computed in BASEGRAIN by research assistant LG (square) and JS (circle). The empty symbols show D_{50} and filled shapes are D_{84} . The highest concentration of duplicated bars is in the middle of the figure, roughly between 108000 to 140000 meters downstream. A single-factor ANOVA analysis of the gravel bars generates a p-value of 0.68, suggesting that the results are similar.	34
4. Gravel size metrics for all of the gravel bars the USGS hand sampled gravels in 2011 which we duplicated sampling as part of this study. Each size threshold is denoted by the same symbol. The USGS samples are green and our values are in black. An ANOVA test revealed that the two data sets are not statistically different with a p-value of 0.65.	35
5. Plots of each of the hydro-geomorphic variables measured and computed for the study area. The vertical dashed line is the location of the split between the alluvial, high development reach and the low development reach. The gap in the relative depth model (sub plot 5) is due to a sensor error resulting in no depth data. Blue X indicates locations where both banks have an anthropogenic confinement and the red triangles are locations where only one bank is anthropogenically confined. Water flow is from right to left and distances are in kilometers. Flow is right to left and distance is in kilometers.	36
6. Aerial imagery of Grants Pass from 1939, and current NAIP imagery of the same area. Notice that gravel bars have decreased in area (A, B) during the same time period that Grants Pass has expanded. At B the unvegetated, mid-channel gravel bar has connected to the left bank and is becoming vegetated.	37

Figure	Page
CHAPTER III	
1. Rogue River watershed location in Oregon (upper left) and a detailed map of the study area. Gravel bar sample locations, tributaries and Grants Pass are also labeled.	81
2. General geologic units of the Rogue River study area and the locations of measured gravel bars, tributaries and non-tributary sediment sources	82
3. Comparison images of a portion of gravel bar ‘MidValley_14’. On the left is the partitioned image from BaseGrain. Blue lines show the location of the a and b axes used in the computation. The right image shows the original photograph of the same area. The black bar (upper right) is one meter in length.....	83
4. An example of the sampling method for the statistical analysis looking at the confluence of Galice Creek and the Rogue River. The black rectangle shows the extent of an 80-meter sample, here sampling channel widths. The selection of width values here will be compared to all width values	83
5. The hydrogeomorphic variables discharge, slope, width, unit stream power, depth, D_{84} and D_{50} for the Rogue River. Flow direction is from right to left. The red dashed lines show the downstream hydraulic geometry best-fit equations. Width, depth and each gravel size are computed using a power function. Slope is computed as an exponential function. Unit stream power is computed using the downstream hydraulic geometry equation prediction from the other variables. Vertical lines show the location of potential sediment links. Solid lines are tributary locations and dashed lines show non-tributary sediment sources.	84
6. Historical imagery from 1939 (left) and current NAIP imagery (right) showing the shift in the confluence of the Applegate River (entering from the south) and the Rogue River (flowing right to left). The riffle associated with the confluence of the two rivers is outlined in black.....	85
7. Hyperscale correlation coefficients for width and distance downstream. Gaps in the data occur where the correlation is not statistically significant ($p=0.01$).	86
8. A close-up view of the 10 km and below window size examining the correlation between width and discharge. The study area begins in the upper right, and flows right to left through each row. The black diagonal lines show the location of named riffles and rapids.....	87
9. Hyperscale correlation coefficients for width and distance downstream. Gaps in the data occur where the correlation is not statistically significant ($p=0.01$).	88

Figure	Page
10. A close-up view of the 10 km and below window size examining the correlation between slope and discharge. The study area begins in the upper right, and flows right to left through each row. The black diagonal lines show the location of named riffles and rapids	89

CHAPTER IV

1. This shows the process we used to develop a workflow for ViSfM.....	113
2. The frequency distribution of differences in sync frames between each of the five GoPro cameras used. Frame differences were computed as the difference in sync frame between any two cameras (eg: C1-C2; C1-C3, C2-C3 etc). In this figure n = 90	114
3. Measured vs modeled distances between ground control targets. The location of each target within the area can be seen below the table	115
4. Photo of the raft with the W shaped camera array. The top bar is the base for three cameras, and the two vertical poles are the base for the two remaining cameras. The fiberglass poles extending behind the boat hold a meter-long scale bar used to test the scale of resulting water surface DEMs	116
5. This figure looks at the doming within the point cloud before and after the 2.5D doming correction. The top row (A & B) are for the static surface. The lower row (C & D) are for the flat water surface.....	117
6. Figures A, B and C are video from used to create water surface models. Images are arranged to match the camera orientation. (A) shows a section of flat water in full sun. (B) shows a partially shaded section with a mean wave height of approximately 0.20 meters. (C) shows a full sun section with wave heights of approximately 0.50 meters. In C, note the back side of the wave has no reconstruction as this wave face was not visible given the camera height and orientation	118
7. This figure shows the signed distance between the reference mesh and +/- 2 frame point clouds as part of the dynamic surface test from the bank onto the Willamette River. The frequency distribution of the errors is displayed vertically along the color ramp of error values	119
8. The workflow we recommend using when applying ViSfM in future applications	120

LIST OF TABLES

Table	Page
 CHAPTER II	
1. Reach and sub-reach scale summary statistics for each of the hydrogeomorphic variables.	38
2. The p-value for each hydro-geomorphic variable is displayed. The location of the confining feature is denoted in the first column as kilometers downstream. There are seventeen single-bank confinements and thirteen locations with a both-bank confinement. There are no single-bank anthropogenic confining features in the mixed geology, low-use sub reach. Reported values are the p-value indicating statistical significance of a given confinement within the reach it is located. The break between the alluvial, high-use sub reach and the mixed geology, low-use sub-reach is at river kilometer 104.....	39
 CHAPTER III	
1. Gravel bar name, location and respective size thresholds. The D ₅₀ sizes are generally course gravels while D ₈₄ falls into the cobble classification. Within a given size class most observations do not deviate from the reach average, with most observations falling close to the reach average as indicated by normalized size values close to one.	79
2. Statistical output table for all of the tributaries and landslides for all hydrogeomorphic variables. We take a p-value < 0.05 to indicate a statistically significant result.....	80
 CHAPTER IV	
1. 2.5D best fit equations before (Pre) and after (Post) transformation for the static and dynamic horizontal surfaces. Here, we take the coefficients as a metric for the severity of curvature in the surface where the larger coefficients (pre-transformation) indicate more doming of the surface.....	121

CHAPTER I: INTRODUCTION

Human activity has had some impact on nearly every watershed in the United States. The range of impacts include dam construction preventing upstream – downstream connectivity, flow modification, and channelization resulting in changes to transport capacity and flow regimes. Common to all of these is the modification of sediment flux within the fluvial system and therefore a disruption of predicted downstream hydraulic and geomorphic trends (Grant G.E., O’Connor, & Safran, 2016; Montgomery & Buffington, 1998). A number of theories have sought to provide a conceptual framework for longitudinal trends in channel morphology. Some examples of these are the river continuum concept (Vannote, Minshall, Cummins, Sedell, & Gushing, 1980), channel-reach morphology (Montgomery & Buffington, 1997), downstream hydraulic geometry (Leopold & Maddock, 1953), and the sediment links concept (Rice, 1998). At basin extents, downstream hydraulic geometry describes the fundamental longitudinal trends in channel morphology. Driven by channel adjustment to increasing discharge with increasing watershed area, downstream hydraulic geometry predicts a general increase in channel width and depth, and a decrease in slope and fining of channel material as one travels downstream. The trends predicted by downstream hydraulic geometry are at the heart of popular channel classification schemes (Rosgen, 1994), landscape evolution models, and theories for longitudinal trends in channel form like those mentioned above. Similarly, channel-reach morphology and the river continuum concept seek a mechanism of channel characterization, relying on the links between channel morphology and channel-forming processes. The sediment links concept is similar, but rather than trying to define reaches *a priori* relying on generally observed

trends, unique reaches are defined based on observations of the form-process relationship. This still requires generalizations, emphasizing some longitudinal trends while minimizing others.

What is more frequently observed from measurements of channel width, depth, slope and particle size distribution is a far noisier signal where local processes such as tributaries, hillslope processes, geologic controls and anthropogenic activity control channel form. While useful for contextualizing general observations of channel form, broad-scale approaches to the classification of fluvial systems rarely match the highly complex and heterogeneous trends observed through detailed studies of a river (Fonstad & Marcus, 2010). With current methods for collecting extensive, high-resolution data sets of fluvial systems we are becoming increasingly aware of the complexity in coupling channel form, process and control. The goal of this research is to improve our understanding of downstream patterns of channel width, depth, slope, unit stream power and gravel sizes in the context of natural and anthropogenic controlling forces. In addition, this dissertation works to develop a method for mapping water surface roughness at a process scale; the same scale I map morphologic variables.

One ubiquitous and largely unstudied anthropogenic impact on fluvial systems is lateral channel constrictions (Blanton & Marcus, 2009, 2013; Fryirs, Wheaton, & Brierley, 2016; Garcia Lugo, Bertoldi, Henshaw, & Gurnell, 2015; Pechenick et al., 2014). Generally speaking, lateral channel constrictions are any feature that prevents lateral channel movement, limiting bank erosion, valley bottom deposition and floodplain access. Examples include roads, railroads and bridges. The presence of these features proximal to a river can prevent lateral channel movement and increase depth and velocity

by confining the channel and preventing floodplain access. Blanton and Marcus (2009) published one of the first papers examining the extent that lateral channel constrictions exist in the US. Their GIS analysis show that lateral channel constrictions exist in every part of the US and that mountainous regions such as the North East and Pacific Northwest see a higher portion of river reaches being impacted by lateral channel constrictions due to the co-location of transportation networks in alluvial valleys. Confining the channel results in an increase in depth at a given flow, increasing the hydraulic radius and therefore, shear stress increase which can drive an increase in mean particle size, and positive skew in the particle size distribution (Leopold, Wolman, & Miller, 1992). A similar process to that downstream of dams (Garcia Lugo et al., 2015; Lane, 1955; Pechenick et al., 2014). The indirect impact of changing sediment supply and hydraulic conditions may also include changes in channel width, depth and slope (L. A. James & Marcus, 2006; Pechenick et al., 2014; Petts, 1985). Human modification of hydraulic regimes and channel morphology trigger sediment breaks, likely producing an identifiable signal in the particle size distribution, width, depth, slope and as a result, unit stream power. Identifying the presence and spatial extent of morphologic change requires high resolution data that can be used to distinguish different forms of morphologic change across multiple scales. In Chapter II, this research seeks to explore the relationship between lateral channel constrictions, channel morphology, and particle size.

Channel form and the related channel-forming processes are a function of anthropogenic and natural controls on a fluvial system. One way of conceptualizing the natural controls on channel form is through the sediment links concept (Rice, 1998) which suggests that the general trend of downstream fining of sediment is actually broken

up into individual sections, or links. The work of Rice focused on tributaries as a predominant source of new material, but recognized the importance of other sources like hillslope processes and fans.

The studies by Rice and others focused on tributaries as sources of sediment. However, we know that there are other sources of sediment in fluvial systems in addition to tributaries. For example, bank failure, landslides and debris flows (Grant G.E. & Wolff, 1991; Jacobson, Cron, & McGeehin, 1989; Lisle, 1987). These sources of sediment will also result in a shift in the particle size distribution, local increase in slope and change in channel width. Despite being potentially significant sources of sediment at a single event, the examples mentioned above frequently have longer return intervals. As time passes, mechanical breakdown of material and less frequent, larger flood events may remove some or all of the sediment link signal. Chapter III of this dissertation looks at the role that tributaries, landslides, bank erosion and the legacy of anthropogenic land use have on channel form in the context of sediment links and downstream hydraulic geometry.

The relationship between channel morphology and water surface patterns has been used to define unique habitat units (Harvey & Clifford, 2009; Harvey, Clifford, & Gurnell, 2008; Marcus, 2002; Zavadil, Stewardson, Turner, & Ladson, 2012). Surface flow structures are related to channel morphology, and by identifying different flow structures it is possible to know something of channel morphology and therefore physical habitat. SfM based water surface mapping has had some success in distinguishing broad physical habitat units. However, most applications have looked at differentiating between general hydraulic features such as riffles, runs, pools and glides (Harvey & Clifford,

2009; Marcus, 2002; Amy S. Woodget, Austrums, Maddock, & Habit, 2017). Previous academic work has not been able to address channel morphology within riffles and rapids beyond simple classification. This approach also fails to measure patterns of water surface roughness at the spatial scale of the hydraulic processes responsible for waves, riffles, and holes. This presents a fundamental mismatch in data resolution, channel form can be measured across scales from the basin to the grain, while water surfaces can only be mapped at the scale of the hydraulic unit and larger.

Chapter IV develops a method for creating quantifiable maps of water surfaces in riffles and rapids. The premise for this method relies on Structure-from-Motion (SfM) which is widely implemented in geomorphic and habitat mapping applications (Carbonneau & Dietrich, 2017; Fonstad, Dietrich, Courville, Jensen, & Carbonneau, 2013; Hugenholtz et al., 2013; Tamminga, Hugenholtz, Eaton, & Lapointe, 2015). Rather than a single camera moving through space multiple cameras fixed in space, relative to each other, all capture the same scene simultaneously. Previous studies have successfully mapped water surfaces in highly controlled field and lab settings (J. Chandler, Wackrow, & Sun, 2008; Dietrich & Fonstad, 2012; Han & Endreny, 2014). While these studies have proved successful in producing accurate maps of water surfaces, the extensive camera-system set up and challenges with precise and consistent image acquisition means they are not practical for studying larger areas or broad application. The method developed in Chapter IV proposes a workflow for creating continuous maps of water surface roughness using an easily scalable workflow and off-the-shelf equipment.

Improving our conceptual models of fluvial systems requires analyzing and interpreting them at different scales than previously done. If we hope to offer meaningful

interpretations of the heterogeneity of fluvial systems at watershed scales we must move beyond isolated samples of hydrogeomorphic variables with interpolated lines between them. This dissertation takes advantage of recent advances in small UAVs, Multi-View Stereo Structure-From-Motion, high-resolution remote sensing, and LiDAR data to create a near-continuous hyperscale picture of the Rogue River, Oregon. With hyperscale data, I am able to explain the relationship between channel form and process; both naturally occurring and anthropogenically forced. In addition, the hyperscale analysis in this dissertation offers insight into the role that autogenic processes have on channel form such as pool-riffle sequences and the dispersion of sediment waves across spatial scales.

CHAPTER II
THE IMPACT OF ANTHROPOGENIC LATERAL
CHANNEL CONFINEMENTS ON CHANNEL FORM

Introduction

Human activity has had a ubiquitous impact on the geomorphic variables often used to quantify channel form, including channel width, slope, depth, sinuosity, gravel sizes, roughness and stream power. Dams are a frequent point of discussion when considering anthropogenic impacts on fluvial geomorphology as they significantly alter downstream sediment transport, which often results in channel incision and an increase in mean particle sizes downstream of the dam (Brandt, 2000; Petts, 1985; Petts & Gurnell, 2005). Equally pervasive in the United States, lateral channel confinement increases shear stress, which can also lead to an increase in particle size, similar to that downstream of dams (Garcia Lugo et al., 2015; Pechenick et al., 2014). The indirect impact of changing sediment supply and hydraulic conditions at confining margins may also alter channel width, depth, slope and velocity (L. A. James & Marcus, 2006; Pechenick et al., 2014; Petts, 1985). This study seeks to augment our knowledge of the effects of human activity on channel form, focusing specifically on lateral channel confinement.

Channel confinement requires a clear definition. We build on the definition of Fryirs et al. (2016) who define confinement as a channel which abuts a confining margin on either bank. Here, we specify that the confining margin must interact with the channel at the bankfull flow. We also differentiate between naturally confining margins (e.g. bedrock outcrops and hillslopes) and anthropogenic confining margins (e.g. levees, roads

and bridge abutments). Given the ubiquitous nature of lateral channel constrictions of both types in the landscape, it is important to understand how lateral channel constrictions impact channel morphology and particle size distributions. A survey by Surian and Rinaldi (2003) of morphologic response to river engineering covered the impacts of a variety of forms of river engineering activities including dams, gravel mining and channelization. The morphologic impacts associated with channelization, including those resulting from transportation infrastructure, included a range of impacts which can include channel incision, decrease in channel width and/or a transition from braiding patterns to wandering (Surian & Rinaldi, 2003). While particle size distribution is not directly discussed in this paper, the processes that led to many of the observed channel-form morphologic changes would likely result in an increase in mean particle size and positive skew in the particle size distribution. The increased shear stress, from channelization and increased depth at a given discharge, should result in the transport of larger material at any given flow event resulting in an overall increase in remaining in-channel gravel sizes (Lane, 1955; Leopold et al., 1992).

In their 2009 study, Blanton and Marcus use national level stream and road data to characterize the nature and extent of lateral channel constrictions. Their findings indicate that anthropogenic channel modifications are ubiquitous features throughout the landscape. The relationship between the type of channel constriction and landscape setting falls along a continuum. More open areas such as plains regions and wide alluvial valleys tend to result in more crossing-related channel constrictions (e.g. bridges and culverts), compared to lateral constrictions. As valleys become narrower, lateral channel constrictions dominate over crossing constrictions.

More recent work examined how lateral channel constrictions and road networks influence the quality of habitat in fluvial systems, of which particle size distribution and channel morphology are a major component (Blanton & Marcus, 2013; Fryirs et al., 2016; Pechenick et al., 2014). The study by Blanton and Marcus (2013) uses paired confined and unconfined reaches in the Yakima and Chehalis Rivers in Washington State to test the impact of channel confinement. Their findings indicate that channel confinement results in narrower channels, a decrease in large wood, a loss of side channels and decrease in mean riparian width. Pechenick et al. (2014) use a multi-variate, multi-scale statistical approach to describe the impact of roads on channel health as defined by field assessments developed by the Vermont Agency of Natural Resources (VANR). Their regression analysis suggests that, among other factors, channel confinement is an important predictor of a decrease in channel health, as assessed by the VANR.

The use of GIS-based analysis in previous studies (Blanton & Marcus, 2009, 2013; Fryirs et al., 2016; Pechenick et al., 2014) provides reach-scale insight into the impact of lateral channel confinement. These papers show that channel confinement decreases channel and floodplain complexity which the authors use as a proxy for habitat health. However, these papers don't address quantitative metrics of habitat quality, such as particle sizes, or explore if single bank confinements differ from dual-bank confinements in how they impact channel form. An improved understanding of the direct impact that channel confinements have on channel form (width, depth, slope, gravel sizes) therefore requires an approach which looks at the magnitude and nature of changes in channel form varies across spatial scales as a result of lateral confinements.

The research in this study combines GIS and remote sensing data to estimate channel width, slope and compute unit stream power and explore how confining margins impact the hydrogeomorphology of channels at the confining margin. High resolution field data on depth and gravel sizes at all exposed gravel bars enhances the GIS dataset, allowing direct comparisons between trends in confined and unconfined sub-sections and sediment sizes. Through this study we aim to improve our understanding of how natural and anthropogenic confinement alters a suite of channel morphology variables at scales from local gravel deposits to kilometers.

Specifically, we use non-parametric statistical analysis, field observations and the historical context of the Rogue River use to answer the question: How do hydrogeomorphic variables change as a result of single and dual-bank channel confinements?

- H₁: Confined reach width values will be smaller than unconfined reach width values
- H₂: Confined reach slope values will be larger than unconfined reach slope values
- H₃: Confined reach unit stream power values will be larger than unconfined reach unit stream power values
- H₄: Confined reach gravel sizes will be larger than the same size class in unconfined reaches
- H₅: Confined reach relative depths will be greater than those in unconfined reaches

Transportation infrastructure is ubiquitous across alluvial valleys, confining channels and preventing floodplain access thus decreasing habitat complexity (Blanton & Marcus,

2009, 2013). The coupling of hydraulics and channel form mean that confining a channel will likely have an impact on channel form (Knighton, 1998; Leopold et al., 1992). In testing the above hypotheses, we hope to better constrain the degree to which lateral anthropogenic controls on a channel result in morphologic changes. A better understanding of how channel confinement exerts a primary control on channel form, and across what spatial scales those impacts are felt is important when considering certain active restoration activities like adding high-flow water passage under lateral confinements. Results from this analysis have the potential to improve how restoration activity is approached in riparian corridors.

Study Area

Testing our hypotheses requires a study area which has alternating stretches of anthropogenic confinement, natural confinement and unconfined reaches. Alternating channel margin types provide the potential to account for longitudinal trends in channel morphology which could otherwise confound our analysis. Oregon's Rogue River flows through alluvial valleys, naturally confined and anthropogenically confined areas (Figure 1). The alternating channel margin and valley bottom conditions allow us to separate longitudinal trends like downstream hydraulic geometry from the impact of confining margins. This study begins downstream of the confluence of the Little Butte Creek and the Rogue River, in a wide valley of Quaternary alluvial deposits dominated by agriculture. Just before the first confining section the Rogue River flows through lacustrine deposits, located just upstream of the old Gold Ray Dam site (removed 2010). The first confined section is naturally confined (approximately RKM 50). The river continues into a widening alluvial valley, with alternating areas of hillslope and

anthropogenic confinement before passing through the city of Grants Pass where it is heavily laterally confined. After Grants Pass the valley remains wide as anthropogenic confinements end and agricultural land-use dominates. As the river enters the Klamath Terrain (RKM 125) , the channel margin narrows, first with occasional natural confinement, then full and near continuous natural confinement. Beginning at approximately RKM 175 the valley widens again before the study area ends upstream of the confluence of the Illinois River. In all, the study area comprises 200 kilometers of the Rogue River. For analytical purposes we consider the study area as a single large area and as two sub sections; an upper alluvial section and a lower, geologically confined section. The break is downstream of the confluence of the Applegate River (Figure 1).

In the upper portion of the study area the Rogue River is generally a meandering river with grade control derived from bedrock and cemented gravels (Jones, O'Connor, Keith, Mangano, & Wallick, 2011). Below Grants Pass, the Rogue River is semi-controlled (Schumm, 1985) with alternating gravel point bars and some straight reaches (Knighton, 1998). In some sections, cemented gravels and bedrock provide vertical and lateral control on the river (Jones et al., 2011). The longitudinal alterations between natural and anthropogenic lateral controls in the Rogue River allows us to control for the potential signal of watershed scale variations in channel form.

Methods

Spatial complexity in channel form is a frequently used metric to gage habitat diversity of a riparian system. Measuring channel forms and processes across scales is important for understanding their relationship. This requires tools which allow us to measure channel form across scales. To assess the impact that lateral channel

constrictions have on channel form we measure width, slope, depth and compute unit stream power continuously. Using high spatial resolution GIS data along with field observations allows us to assess the impact of confining margins on channel morphology across spatial scales. This study integrates the National Elevation Dataset (NED) 10-meter elevation data, 1.2 meter LiDAR data, aerial imagery from the National Agriculture Imagery Program (NAIP), soil maps from the U.S. Department of Agriculture (USDA), geologic maps from the Oregon Department of Geology and Mineral industries (DOGAMI) and the 100-year flood inundation maps from the Federal Emergency Management Agency (FEMA) (Archuleta, Constance, Arundel, et al., 2017). I collected aerial imagery using a DJI Phantom 3 UAV and a Nikon D5200 digital SLR camera. Depth data was collected using a Seafloor Systems Hydrolite-TM single beam echo sounder paired with a Trimble GeoX7 handheld data collector. These data were combined to create a spatially intensive and extensive data set for the multi-scale analysis of how natural and anthropogenic confinements control channel morphology and gravel sizes.

GIS Processing

Using the above GIS data layers, we digitized the bankfull channel margin, valley margin and anthropogenic confining margins following methods outlined by Fryirs et al. (2016) and Pechenick et al. (2014). Delineation of the bankfull channel margin required use of the NAIP imagery, 1.2-meter LiDAR data, 10-meter NED elevation data and FEMA floodplain maps. The active channel was defined as the bankfull width, which was identified from NAIP imagery and breaks in the bank slope from LiDAR. On the NAIP imagery we identified active portions of the channel based on the presence of

active, unvegetated gravels and the type and presence of vegetation along the channel margin. Soils which were characterized as river wash were also included within the active channel (Harrelson, Rawlins, & Potyondy, 1994). We used the latest FEMA floodplain maps as a check on active channel margin. At no point does the bankfull channel margin cross the 100-year floodplain, but in certain confined sections they follow the same path. Digitizing the anthropogenic margin followed a similar process with an emphasis placed on imagery, field observations and LiDAR. Anthropogenic confining margins were characterized as any location where a confining margin fell within the bankfull channel width. This was noted by places where the channel width decreased upon contact with the confining feature or where the Rogue River actively flows along the confining margin. Natural confining margins were any categorized as any location where bedrock intersected the active channel. Digitizing was confirmed with field observations. We included anthropogenic confining features such as road, railroads and bridge abutments. A channel margin was considered anthropogenically confining if it was located inside the estimated bankfull channel width. This was defined as any place where channel width decreased after entering a reach with lateral anthropogenic controls. Locations where channel incision was informally observed (Figure 2) were not included as anthropogenic confinement unless there was anthropogenic reinforcement of the incised bank. In the field we interpreted places where the geomorphic floodplain was perched above the active channel and separated by vertical banks as evidence of channel incision.

Distance downstream and channel width were derived from the digitized bankfull channel margin shapefile using the MATLAB program ChanGeom V0.3 (Fisher, Amos, Bookhagen, Burbank, & Godard, 2012; Fisher, Bookhagen, & Amos, 2013). From the

bankfull shapefile we created a four-meter pixel raster image, a balance between the necessary high resolution imagery and processing times. ChanGeom determines the centerline of the raster image, computing a cumulative distance downstream along the center line, and computes channel width perpendicular to the center line. The output of the ChanGeom program is a channel centerline and width measurement every four meters. Computing elevation requires a moving window of distance downstream over which to compute elevation change. It is important that this window be large enough to capture elevation change in low-slope reaches without being so large as to smooth over small riffles and rapids. We built a semi-variogram to determine at what distance adjacent elevation values were no longer related, termed the range of a semi-variogram. For the Rogue River, this distance was roughly 40 meters. We extracted elevation along the channel centerline, the water surface elevation, at each point from the NED data and used a moving window of 40 meters to compute slope.

There are five gages on the Rogue River, two of which are within the study area, two upstream of the study area, and one just downstream of the study area. We used the log-Pearson Type-III method to estimate the two-year return interval flood for all five gages; we considered this the channel forming flow, that is, the flow at which channel width, depth and gravel sizes are adjusted to (Knighton, 1998; Wolman & Miller, 1960). We used a second-degree polynomial regression equation using drainage area at each of the five gages to develop a discharge-area model ($R^2=0.99$). We then applied this model to ungaged sites throughout the basin by computing flow accumulation area from the ten-meter NED data generating a computed discharge at every pixel along the channel. From the above variables we computed unit stream power (Equation 1) to provide a

physically based measure of sediment transport competence (Bagnold, 1966; Phillips, 1989).

In addition to confinement there are sections of the Rogue River channel which appear to be incised. We consider incision as a section of channel such that at the channel forming flow (Q_2) the water surface sits below the geomorphic bankfull (Harrelson et al., 1994). To test whether the channel did appear to be incised we used an inverted form of the Manning's Equation to estimate water depth at the Q_2 discharge at the gravel bars located in areas with potentially confined reaches. Because we needed D_{84} to compute an estimate of channel roughness (Manning's n) we could not compute water depth continuously for the study area. We computed water depth at the bankfull discharge using an iterative process. Manning's n was computed based on the D_{84} at gravel bars using the approach of Hey (Hey, 1979) (Equation 2) and the D_{84} at a gravel bar. The estimated roughness value was then used to compute channel velocity using the Manning equation (Equation 3), given the estimated bankfull discharge at that location. Hydraulic radius (Equation 4), wetted perimeter (Equation 5) and cross section area (Equation 6) were all computed from width using a triangular estimate of cross section shape, which was found to be the most accurate based on multiple experimental cross sections in the study area. To estimate water depth at the Q_2 discharge, I used a goal-seeking approach where depth increased iteratively until the computed discharge (Equation 7) matched the estimated Q_2 discharge at a given location.

$$\omega = \frac{\rho g Q S}{W} \quad [1]$$

$$n = \frac{0.1129 R^{0.167}}{2.03 \left(\log \left(\frac{R}{3.5 D_{84}} \right) \right)} \quad [2]$$

$$v = \frac{R^{0.667} S^{0.5}}{n} \quad [3]$$

$$R = \frac{w}{((2*D)+w)} \quad [4]$$

$$P = 2 * \sqrt{(W/2 + D^2)} \quad [5]$$

$$A = \frac{(W*D)}{2} \quad [6]$$

$$Q = W * A * V \quad [7]$$

In the above equations ω (W/m²) represents unit stream power, ρ (kg/m³) is the density of water, g (m/s²) is the gravitational constant, Q (m³/s) is discharge, S (m/m) is slope and W (m) is channel width, R (m) is hydraulic radius, n is the Manning Roughness coefficient and P (m) is the wetted perimeter. For locations where field observations suggested an incised channel, we computed an estimated water depth using equations 1 through 7. We computed depths at the Q_2 depth as between 3.7 meters and 9.5 meters. Where we were able to compute an estimated Q_2 depth, the summer low-flow thalweg depth was frequently between four and five meters deep. The computed Q_2 discharge is more than double the low-flow discharge suggest that a depth increase of four to five meters is reasonable. The computed depth at the Q_2 discharge within the channel was used to check whether the channel was incised below the geomorphic floodplain. Where the Q_2 water depth was less than the vertical distance between channel bottom at the thalweg and the geomorphic floodplain the channel is likely incised. The result of the GIS data processing is a spatial dataset with a point every four meters containing the northing and easting, distance downstream, elevation, channel width, channel slope, discharge and unit stream power.

Field Data

Field work was used to collect the data necessary for computation of the particle size distribution for all exposed gravel bars and channel depth data. To better understand the ways in which channel confinements impact gravel size distributions and depth through space, high resolution depth and gravel size data were needed. We wanted to have data at a resolution that showed variation within a single confining feature, between adjacent confining margins, and at basin-wide extents. Field work took place over nine days spread over three trips traveling 200 kilometers of the Rogue River in a fifteen-foot cataraft. Field work took place during dam-controlled summer low-flows of 32.5 cms (95% exceedance) to maximize the number and size of exposed gravel bars. Every attempt was made to travel in the channel thalweg so that depth data from the echo sounder represented the deepest point in the channel. However, this was not always possible due to rapids and other obstacles. The echo sounder and GeoX7 recorded a point every five seconds comprised of channel depth, northing, easting and elevation. Initial study design planned to use the field collected GIS elevation data as a water surface slope map but poor precision in the Z direction, with values changing up to 100 meters between adjacent measurements, meant that this was not possible. Because the LiDAR elevations were collected during higher discharge than when depth data was collected we did not feel it was appropriate to correlate the measured depths with LiDAR or NED elevations which approximate the water surface. Depth measurements therefore represent a relative depth model (RDM), showing channel depth detrended from any elevation data. Downstream trends in depth associated with pool-riffle sequences are visible as

longitudinal changes in depth but it is not possible to use this data to estimate longitudinal trends such as water surface or energy slopes.

Airspace and land management allow for the flight of UAVs from the beginning of the study area near White City to the confluence of Grave Creek. For all exposed gravel bars in this section I collected the aerial imagery using a DJI Phantom 3 UAV. From Grave Creek to the end of the study area at Illahe the Rogue River flows through a designated Wild and Scenic River corridor which prohibits UAV operation. For gravel bars within this section I walked gravel bars taking photographs with a Nikon D5200 on telescoping pole.

All gravel bars were photographed from heights between four and ten meters above ground level giving a horizontal and vertical ground resolution of 0.4 cm or better. Camera height for a given gravel bar was chosen based on visual estimations of the gravel sizes present, ensuring that individual clasts were clearly visible. Each gravel bar was processed using Agisoft PhotoScan 1.4 (now Metashape) generating a sparse point cloud, dense point cloud and georeferenced orthophotograph for each gravel bar (Fonstad et al., 2013; M. R. James & Robson, 2014; Westoby, Brasington, Glasser, Hambrey, & Reynolds, 2012). All gravel bars were exported as GeoTIFFs with one-centimeter resolution to standardize analytical scale between gravel bars. For the UAV based imagery we used a direct georeferencing approach relying on the UAV's internal GPS. This led to small ranges of uncertainty in absolute gravel bar location which were deemed acceptable in exchange for more efficient data collection in the field by not having to survey ground control points at each bar (Carbonneau & Dietrich, 2017). The gravel bars photographed using camera-on-a-pole required ground control points so that they could

be georeferenced, which we did with the Trimble GeoX7. It took between 30 and 200 photographs to capture gravel bars depending on the size of the bar and camera height.

We analyzed gravel bar orthophotographs using the BASEGRAIN 2.2 which is implemented in MATLAB (Detert and Weitbrecht, 2012; 2013). BASEGRAIN is a progressive edge detection algorithm which iteratively turns clasts to white and the shadowed interstitial spaces black, and converts the white raster areas to individual vector polygons. It then computes the A axis, B axis, area and orientation for each identified gravel, exporting these data as a .csv file. Small gravel bars ($<15\text{m}^2$) were processed as a single image. Large gravel bars ($>15\text{m}^2$) were broken into a series of 15m by 15m tiles. This was done to increase processing efficiency of BASEGRAIN. After processing, the .csv tables were combined so that each gravel bar had a single table with all gravel data. From the data tables containing the size of all gravels, we computed the D_{16} , D_{50} and D_{84} . Photoseiving is an increasingly popular approach to quantifying particle sizes over large areas (Detert, Kadinski, & Weitbrecht, 2018).

The recommendations of Detert and Weitbrecht (2012, 2013) were followed concerning the parameterization of BASEGRAIN. Before processing each image, vegetation and fines were masked in BASEGRAIN. After processing the user can choose to examine the partitioned image and mask, then merge or split clasts based on their visual analysis of the image. Two research assistants each processed the gravel bars and conducted some repeat measurements of the same gravel bars to evaluate if there were significant variations between personnel (Figure 3). The gravel bar metrics were also compared to hand sampling of gravel bars conducted by the USGS in 2011 (Jones et al., 2011) on duplicated gravel bars (Figure 4).

Analysis

As a check of the accuracy of BASEGRAIN we compared the D_{16} , D_{50} and D_{84} values we computed against the hand-sampled USGS results from 2011 using single factor ANOVA. Gravel bar spatiality was analyzed using Getis-Ord General G to determine whether gravel bars were randomly distributed within the study area as the hypothesized high transport capacity and decreased width may lead to fewer gravel bars per distance in confined reaches. To explore locations within the study area that do exhibit some clustering we used the Getis-Ord G_i^* .

Study area analysis to compute percent confinement followed the methods outlined by Fryirs et al. (2016) which used distance of a confining margin and the section stream length to compute confined percent. To describe the statistical difference of confined sections to unconfined sections we extracted all measured and computed hydrogeomorphic variables (width, slope, discharge, ω , and relative depth) at each confining feature, separating single bank confinement and dual-bank confining margins. We used the non-parametric 1-tailed Mann-Whitney test to determine whether changes in a hydrogeomorphic variable were statistically significant. The Mann-Whitney tests whether a randomly selected sample is less than or greater than a second sample or population. A test sample consisted of all observations of a given variable along a confining margin which were tested against the all measurements of that variable in the full river and the geologically defined sub-section respectively (Figure 1).

Results

Channel Morphology & Confinement

For the full study area, 8.0% of the channel is anthropogenically confined on one bank and 2.8% is confined on both banks. In the upstream alluvial, high-use area 16.4% of the channel is anthropogenically confined on one bank and 5.5% is confined on both banks. In the downstream, low-use area there are no single-bank anthropogenic confinements and 0.1% of the channel is confined on both banks. In the alluvial, high-use portion of the study area approximately 42% of the channel appears incised. Table 1 provides an overview of river characteristics for the entire river and for the separate geologic and land use classifications.

Figure 5 shows the downstream trends for each of the geomorphic variables. There is no downstream trend in width or slope. Width has the highest deviation in two locations, between 0 and 65 kilometers (64.2 meters) and between 100 and 115 kilometers (63.2 meters). Within the most heavily developed alluvial section near Grants Pass (RKM 65 – 100) widths are narrow and similar to those seen in the downstream, geologically confined section (RKM 130 – 175) and the two sections have similar variability: 18.7 in the anthropogenically confined (RKM 65 – 100) section and 19.1 in the naturally confined section (RKM 130 – 175). Between these two sections (RKM 100 – 130) is a relatively short section dominated by agriculture which appeared to have low anthropogenic impacts relative to upstream, alternating point bars and a general increase in channel width and width variability. The graph of slope illustrates the pool-riffle sequence found throughout the Rogue River. In the area with the most confining margins and areas of incised channel (RKM 70 – 95) channel slope is consistent (a flat line in Figure 5) punctuated by discrete riffles and rapids. However, in the comparable naturally-confined section there is a much greater spatial variability in slope and no places where

slope is consistent over relatively long areas. The most variability in unit stream power is located approximately at river kilometer 150 which marks the beginning of the Wild and Scenic River corridor and a more bedrock-controlled channel form with frequent rapids.

The trends in the relative depth model are similar to those of channel width. Depths have a smaller variability of 0.68 meters in the most heavily developed alluvial section compared to a variability of 1.3 meters in the alluvial portion of the channel just upstream. We did not notice a significant impact on channel form as a result of tributaries.

The Mann-Whitney statistical analysis suggests that, for single-bank and both-bank confinements some of the confining features result in a statistically significant difference in one or more of the hydrogeomorphic variables, but not all of the confining features do. This is true when confining features are compared to the full-river dataset and the relevant land-use sub-section. We use the threshold of $p < 0.05$ to define statistical significance at a 95% confidence level of results in support of the hypotheses. Results are only classified as statistically significant if the difference between the sample and population is in the expected direction. There are not any clear patterns in which confining features generate a statistically significant result for any given geomorphic variables. For example, a significant decrease in width at a given confinement may not result in a significant increase in unit stream power or slope.

We conducted a statistical test for each hydrogeomorphic variable using the full river data set and the reach-specific data sets at each confining margin. The purpose of these tests was to determine if a change in a given hydrogeomorphic variable was statistically significant relative to the full river, and relative to each sub-section which

allowed us to control from geology. A given hydrogeomorphic variable at a given confining margin (e.g. width) was compared to the median value for the full river and the geologic sub-section the sample came from. Table 2 shows each of the confining features, the geomorphic variable and the p-value based on the appropriate reach. The number of statistically significant confining features changes depending on the geomorphic variable in question. In the alluvial, high-use area the number of significant single-bank confinement widths is eight, compared to nine when considering the full river. The number of significant unit stream power values decrease from thirteen compared to the full-river to seven when using the appropriate sub-section. Slope has a slight increase in the number of significant confinements from five in the full-river dataset to seven compared to the specific section. Relative depth also had a small change of seven significant confinements when compared to the full-river dataset to eight. When considering both-bank confinements the change in the number of confinements with a significant change in the geomorphic variable are generally smaller. The largest shift is unit stream power, where seven of the confining features are significant when compared to the full-river and only four when based on the land-use section they occur in.

Gravel Bars

We photographed a total of 60 gravel bars in the study area requiring 30 to 200 photographs per bar. Of those, five could not be processed in BASEGRAIN because grain sizes were too small for individual clast detection (1 gravel bar), too much vegetation for clast identification (2 gravel bars), or poor photogrammetric alignment and therefore an unreliable orthophotograph (2 gravel bars). The two gravel bars with poor photograph alignment were all captured using the camera-on-a-pole where it was not

possible to check for appropriate photograph overlap in real-time. The results of the ANOVA test comparing the D_{16} , D_{50} and D_{84} gravel sizes computed using BASEGRAIN to those from the 2011 USGS survey (Jones et al., 2011) suggest that the two data groups are not statistically different, with a p-value of 0.65; well above 0.05 which is the common indicator for statistically unique samples (Figure 5).

Within the most heavily urbanized area at Grants Pass the gravel bar density is on average 0.37 gravel bars per kilometer over the 35 kilometers. The naturally confined section has an average gravel bar density of 0.26 per kilometer over 45 kilometers. The alluvial portion of the low-use section has a gravel bar density of 0.48 per kilometer over 23 kilometers. The Getis-Ord General G test of spatial clustering reveals a random spatial pattern of gravel bars through the Rogue River study area with a z-score of 0.06.

However, within the random distribution there are localized hot and cold spots. The two gravel bars in the middle of Grants Pass have D_{84} values larger than the gravel bars immediately upstream and downstream which fall within the alluvial valley. The section-averaged D_{84} values are very similar regardless of how sections are divided, between 98.2 mm and 99.8 mm. The standard deviations for each of the three study area categories (full river, upper alluvial, lower naturally confined) does show some distinction in particle size distribution, with the alluvial, high-use section having the lowest standard deviation of 10.8 mm and the natural, low-use section a variation of 19 mm.

Discussion

This study examined the impact that anthropogenic lateral channel confinements have on channel form. We hypothesized that width, sinuosity and slope would decrease while unit stream power, D_{84} and depth would increase as a result of confinement. At

certain single-bank and both-bank confinements this appears to be true. Over the reach we surveyed the commonly observed longitudinal trends in channel form like downstream hydraulic geometry (Leopold & Maddock, 1953) did not exist in this river. For the entire study, the downstream hydraulic geometry relation scaling exponent for width is below the expected range of 0.3-0.5 for alluvial channels (K. Gran & Montgomery, 2001). When dividing the study area into geologically similar reaches those that are characterized by alluvial processes do exhibit scaling exponents in-line with those expected by downstream hydraulic geometry. This is especially noteworthy for the reach beginning just downstream of Grants Pass and ending at Jump-off Joe Creek as the scaling exponent for the reach upstream is below the expect range (0.07). This further suggests that the lateral channel confinements associated with Grants Pass are resulting in a quantifiable impact on channel form.

However, isolating the geomorphic impacts of confining margins from the legacy impacts of dams, floodplain gravel mining and urbanization poses a challenge. One of the principle challenges is the collocation of channel incision and anthropogenic confinement; channel incision frequently being observed in the context of anthropogenic impacts on fluvial systems. The result has been channel incision which is frequently seen in such scenarios (Paul & Meyer, 2008; Petts, 1985; Simon & Rinaldi, 2006). As Grants Pass developed, the channel has become more confined (Figure 6). To prevent lateral bank erosion like that seen in the portions of the valley still used for agriculture, there has been bank armoring in many places, reinforcing channel incision. Figure 6 shows a set of paired aerial images comparing Grants Pass and the surrounding area in 1939 to the NAIP imagery. In Grants Pass the pattern of geomorphic channel variables of width,

slope, and the relative depth model all support the channel simplification anticipated from a confined channel where sediment supply is less than the transport rate.

Geomorphic Variables

The statistical significance of a single confinement observation is related to which population it was compared to; the full river or one of the sub-sections. When compared to the full river, more of the confining features resulted in p-values supporting H_A than when compared to the two geologic and land-use sections independently. This is not surprising given the larger range and higher standard deviations of a given geomorphic variable when considering the diversity of geologic and land-uses in the full river. This also suggests that within each sub-section there is more homogeneity in the geomorphic variables as supported by the standard deviations for each variable (Table 1).

The homogeneity of the geomorphic variables (Figure 5) within the heaviest land-use portion of the study area (RKM 65-100) is contrasted with the geologically-similar areas upstream (RKM 25 – 50) and downstream of Grants Pass (RKM 100 – 130). The upstream and downstream sections appear to have overall wider active channels and more heterogeneity associated with the pool and riffle sequences that characterize the river (Richards 1976). The downstream section (RKM 100 – 130) is dominated by the same alluvial deposition geology as that upstream in Grants Pass, however, downstream of Grants Pass there are no single-bank confinements and the dual-bank confinements are bridge abutments where bedrock is also a naturally confining feature. The difference in geomorphic diversity between the two similar geologic sections with different levels of anthropogenic confinement supports the hypothesis that lateral channel confinement is resulting in a decrease in channel heterogeneity expressed here most clearly as a decrease

in channel width. In the geologically-similar area upstream of Grants Pass, the variance in width is greater than in the Grants Pass area. Similarly, downstream of Grants Pass, width and the variance in width are also greater. Trends in slope do not show as clear a relationship between confinement. Confining margins which had a statistically high slope frequently also had a bedrock rapid someplace within the confinement. Through much of Grants Pass (RKM 65 – 100) the Rogue River flows along a bed of cemented gravels which provides some vertical confinement (Jones et al., 2011). The slope of this resistant layer may also be contributing to those areas with a statistically high slope in confining margins.

Unit stream power in the alluvial upper half of the study area does not appear to be strongly related to the decrease in width associated with the confined, incised channel (RKM 75) (Figure 5). This is likely due to the fact that this section (RKM 75) is also frequently low slope which is exerting a more dominate control in the unit stream power equation than width (equation 1). The confined channel sections where unit stream power has a statistically significant increase are those locations where riffles occur coincident with confining feature. At these riffles and rapids, slope can change an order of magnitude over relatively short longitudinal distances (eg: 0.0001 – 0.001) while over the same distances width values will only vary by 10's of meters.

The smaller variance in the alluvial section of the relative depth model (Figure 5) support the hypothesis of a more homogeneous channel as a result of channel confinement and incision. The hypothesized local increase in depth as a result of confining features does not appear in our study area. The local increase in depth signal is most likely lost to the more pervasive and extreme trend of uniform channel incision to

the layer of resistant cemented gravels (Jones et al., 2011). The two deepest points in the alluvial section (RKM 62 & 66) are both located at narrow points in the channel with bridge crossings, places where highly localized anthropogenic and geologic confinements produce deep scour pools.

Gravel Bar Analysis

The use of a UAV and Structure-from-Motion in combination with digital photoseiving proved to be effective as a robust analytical approach to quantifying gravel sizes over large study areas. This workflow offers a more time-efficient approach than hand measurement in the field with results that compare favorably to hand samples.

Through the study area we do not observe a trend of downstream fining at any size as predicted by downstream hydraulic geometry (Leopold & Maddock, 1953). The size of exposed gravels within the anthropogenically confined section at Grants Pass (Figure 5) is larger than those unconfined areas immediately upstream and downstream but this does not represent a statistically significant increase. The smaller size variance and larger size in D_{84} values of gravel bars in Grants Pass suggests higher stream power and less fine material, however the small number of gravel bars in this section (two) means this interpretation isn't conclusive. Gravel bar frequency in Grants Pass is lower than those areas upstream and downstream with comparable geologic and valley controls. Within the Grants Pass corridor the frequency of gravel bars most closely resembles that of the naturally confined section downstream (RKM 130) which suggests that despite a general lack of significant increases in unit stream power at confinements, similar hydraulic conditions to the naturally confined reach may exist.

We do not believe that gravel supply is limiting the frequency of gravel bars in the Grants Pass area. There is a greater number of likely sediment sources (tributaries) upstream of Grants Pass than downstream suggesting that there is a supply of mobile gravels in the Rogue River. Additionally, the number of gravel bars per kilometer is higher in places upstream and downstream of Grants Pass. Channel incision and armoring of banks creates a channel form where the lateral floodplain space for gravel bar development does not exist. The gravel bars which are present in the Grants Pass areas are located where active channel width is higher, occurring at the confluence of Evan's Creek, located east of Grants Pass (Figure 1), and near the constructed boat ramp in the heart of the city.

Conclusion

This study provides insight into the complicated role that anthropogenic confinements have on channel morphology and gravel sizes. However, determining direct causal relationships between a given metric (e.g. channel width) and a signal (e.g. absence of gravel bars) proved analytically challenging. The anthropogenic influence on channel form is intrinsically linked to the natural, geologic controls on the river. A history of dams on the mainstem and tributaries of the Rogue River likely resulted in channel incision (Petts, 1985; Petts & Gurnell, 2005), incision which was potentially reinforced by geologic controls such as cemented gravels and volcanic intrusives (Jones et al., 2011). The lateral channel reinforcement at anthropogenic confining margins further prevents lateral adjustment.

There is a long tradition of studying the impacts that humans have on the modification of fluvial systems. Much of that focus has been on the impact of dams as they offer a

spatially discrete break which allows straight-forward comparisons to be made between channel properties upstream of the dam and those downstream. This study examines the impact of lateral channel confinements on a suite of geomorphic variables derived from GIS data and field work spanning a roughly 200-kilometer study area. From this study it is clear that a legacy of human activity along the Rogue River, and ongoing urban pressure have resulted in significant modification of the channel form. In many places, lateral channel confinements resulted in significantly narrow channels. However, the most notable impact of the anthropogenically confined reaches was the lack of channel variability. This is most apparent when comparing width values in the anthropogenically confined reach to those geologically similar reaches upstream and downstream. The variability in depth in the naturally confined as compared to the heterogeneity of depths in the anthropogenically confined reach all suggest that the confining margins decrease channel complexity and likely habitat diversity. These changes are a result of anthropogenic channel confinement and the legacy of dams on the river. Some additional lateral stability is likely attributable to areas of cemented gravels in the area of Grants Pass (Jones et al., 2011). In the less heavily developed sections upstream and downstream of Grants Pass channel morphology was found to have higher heterogeneity indicating a more complex channel. The most heavily developed portions of the study area exhibited a high degree of homogeneity in each of the geomorphic variables. This is indicative of poor channel complexity as a result of incision and therefore lateral channel confinement. Through the most intensively anthropogenically confined reaches (RKM 75) width, slope and depth have low variability. This sits in contrast to those locations upstream and downstream (RKM 50 and 100) where variability in these variables is greater. Even with

geologic confinement (RKM 160) where width variability is similar to that upstream we still see greater variability in slope and depth.

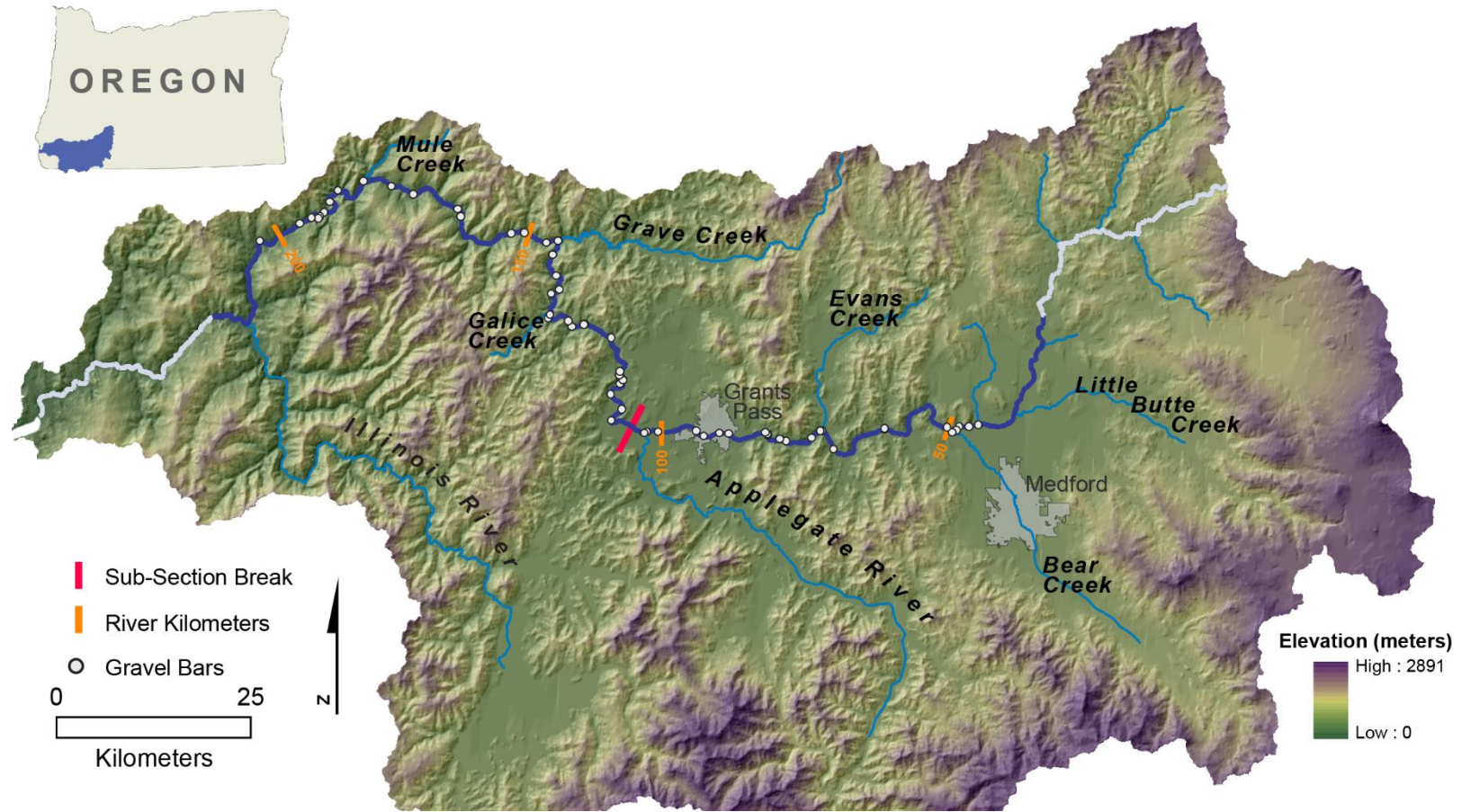


Figure 1. The Rogue River sits in the Southwest corner of Oregon (upper left). The study area encompasses the darker blue portion of the streamline. The perpendicular red line indicates the break between the upper, alluvial section and the lower naturally confined section. The study area consisted of roughly 200 kilometers of river encompassing wide unconfined alluvial valleys with low anthropogenic activity, anthropogenically confined alluvial valleys, and naturally confined sections.



Figure 2. An example of an incised channel in the Rogue River. This photo taken at approximately river kilometer 50. Smoke from near by forest fires is clearly visible.

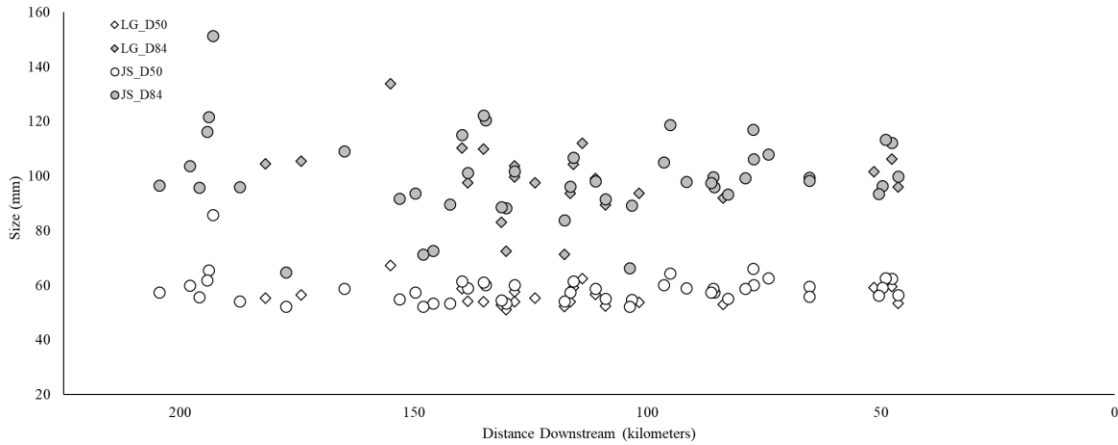


Figure 3. Scatter plot of D₅₀ and D₈₄ gravel size thresholds as computed in BASEGRAIN by research assistant LG (square) and JS (circle). The empty symbols show D₅₀ and filled shapes are D₈₄. The highest concentration of duplicated bars is in the middle of the figure, roughly between 108 to 140 meters downstream. A single-factor ANOVA analysis of the gravel bars generates a p-value of 0.68, suggesting that the results are similar.

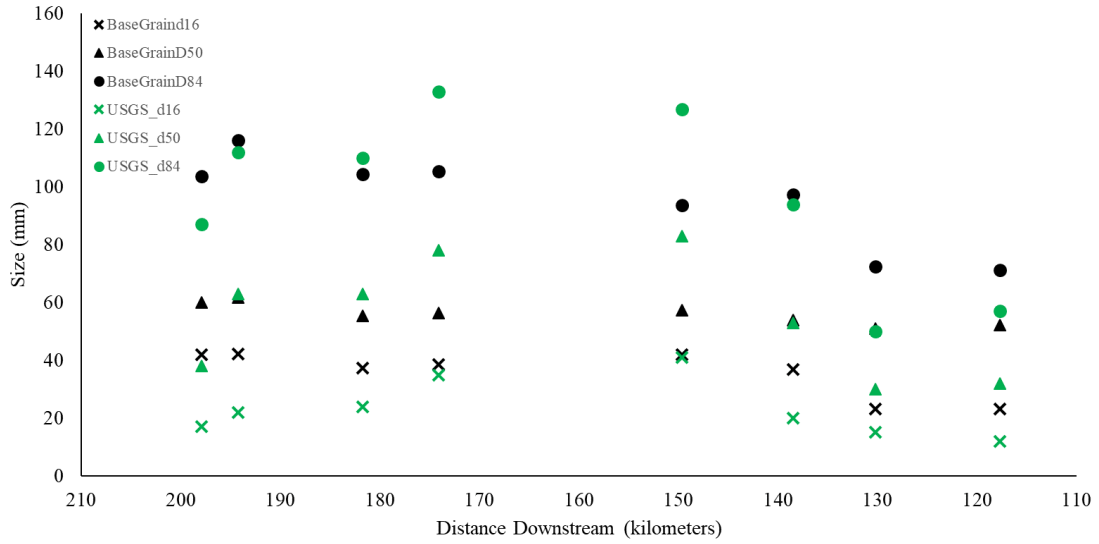


Figure 4. Gravel size metrics for all of the gravel bars the USGS hand sampled gravels in 2011 which we duplicated sampling as part of this study. Each size threshold is denoted by the same symbol. The USGS samples are green and our values are in black. An ANOVA test revealed that the two data sets are not statistically different with a p-value of 0.65.

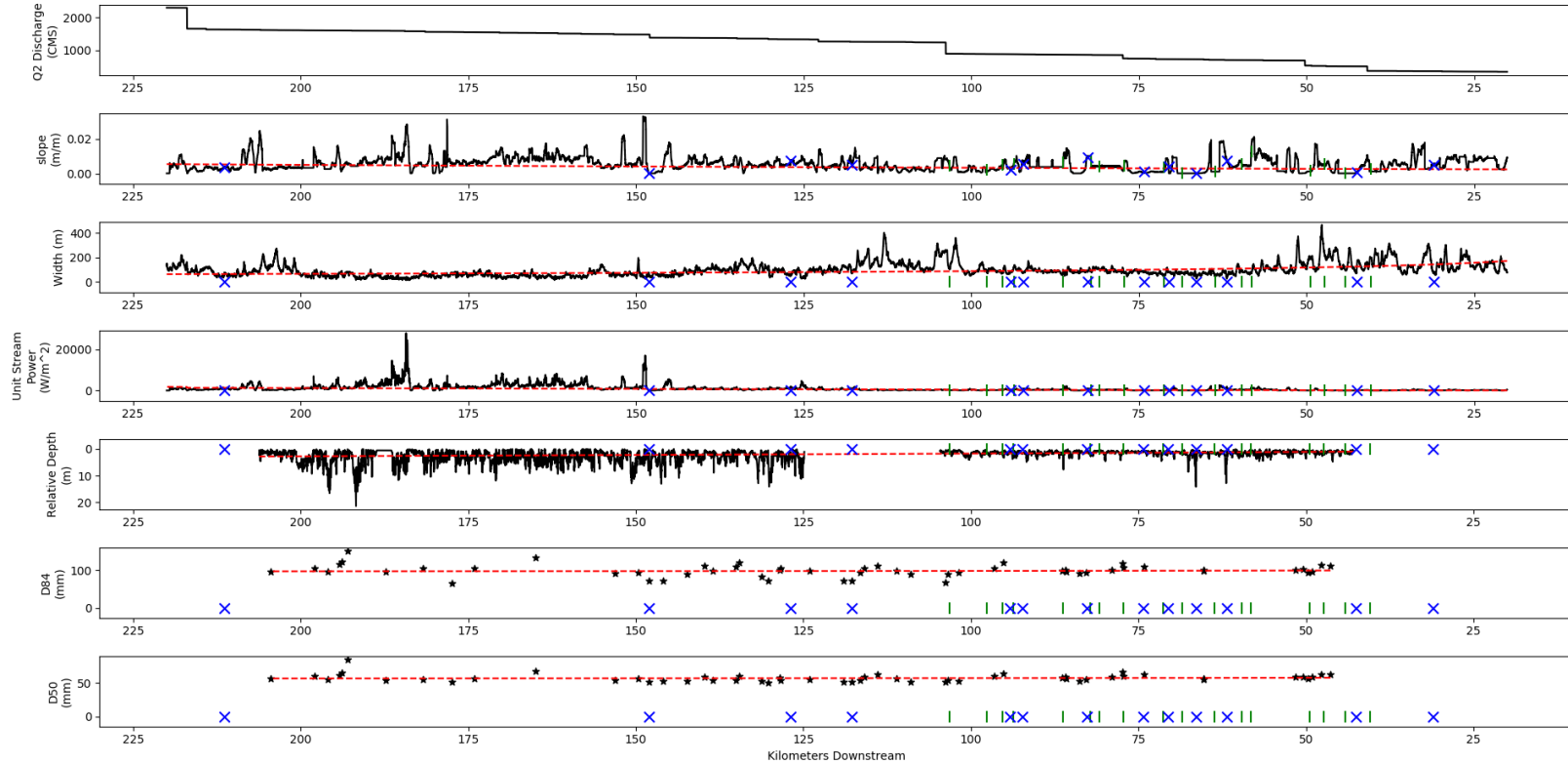


Figure 5. Plots of each of the hydro-geomorphic variables measured and computed for the study area. Grants Pass is located at RKM 75. The gap in the relative depth model (sub plot 5) is due to a sensor error resulting in no depth data. Blue X indicates locations where both banks have an anthropogenic confinement and the green vertical lines are locations where only one bank is anthropogenically confined. The markers indicate the center point of the confining margin and do not represent the distance over which the confinement occurs. Natural confinement begins at RKM 150 and extends nearly continuously to RKM 175. Water flow is from right to left and distances are in kilometers.

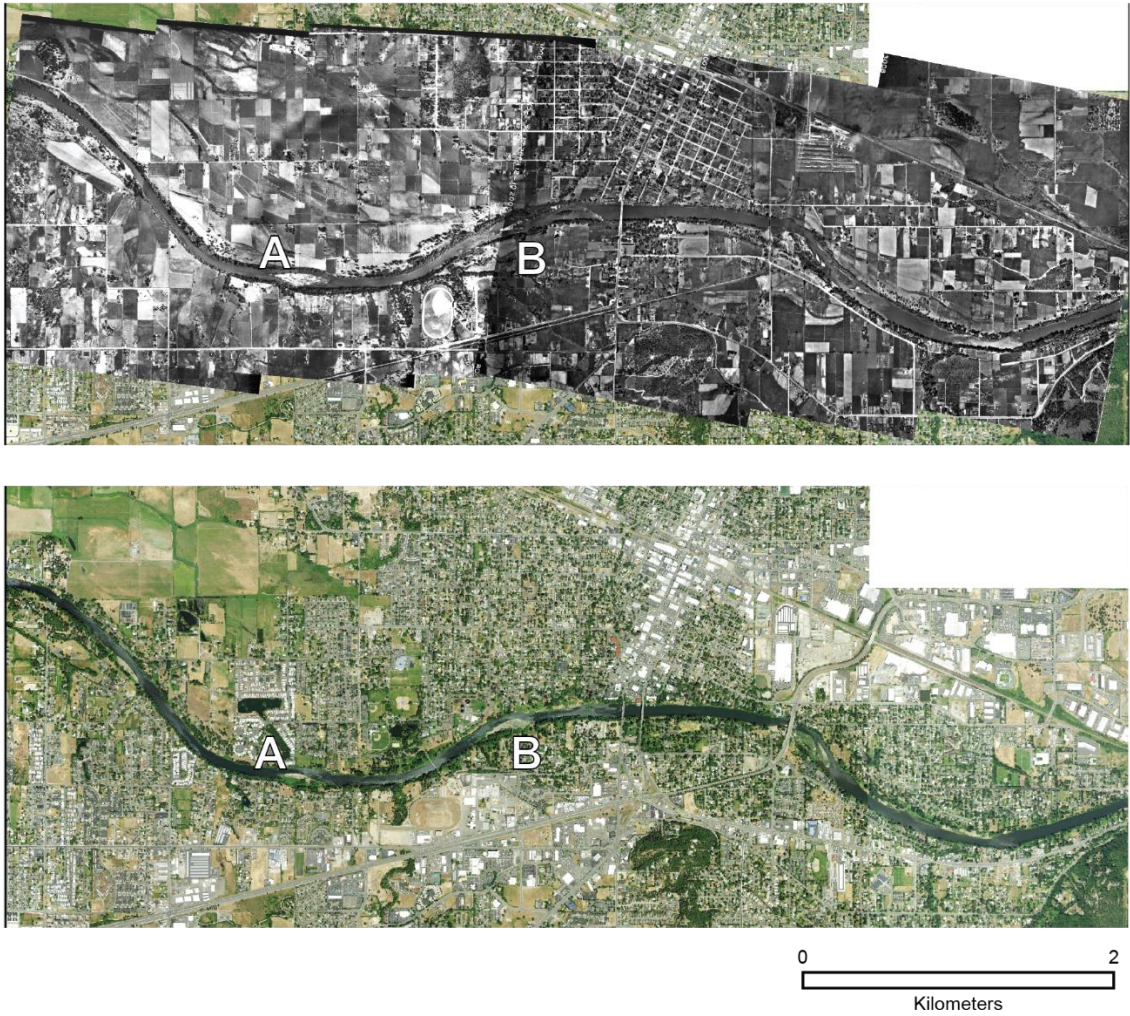


Figure 6. Aerial imagery of Grants Pass from 1939, and 2016 NAIP imagery of the same area. Notice that gravel bars have decreased in area (A, B) during the same time period that Grants Pass has expanded. At B the unvegetated, mid-channel gravel bar has connected to the left bank and is becoming vegetated.

Full River

Statistic	Width (m)	Slope (m/m)	Unit Stream Power (w/m ²)	Relative Depth (m)
mean	99.32	0.006	1030.83	2.60
median	87.31	0.005	505.16	1.79
standard deviation	55.79	0.004	1569.82	2.23

Alluvial, High-Use Sub-reach

Statistic	Width (m)	Slope (m/m)	Unit Stream Power (w/m ²)	Relative Depth (m)
mean	119.28	0.005	287.69	1.50
median	100.00	0.004	203.44	1.32
standard deviation	59.39	0.004	314.46	0.96

Mixed Geology, Low-Use Sub-reach

Statistic	Width (m)	Slope (m/m)	Unit Stream Power (w/m ²)	Relative Depth (m)
mean	84.32	0.006	1588.75	3.41
median	71.88	0.005	1006.43	2.90
standard deviation	47.70	0.004	1874.72	1.01

Table 1: Reach and sub-reach scale summary statistics for each of the hydrogeomorphic variables.

Confinement location	Number of banks confined	Full River p-values				Alluvial, High-use Sub-section p-values				Mixed Geology, Low-use Sub-section p-values			
		Width	Slope	Unit Stream Power	Relative Depth	Width	Slope	Unit Stream Power	Relative Depth	Width	Slope	Unit Stream Power	Relative Depth
31.00	2	1.000	0.056	0.000	0.000	1.000	0.000	0.013	0.000				
40.45	1	0.000	1.000	0.000	0.003	0.000	1.000	0.000	0.000				
42.58	2	0.650	1.000	0.000	0.000	0.998	1.000	1.000	0.000				
44.21	1	0.000	1.000	0.000	0.000	0.001	1.000	0.000	0.000				
47.39	1	0.000	0.002	0.000	0.000	0.000	0.000	0.000	0.000				
49.49	1	0.000	1.000	0.000	0.000	0.000	1.000	0.000	0.000				
58.25	1	0.310	0.000	1.000	1.000	1.000	0.000	1.000	1.000				
59.63	1	0.723	0.000	0.095	1.000	1.000	0.000	1.000	1.000				
61.86	2	1.000	0.000	1.000	0.001	1.000	0.000	0.000	0.000				
63.67	1	1.000	1.000	0.000	1.000	1.000	1.000	0.000	1.000				
66.44	2	1.000	1.000	0.000	0.000	1.000	1.000	1.000	0.000				
68.54	1	1.000	1.000	0.000	1.000	1.000	1.000	0.000	1.000				
70.60	2	0.809	0.999	0.000	0.379	1.000	0.953	0.261	0.457				
71.29	1	1.000	1.000	0.000	0.000	1.000	1.000	0.999	0.000				
74.29	2	1.000	1.000	0.000	0.000	1.000	1.000	1.000	0.000				
77.26	1	0.969	0.999	0.000	0.001	1.000	0.152	1.000	0.000				
80.89	1	0.000	0.998	0.000	0.000	0.041	0.052	1.000	0.000				
82.16	1	0.211	0.000	0.995	1.000	1.000	0.000	1.000	1.000				
82.64	2	0.042	0.000	1.000	0.000	0.997	0.000	0.000	0.000				
86.30	1	0.633	0.015	0.812	1.000	1.000	0.000	1.000	1.000				
92.30	2	0.000	0.000	0.044	0.003	1.000	0.000	0.000	0.000				
93.66	1	0.000	0.016	0.025	1.000	0.000	0.000	1.000	1.000				
94.16	2	0.504	1.000	0.000	0.001	0.986	0.995	0.383	0.000				
95.31	1	0.020	0.608	0.013	1.000	1.000	0.000	1.000	1.000				
97.65	1	0.000	1.000	0.000	1.000	0.000	1.000	0.000	1.000				
103.24	1	0.000	0.998	0.000	0.000	0.000	0.132	1.000	0.000				

Confinement location	Number of banks confined	Full River p-values				Alluvial, High-use Sub-section p-values				Mixed Geology, Low-use Sub-section p-values			
		Width	Slope	Unit Stream Power	Relative Depth	Width	Slope	Unit Stream Power	Relative Depth	Width	Slope	Unit Stream Power	Relative Depth
117.81	2	0.989	0.214	0.996		1.000	0.010	0.000					
126.91	2	1.000	0.000	1.000						0.997	0.001	0.999	
148.01	2	1.000	1.000	0.000						0.987	1.000	0.000	
211.34	2	0.975	0.923	0.963						0.562	0.990	0.210	

Table 2: The p-value from the Mann-Whitney test for each hydro-geomorphic variable within each confined reach is displayed. P-values are for the variable compared to all values of that variable in the full study area and the sub-section it occurs in. The location of the confining feature is denoted in the first column as kilometers downstream. There are seventeen single-bank confinements and thirteen locations with a both-bank confinement. There are no single-bank anthropogenic confining features in the mixed geology, low-use sub reach. Reported values are the p-value indicating statistical significance of a given confinement within the reach it is located. The break between the alluvial, high-use sub reach and the mixed geology, low-use sub-reach is at river kilometer 104.

BRIDGE: CHAPTER 2: THE IMPACT OF ANTHROPOGENIC LATERAL CHANNEL
CONFINEMENT ON CHANNEL FORM AND CHAPTER 3: A RIVERSCAPE MAPPING
APPROACH TO THE SEDIMENT LINKS CONCEPT

Chapters 2 and 3 are closely related. They both look at longitudinal patterns of the hydrogeomorphic variables of the Rogue River. Chapter 2 focuses on the role that anthropogenic forces have on controlling channel form. Anthropogenic activity can impact the movement of sediment and water in the channel and adjacent floodplain. Changes to the hydrology and sediment transport in a fluvial system can trigger changes in channel morphology. Chapter 3 focuses on the natural processes which impact channel form, specifically tributaries and hillslope processes as mechanisms for sediment delivery. The addition of new sediment from alluvial and colluvial sources can have an impact on channel form and the rate of certain longitudinal trends such as downstream fining. In addition, tributaries deliver additional discharge to the main channel, altering the hydrologic regime. These natural processes work in tandem with anthropogenic forcing mechanisms to control channel form.

CHAPTER III

A RIVERSCAPE MAPPING APPROACH TO THE

SEDIMENT LINKS CONCEPT

1.0 INTRODUCTION

Fluvial geomorphology has a long history of using broad conceptual frameworks to characterize watershed scale trends such as downstream hydraulic geometry (Leopold & Maddock, 1953), the river continuum concept (Vannote et al., 1980), channel-reach morphology (Montgomery & Buffington, 1997) and the sediment links concept (Rice, 1998). As described by Fonstad and Marcus (2009) and Carbonneau et al. (2012), increasing data resolution continues to illustrate a far more complex geomorphic and hydrologic landscape. Despite this, gradual, basin-wide trends continue to be referenced as the “expected” pattern against which morphologic alterations are judged. The Rosgen classification scheme (Rosgen, 1994), a common basis in fluvial restoration, relies on smoothly varying trends in channel form. Many landscape evolution models also rely on smoothly varying trends. This approach can have high accuracy for very generalized basin-wide descriptions of channel form in fine-grained alluvial valleys where autogenic processes dominate and external controls are minimal. However, these generalized trends do not accurately predict the spatial heterogeneity seen across the diversity of channel forms in existence, at the resolution we can now quantify (Fonstad & Marcus, 2010; Rice, Greenwood, & Joyce, 2001). What is more frequently observed from measurements of channel width, depth and particle size distribution is a far noisier signal. Local

variability in channel form dominates at small scales making the gradual, longitudinal, basin-wide trends more complicated than watershed scale conceptual models reveal.

Downstream hydraulic geometry proposes general trends in the hydrogeomorphic variables which occur at a watershed scale (Leopold & Maddock, 1953). Leopold and Maddock state that as one travels from the upper to lower portions of a watershed discharge will increase in response to increasing catchment size. In the downstream hydraulic geometry model, the channel responds to increasing discharge with an increase in channel width and depth. At the same time, particle sizes decrease as a result of abrasion, hydraulic sorting and weathering. Meanwhile, slope decreases with the decrease in relief (Knighton, 1998). Estimating discharge as a function of watershed area implies generally smooth increases in discharge moving downstream punctuated by abrupt jumps in watershed area, and discharge. If channel form is a function of hydraulics, other variables in downstream hydraulic geometry should undergo a commensurate change.

Other characterizations such as channel-reach morphology (Montgomery & Buffington, 1997) and the river continuum concept (Vannote et al., 1980) seek to address the heterogeneous nature of rivers, but still discuss distinct and uniquely identifiable reaches which are a function of idealized downstream hydraulic geometry relationships within a watershed. The sediment links concept (Rice, 1998; Rice & Church, 1998) is variation on downstream hydraulic geometry (Leopold & Maddock, 1953) that does not rely on characterizing the channel type morphology as a function of its distance from the basin divide. Instead of a continuous downstream fining from the upper to lower watershed, the sediment links concept suggests that the pattern of downstream fining may be periodically interrupted by local sources of new material (e.g. an underlying glacial

deposit, landslides, bank failure) or discharge from tributaries. There are two processes by which a new material may cause an interruption in the process of downstream fining: (1) the new material deposited into the channel is of a sufficient size as to disrupt the pattern of downstream fining in the mainstem (e.g. it is larger than that in the mainstem). The addition of new material could be infrequent but deliver large quantities (e.g. landslide) or is delivered with a frequency such that it is a continuous source which is constantly delivering new material (e.g. landslides or bank failure) or (2) in the case of a tributary, it has a sufficient discharge such that the transport capacity downstream of the confluence increases with the additional discharge. The increase in transport capacity is sufficient such that clast sizes which could not be transported upstream of the confluence are mobilized, leaving larger clasts, relative to those upstream, in the channel. Either scenario will result in an increase in gravel sizes at the confluence and potentially an increase in slope locally (Knighton, 1998; Leopold et al., 1992).

A primary challenge in reconciling basin-wide conceptual river models and more quantitative, location specific observations is the fundamental spatial disparity in observation. As the spatial scale of observation increases, local variability in channel morphology is missed or “smoothed out” and generalized longitudinal trends become more obvious. However, as spatial scales decrease to the scale of individual gravels and near-continuous width and depth measurements, channel heterogeneity makes large-scale trends less and less apparent. A growing body of literature establishes the importance of the conceptual framework of riverscapes as holistic systems which exist simultaneously at scales from microhabitat to watershed (Carbonneau, Fonstad, Marcus, & Dugdale, 2012; Fausch, Torgersen, Baxter, & Li, 2002; Thorp et al., 2010; Thorp, Thoms, &

Delong, 2006). Hyperscale analysis requires intensive, high-resolution data over extensive areas so that analysis can be conducted simultaneously at and across spatial scales (Fonstad & Marcus, 2010).

Structure-from-Motion (SfM) and digital photosieving are tools that allow grain-by-grain measurement for entire gravel bars (Chang & Chung, 2012; Langhammer, Lendzioch, Miřijovský, & Hartvich, 2017; Millidine, Malcolm, & Gibbins, 2010; A. S. Woodget, Fyffe, & Carbonneau, 2018). This approach to data collection allows us to more efficiently characterize longitudinal trends in gravel sizes for all gravel bars in the study watershed. If one travels via the river, it is possible to sample gravel bars continuously rather than being limited to those that have road access, providing the opportunity to create a more complete picture of the variations in sediment and local morphology. We can integrate field data with high-resolution remote sensing datasets to create the spatially intensive data necessary to address questions concerning the longitudinal variation in width, depth, slope and the spatial pattern of sediment sizes within and between gravel bars. Observing patterns across spatial scales is not possible with discrete data sets. Hyperscale data are critical to examining the conceptual models which have been a foundation of fluvial geomorphology for decades to evaluate under what conditions they still provide useful insight into the process-form relationship.

This study integrates Structure-from-Motion, digital photosieving techniques, depth measured in the field, and remote sensing imagery to create a hyperscale data set of the Rogue River, a gravel bed river in the Pacific Northwest, USA. We consider all potential sediment sources in the study area, recognizing that some potential sediment links may not create a quantifiable signal. In the context of the sediment links concept,

we examine whether and how sediment links and basin geology control gravel sizes and channel form: asking how tributary and hillslope sediment contributions will influence channel form and particle size distributions? Specifically, we evaluate the following hypotheses:

- (H1) Tributaries will result in an increased gravel size at their confluence with the Rogue River.
- (H2) Non-tributary sediment sources will produce larger gravel sizes where they intersect the proximal channel compared with those gravel bars upstream.
- (H3) Tributary sediment links will result in an increase in channel width and hillslope processes (e.g. debris flows and landslides) will trigger a decrease in channel width.
- (H4) Tributary and non-tributary sediment links will generate an increase in slope.
- (H5) Channel depth will decrease locally at tributary and non-tributary sediment links.

Our hypotheses come from previous studies and our understanding of the process-form relationship. Our hypotheses concerning the size of gravels at sediment links (H1 and H2) come from Rice (1998). Our prediction for the behavior of channel width (H3) derive from a process-form based approach. An increase in discharge and the potential for small alluvial fan development within the active channel at confluences both suggest an increase in width (Knighton, 1998; Leopold et al., 1992). In contrast the addition of large volumes of immobile colluvium at hillslope derived sediment links would likely decrease channel width. Our final hypotheses regarding slope and depth (H4 and H5) also follow from a process-form understanding. The accumulation of alluvial and colluvial

material which is not transported downstream will eventually raise the elevation of the channel bottom, creating a decrease in channel depth (H5) and an increase in slope (H4). How, and at what spatial scales we characterize longitudinal trends in channel form is important for channel classification, hydraulic modeling and stream restoration. Too large a spatial scale of characterization and important complexity is lost. Too fine a scale and it becomes challenging to relate longitudinal connectivity to morphologic connectivity. This research seeks to improve our understanding across spatial scales of the impact of sediment sources as controls on channel form.

2.0 STUDY AREA

To accurately assess the impact of tributary and non-tributary sediment links on a fluvial system requires a river with a number of tributaries, and some knowledge of where hillslope activity has impacted the active channel. The Rogue River is a characteristic gravel bed river in the Pacific Northwest, USA (Figure 1) and flows through alluvial, metamorphic and sedimentary provinces (Figure 2). Frequent gravel bars throughout the study area allow use to map longitudinal trends in gravel sizes. The study area is comprised of an upper alluvial section with frequent gravel bars which flows over mobile and cemented gravels with occasionally bedrock outcrops. The lower portion is characterized by geologic lateral confinement with frequent bedrock outcrops controlling slope. Given the presence of in-channel bedrock and coarse gravels the majority of the study area is likely supply-limited (Jones et al., 2011). Tributary and non-tributary sediment sources occur throughout the study area, allowing us to examine their relationship with channel form in the context of downstream hydraulic geometry and

changing geologic landscape. In general, the Rogue River is a supply limited channel, having the stream competence to move more material than available.

The watershed is 13,350km² and made up of four geologic provinces: The High Cascades (14%), the Western Cascades (16%), the Coast Range (1%) and the Klamath Mountains (56%) (Jones et al., 2011). Much of the broad valley floor the Rogue River flows through is comprised of Quaternary sedimentary deposits and landslides. In many places it is broken up by a number of metamorphosed and intruded igneous plutons, dikes and sills. Upstream of the old Gold Ray Dam site is an area of lacustrine deposits from the former Gold Ray dam roughly 2 river-kilometers long. The further west one travels in the watershed, the less deformed and softer the Klamath terrain becomes suggesting the potential for the delivery of more material from sediment links. The spatially varying river valley context exerts large-scale controls on channel morphology with important implications for watershed scale trends.

In the eastern portion of the study area, the Rogue River valley is predominately alluvial and is bordered by harder volcanic and metamorphosed rocks. Downstream of the confluence with the Applegate River, the broad alluvial valley begins to narrow and the Rogue River becomes increasingly confined by ophiolite and sedimentary lithologies. The spatially varying river valley context exert large-scale controls on channel morphology with important implications for watershed scale trends. Within the study area are seven major tributaries: the Illinois River (2550km²), the Applegate River (1994km²), Bear Creek (930km²), Little Butte Creek (917km²), Evans Creek (580km²), Grave Creek (422km²) and Jump-off Joe Creek (282km²). There are an additional four small tributaries, Reece Creek (55km²), Mule Creek (77km²), Snider Creek (60.6km²) and

Galice Creek (61.9km²). Tributaries entering the Rogue River east of the Applegate River (Evans Creek, Bear Creek, Snider Creek and Little Butte Creek) originate in the older, more heavily metamorphosed portion of the Klamath Mountains suggesting less abrasion and therefore larger gravels. The Applegate River and Illinois River are the two largest tributaries. Rice (1998) suggest that this is a good indication of a sediment link, however in the lower portion of both of these tributaries Jones et al. (2011) not that they are likely transport limited meaning the readily available gravels may not reach the Rogue River. Figure 2 is a geologic map of the study area. From field observations and GIS we mapped fourteen non-tributary sediment sources including landslides, active bank erosion, and leftover hydraulic mining debris which are within the active channel. Channel forming flows are generated from winter frontal systems with base flows sustained by groundwater contributions from the upper Rogue River basin, supplemented by the only remaining dam, the William L. Jess Dam located 40 kilometers upstream of the study area (Jones et al., 2011).

3.0 METHODS

Downstream hydraulic geometry (Leopold & Maddock, 1953), the river continuum concept (Vannote et al., 1980) and channel reach morphology (Montgomery & Buffington, 1997) all suggest certain downstream trends in channel form, drawing large-scale trends from a series of discrete data points. To accurately improve our understanding of the heterogeneity in channel morphology requires a near-continuous longitudinal dataset. The goals of our field work were to collect the data necessary for computing particle size distributions, channel depth, and making observations of unmapped, non-tributary sediment sources. We use combination of remote sensing and

field data to plot longitudinal patterns in channel form. Combined with gravel size measurements of all exposed gravel bars, we can examine the role sediment links have on channel morphology and sediment size distribution across spatial scales.

3.1 Methodological Approach

This study integrated aerial imagery, remote sensing and field-based data. We used ten-meter National Elevation Dataset (NED) and 1.2-meter LiDAR data, aerial imagery from the National Agriculture Imagery Program (NAIP), soil maps from the U.S. Department of Agriculture (USDA), geologic maps from the Oregon Department of Geology and Mineral Industries (DOGAMI) and the 100-year flood inundation maps from the Federal Emergency Management Agency (FEMA) (Archuleta, Constance, Arundel, et al., 2017). We used these GIS data to digitize the active channel margin, extract channel slope, estimate the 2-year return interval discharge and compute unit stream power. We collected aerial imagery using a DJI Phantom 3 UAV and a Nikon D5200 digital SLR camera. Depth data was collected using a Seafloor Systems Hydrolite-TM single beam echo sounder paired with a Trimble GeoX7 handheld data collector.

3.2 GIS Processing

This study requires high resolution, spatially extensive data of multiple hydrogeomorphic variables to address the research question. Creating continuous maps of channel width and slope requires an approach which can be implemented at a basin-wide scale using all available data. GIS analysis for this study begins at the town of Shady Cove and ends downstream of the confluence with the Illinois River. Due to the spacing of river access sites, field work began at Touvelle State Park near White City and ends

upstream of the confluence with the Illinois River at Illahe. Mapping of the active channel, corresponding with the bankfull width, was based predominately on NAIP imagery, relying on the presence of active, unvegetated gravels and the type and presence of vegetation along the channel margin. We supplemented this with breaks in bank slope from LiDAR and soils data, including those characterized by the USDA as river wash (Harrelson et al., 1994). We used the FEMA floodplain maps as a reference point. At no point does the bankfull channel margin cross the 100-year floodplain, but in certain confined reaches they follow the same path. Distance downstream and channel width were derived from the digitized bankfull channel margin shapefile, converted to a four meter raster image, using the MATLAB program ChanGeom V0.3 (Fisher et al., 2012, 2013). ChanGeom computes a cumulative distance downstream based on pixel size centered within the rasterized active channel shapefile. Channel width is computed perpendicular to that center line at each pixel. The output of the ChanGeom program is a channel centerline and width measurement at every pixel. We extracted elevation at each centerline point from the NED data which we used to compute slope using a moving window. It is important that this window be large enough to capture elevation change in low-slope reaches without being so large as to smooth over small riffles and rapids. We built a semi-variogram to determine at what distance adjacent elevation values were no longer related, termed the range of a semi-variogram. This distance is derived from the range of the semi-variogram for elevation, where distances beyond 40 meters no longer see spatial autocorrelation. We therefore used a 40-meter window to compute slope. From our field observations we suspected that changes in slope, as a result of sediment links, may be smoothed over given the window size for our slope computation and the

subtle change in elevation at some riffles. Therefore, we digitized all named riffles and rapids in the study area based on Leidecker's (2015) river guide book which provides an independent source for the identification of channel slope breaks.

To identify non-tributary sediment links, we used a combination of previously mapped landslides from DOGAMI and field observations. GIS mapped landslides were included only when they intersected the active channel. We added unmapped landslides and debris flows from field observations where hillslope scars were present and colluvium was noted within the bankfull channel. An area with eroding mining debris (RKM 113) and the two kilometers of bank erosion (RKM 50) through the lacustrine deposits upstream of the old Gold Ray Dam site also came from field observations.

There are five USGS discharge gages on the Rogue River, two of which are within the study area, two upstream of the study area, and one just downstream of the study area. We used the log-Pearson Type III method to estimate the two-year return interval flood for all five gages (Bedient & Huber, 2002). We built a second-degree polynomial regression equation where drainage area at each gage is used to estimate the 2-year return interval discharge at that gage ($R^2=0.99$). For this study, we take the 2-year flood event to be the channel forming flow – that is, the flow which channel width, depth and gravel sizes are adjusted to (Knighton, 1998; Stock & Montgomery, 1999; Wolman & Miller, 1960). From the ten-meter NED data we computed a flow accumulation raster which we applied the polynomial equation to, generating a computed discharge at every pixel along the channel based on the size of the contributing area at that pixel. From the above variables we computed unit stream power (equation 1) to provide a physically based estimate of sediment competence (Bagnold, 1966; Phillips, 1989), where ω

represents unit stream power, ρ is the density of water, g is the gravitational constant, Q is discharge, S is slope and W is channel width.

$$\omega = \frac{\rho g Q S}{W} \quad [1]$$

The result of the GIS data processing is a spatial dataset with a point every four meters containing the northing and easting, distance downstream (km), elevation (m), channel width (m), channel slope (m/m), Q_2 discharge (cms) and unit stream power (W/m^2).

3.3 Field Data

Field work took place over nine days, in three trips, traveling 200 kilometers total of the Rogue River. We traveled during dam-controlled summer low-flows approximately $32.5 \text{ m}^3/\text{s}$ (95% exceedance) to maximize the number and size of exposed gravel bars. We stopped at each gravel bar and photograph all unvegetated portions of the gravel bar which we used to generate orthophotographs. Every attempt was made to travel in the channel thalweg so that depth data from the echo sounder represented the deepest point in the channel. However, this was not always possible due to rapids and other obstacles. The echo sounder and GeoX7 recorded a point every five seconds comprised of channel depth, northing, easting and elevation. Initial study design anticipated using the field collected GPS elevation data for water surface slope and channel elevation maps but poor precision in the Z direction, with elevation points changing by as many as 100 meters between adjacent measurements, meant that this was not possible. Depth measurements couldn't be accurately tied to an elevation datum, therefore depth is a relative depth model (RDM). This still allows us to address our

hypothesis that depth will decrease at sediment links (H5). The RDM still illustrates the distinction of pool-riffle sequences in the bathymetry, even without being able to tie the channel bottom to an absolute elevation above sea level.

Airspace and land management allow for the flight of UAVs from the beginning of the field work portion of the study area at Touvelle State Park to the confluence of Grave Creek. For all exposed gravel bars in this reach aerial imagery was collected using a DJI Phantom 3 UAV. From Grave Creek to the end of the study area at Illahe, the Rogue River flows through a designated Wild and Scenic River corridor which prohibits UAV operation. For gravel bars within this reach we walked the bars taking photographs with a Nikon D5200 DSLR on telescoping pole.

All gravel bars were photographed from heights between four and ten meters above ground level, for both photographic platforms, giving a horizontal and vertical ground resolution of 0.4 cm or better. Camera height for a given gravel bar was chosen based on visual estimations of the gravel sizes present, ensuring that individual clasts were clearly visible based on the POV screen. Each gravel bar was processed using Agisoft PhotoScan 1.4 (now Metashape) generating a sparse point cloud, dense point cloud and georeferenced orthophotograph for each gravel bar following well established best-practice (Carbonneau & Dietrich, 2017; Fonstad et al., 2013; M. R. James & Robson, 2014; Westoby et al., 2012). All gravel bars were exported as GeoTIFFs with one-centimeter resolution to standardize analytical scale between gravel bars. For the UAV based imagery we relied on direct georeferencing the orthophotographs as small ranges of uncertainty in absolute gravel bar location were deemed acceptable in exchange for the more efficient data collection in the field by not having to survey ground control

points at each bar (Carbonneau & Dietrich, 2017). The gravel bars photographed using camera-on-a-pole had ground control points taken using the Trimble GeoX7 so that they could be georeferenced. It took between 30 and 200 photographs to capture a gravel bar depending on the size of the bar and camera height necessary to capture gravels.

We analyzed gravel bar orthophotographs using BASEGRAIN 2.2 which is implemented in MATLAB. BASEGRAIN is a progressive edge detection algorithm which iteratively turns clasts to white and the shadowed intercostal spaces black, and converts the white raster area to individual vector polygons. It then computes the A axis, B axis, area, and orientation for each identified gravel, exporting these measurements as tabular data (Detert & Weibrecht, 2013; Detert & Weitbrecht, 2012). Small gravel bars ($<15\text{m}^2$) were processed as a single image. Large gravel bars ($>15\text{m}^2$) were broken into a series of adjacent, not overlapping 15m by 15m tiles. This was done to increase the processing efficiency of BASEGRAIN. We used the parameterization recommendations in the BASEGRAIN documentation concerning image processing thresholds at each of the five steps (Detert & Weibrecht, 2013; Detert & Weitbrecht, 2012). Before processing each image, vegetation and fines were masked. After processing the user can examine the partitioned image and mask, merge or split clasts based on their visual analysis of the image (see Figure 3). After processing, the 15m sample data tables were combined so that each gravel bar had a single table with all gravel data. From the data tables containing the size of all identified and measured gravels at a single bar, we computed the D_{16} , D_{50} and D_{84} . As a sensitivity analysis to the user-input portions of BASEGRAIN, two paid research assistants each processed 21 of the gravel bars. The gravel bar metrics were also

compared to hand sampling of gravel bars conducted by the USGS in 2011 (Jones et al., 2011) on duplicated gravel bars.

3.4 Analysis

Analysis of the hydrogeomorphic variables width, slope, unit stream power and relative depth relied on the non-parametric 1-tailed Kruskal-Wallis H test. A test area consisted of the data for a single variable adjacent to the identified sediment source, plus those values extending one mean channel width (80 meters) downstream of the source. An 80-meter window was chosen as the average distance of the range from semi-variogram plots for each of the variables except slope as explained in section 3.2. See Figure 4 for a sampling example. A sample was then tested against all values for the study area.

As an external check of the accuracy of BASEGRAIN we compared the D_{16} , D_{50} and D_{84} values we computed against hand-sampled USGS results from 2011 using single factor ANOVA. Gravel bar spatiality was analyzed using Getis-Ord General G to determine whether gravel bars were randomly distributed within the study area. Size based clustering of gravel bars was analyzed using Getis-Ord G_i^* .

Having traveled a number of rivers we have observed that riffles and rapids frequently occur at tributary confluences and places where hillslope activity interacts with the channel. Riffles and rapids are a hydrologic sign of an increase in channel slope and or roughness (Knighton, 1998; Leopold et al., 1992). We include the point location of all named rivers and rapids in the study area as an alternative indication of a break in channel slope which may not be quantifiable from our statistical analysis.

4.0 RESULTS

Our research on the Rogue River reveals a complex sediment landscape. Commonly observed longitudinal trends like downstream hydraulic geometry do not appear in any of the variables measured. For the entire study, the downstream hydraulic geometry relation scaling exponent for width is below the expected range of 0.3-0.5 for alluvial channels (K. Gran & Montgomery, 2001). Relative depth and slope both vary at short spatial scales with little to no lasting downstream impact due to sediment links. Width and unit stream power both have sub-reaches with higher spatial autocorrelation broken up by sub-reaches with high spatial variability. Discharge increases smoothly between tributaries, with abrupt jumps in discharge commensurate with the size of the tributary. However, the increase in discharge does not appear to correlate with changes to the other geomorphic variables (Figure 5). The downstream plot of D_{84} suggests that there may be some reaches with downstream fining (RKM 134 & 113, Figure 5) but these trends are subtle and are not clear in the plot of D_{50} (Figure 5). Many of the tributary and non-tributary sediment sources we identified produced a statistically significant geomorphic signal when compared to the study area median. However, statistical significance was not always caused by the geomorphic change we hypothesized, such as significant high slope values at a landslide caused by a bedrock outcrop rather than colluvial deposition. And in many cases a significant change in a variable which confirmed a hypothesis did not indicate that other, related variables at that location were significant. Some explanation may be related to the size and volume of the material in the sediment link. If the material contributed to the main channel from a sediment link is of a

size which can be transported by the Rogue River than a geomorphic signal may not persist.

We photographed 60 gravel bars in the study area using the UAV or camera-on-a-pole, each gravel bar requiring 30 to 200 photographs to capture. Structure-from-Motion processing generated usable orthophotographs for 55 gravel bars. Of the five bars we couldn't use, one had clast sizes which were too small to detect, two had vegetation which prevented gravels from being clearly distinguishable, and two suffered from poor photogrammetric alignment and were therefore unreliable. Comparisons to gravels bars hand sampled by the USGS in 2011 suggests that the BASEGRAIN analysis is an acceptably reliable method for analyzing gravel sizes. Using the BASEGRAIN computed D_{16} , D_{50} and D_{84} compared to the USGS reported values at the same gravel bars we computed a p-value of 0.65 (see Chapter 2, Figure 4). When we only considered D_{50} and D_{84} in the comparison, the p-value increased to 0.98. Knowing that BASEGRAIN is limited in its ability to detect the smallest class sizes, based on image resolution, we only considered D_{50} and D_{84} in our analysis. Depth measurements exist for the 200 kilometers of field-based study area except for a 20-kilometer section beginning at RKM 104 caused by a sensor error.

Not all tributary and non-tributary sediment sources will generate a quantifiable change in channel morphology indicating a sediment link. Here we test all potential sediment sources in the study area for the presence of a geomorphic signal of a sediment link. We then take a form-process approach in an attempt to better understand when and why a sediment link may or may not produce a quantifiable signal. We analyzed the

impacts of tributary and non-tributary sediment sources on a variety of hydrogeomorphic variables. The results of that analysis, in the context of our hypotheses, are below.

4.1 (H1) Tributaries will result in an increased gravel size at their confluence with the Rogue River.

Only three of the tributaries have a gravel bar located at the confluence with the Rogue River and have gravel sizes larger than those at the nearest upstream gravel bars; the sign of a significant sediment link according to Rice (1998). Evans Creek, Galice Creek and Mule Creek all have D_{50} and D_{84} sizes larger than the closest upstream gravel bar. The Applegate River, Bear Creek and Grave Creek all have gravel bars at the confluence with the Rogue River but gravels are smaller than those upstream. Reece Creek, Little Butte Creek, Snider Creek and Jump-off Joe Creek do not have gravel bars at the confluence. The Illinois River does have a gravel bar at the confluence but gravel size measurements do not exist for those gravel bars. Table 1 shows the sizes of each gravel bar in the study area.

4.2 (H2) Non-tributary sediment sources will have larger gravel sizes at the exposed gravel bar where they intersect the active channel.

Most non-tributary sediment sources do not have an associated gravel bar. The active bank erosion at RKM 50, the debris at the Flanagan Mine at RKM 113, landslide at RKM 142 and the landslide complex at RKM 203 all have associated gravel bars. Of those, only the Flanagan Mine results in gravel sizes larger than those at upstream gravel bars. The remaining ten non-tributary sediment sources do not have a gravel bar in close proximity (table 1).

4.3 (H3) Tributary sediment links will result in an increase in channel width and hillslope processes will trigger a decrease in channel width.

All tributaries which exhibited a statistically significant change in width did so as a predicted increase in width (Table 2). Evans Creek, Jump-off Joe Creek and Galice Creek confluences do not have mainstem widths which are statistically different than the median for the study area. The statistical results of non-tributary sediment links are less clearly defined. The active cut bank and Flanagan Mine debris both show a significantly high width, as do the landslides at RKM 196 and RKM 211. The remaining five statistically significant landslides are all significantly narrower than the median. An additional five landslides do not have a significant impact on channel width.

4.4 (H4) Tributary and non-tributary sediment links will generate an increase in slope.

Eight of the eleven tributary confluences have a slope which is significantly different than the median study area slope with 95% confidence. However, not all of those eight are due to slopes which are steeper than the study area median slope, as hypothesized. Bear Creek, Grave Creek and the Illinois River all have slope values which are statistically lower than the median slope. Reece Creek, Little Butte Creek, Evans Creek, Galice Creek, and Mule Creek are all significantly steeper than the median slope. Snider Creek, Jump-off Joe Creek and Mule Creek do not have a slope which is statistically different than the median. In addition to the statistical test we used the presence or absence of named riffles and rapids as a method for identifying locations with a local increase in slope. The only creek with a statistically high slope, but no named riffle at the confluence is Little Butte Creek. The remaining seven tributaries with

statistically significant slopes (high and low) all have a named riffle or rapid at the confluence.

Only two non-tributary sediment links have mainstem slopes which are not statistically significant, both of which are landslides. Four non-tributary sediment links have a significantly high slope and eight have a significantly low slope, as compared to the median slope (Table 2). Not all significant high slope, non-tributary sediment sources are necessarily a result of channel-modifying colluvium (see section 5.3).

4.5 (H5) Channel depth will decrease locally at all sediment links.

None of the depth measurements samples were statistically significantly different compared to the median depth. However, our more detailed exploration of this dataset later in this chapter in the Discussion section does suggest a relationship between changes in depth and sediment links in certain locations.

4.6 Hyperscale Analysis

Hyperscale graphs (Figure 7) offer new ways to analyze and interpret fluvial features at watershed to gravel bar extents (Fonstad & Marcus, 2010). Hyperscale graphs display the correlation between two variables using all possible window sizes to compute each correlation. Here, we use color to show the Pearson's correlation coefficient between two variables. Along the x-axis is distance downstream. The y-axis represents the size of the moving window used to compute the correlation coefficient (Dietrich, 2016b). Large window sizes should reveal general, basin-scale trends in how the two variables change through space relative to each other. At smaller window sizes the impact of local controls on the channel dominate the pattern. In the context downstream

hydraulic geometry we would expect width to have a generally positive correlation with discharge as the channel responds to increasing stream competence, and slope to have a generally negative correlation as relief decreases (Leopold & Maddock, 1953).

Figure 7 shows the correlation between channel width and estimated discharge at the channel forming flow. At window sizes above 120 km it exhibits the opposite trend as predicted by downstream hydraulic geometry, a general decrease in channel width with increasing discharge expressed as a negative correlation between the two. This is a function of the generally narrow channel as the Rogue River passes through the Klamath Mountains and Coast Range in the lower half of the study area. At window sizes between 30 km and 120 km changes valley geology appear. The upper portion of the watershed displays the trend in correlation we would expect from a confined reach and occurs where volcanic rocks confine the channel (Figure 2). At around RKM 60 the Rogue River enters the wider alluvial valley where width generally increases with increasing discharge. As the Rogue River flows out of the alluvial section channel width decreases downstream (RKM 100). As the Rogue River approaches the coast (RKM 180) the valley begins to widen moving downstream. Within these window sizes the relationship between channel width and discharge appears to be independent of tributary contributions, suggesting that geology is still the primary control.

At window sizes under 10 km (Figure 8) we would expect to see the influence sediment links and single-point geologic controls. Where channel form is a function of downstream hydraulic geometry we should also see some evidence at these spatial scales. Tributaries which join the Rogue River in the alluvial portion of the study area do tend to be associated with a positive correlation between channel width and discharge. These

include Evans Creek (RKM 77), the Applegate River (RKM 103) and Jump-off Joe Creek (RKM 122). Of these, only the Applegate River confluence was statistically wider than the study area. The bank erosion at RKM 50 also shows a positive correlation between width and discharge. Landslides should result in a negative correlation coefficient, driving a decrease in channel width regardless of discharge. Many of the landslides occur where there is a statistically insignificant correlation between width and discharge in the hyperscale graph indicated by a gap in the graph. Some, such as the landslides at RKM 82, 87 and 203 occur at places with a clear negative correlation coefficient between width and discharge indicating a localized narrowing of the channel. In general, the impact of this narrowing on the correlation does not extend beyond window sizes of 10 km.

The graph of slope and discharge (Figure 9) also exhibit a trend running opposite to that of downstream hydraulic geometry at window sizes greater than 130 km. At window sizes between 30 km and 130 km the middle, alluvial portion of the study area shows a slightly positive correlation between slope and discharge. This runs counter to downstream hydraulic geometry and the trends seen in the hyperscale graph of width and discharge. In the upper portion of the study area the mid-sized correlation coefficient window sizes show a patchwork of the expected negative correlation between slope and discharge. The impact of particularly low slope areas, such as at RKM 50, influence average slopes at these larger window sizes. In the downstream portion of the study area average slope decreases as the Rogue River leaves the Coast Range generating the expected negative correlation between slope and discharge.

At window sizes under 10 km (Figure 10) the influence of tributary and non-tributary sediment sources, and local geologic control (such as bedrock grade control) are apparent. This is most notable at locations where landslides interact with the channel such as at RKM 87, 121, 142, 148 and 203. Some, but not all of the tributaries exhibit an increase in slope while others have the opposite relationship with slope. Evans Creek (RKM 77), the Applegate River (RKM 103) and Galice Creek (RKM 134) all exhibit a positive correlation indicating a local increase in slope. Jump-off Joe Creek (RKM 122) and Mule Creek (RKM 181) exhibit a negative correlation; a local decrease in slope. At the scale of single pixels there is pattern of alternating positive and negative values. Carbonneau et al. (2012) suggest that this is potentially a function of the pool-riffle sequence. The black lines in Figure 10 show the location of named riffles and rapids in the study area. Some of these agree with the sequence of positive (high slope) and negative (low slope) correlations in the hyperscale graph but not all. In some locations such as between RKM 50 and 110 there is good overall agreement between where named riffles and rapids are and local increases in slope. In other areas, between RKM 150 and the end of the study area there appears to still be an agreement but the correlation does not have an influence at window sizes beyond a couple pixels.

5.0 DISCUSSION

The Rogue River presents a hydrogeomorphic landscape with high spatial variability which runs opposite the conceptual model for changes in geomorphic properties proposed by downstream hydraulic geometry (Leopold & Maddock, 1953), represents a more complex sediment landscape than the sediment links concept (Rice, 1998), and is less conducive to reach-specific characterization than channel-reach

morphology (Montgomery & Buffington, 1997). For the entire study, the downstream hydraulic geometry relation scaling exponent for width is below the expected range of 0.3-0.5 for alluvial channels (K. Gran & Montgomery, 2001). When dividing the study area into geologically similar reaches those that are characterized by alluvial processes do exhibit scaling exponents in-line with those expected by downstream hydraulic geometry. Specifically, the area upstream of Bear Creek, and that beginning just downstream of Grants Pass and ending at Jump-off Joe Creek. This suggests that the reason for the lack of characteristic downstream hydraulic geometry is those reaches which are geologically confined. These alluvial reaches are also where we see the clearest signals of sediment links in gravel sizes. The geologically confined sections where the expected patterns of downstream hydraulic geometry is not present also have more narrow channels, and higher slopes as expected.

In the Rogue River, sediment links appear to exert a quantitative control on many of the hydrogeomorphic variables we examined. However, variability within the channel is not entirely explained through sediment links. Rice (1998, 2016) and others (Ferguson, Cudden, Hoey, & Rice, 2006) suggest that tributary area relative to the main channel is a good predictor for the presence of a quantifiable sediment link based on the metric of an increase in gravel sizes. However, we find that gravel size does not act as a reliable indicator of a sustaining source of sediment, regardless of tributary watershed area.. In the Rogue River different sediment links seem to be highlighted by different hydrogeomorphic variables – width in some places, slope in others, and some do not appear to exert a quantifiable control on channel form. Our findings show that the identification of sediment links in the Rogue River must be considered in the context of

the multiple hydrogeomorphic variables which can be used to quantify channel form. No single variable was a consistent indicator of sediment link presence. Instead, different hydrogeomorphic variables exhibited a statistically meaningful change at predicted sediment sources inconsistently, suggesting that in the Rogue River enduring sediment sources do not create consistent geomorphic signals. We also show that the anthropogenic context for creating sediment links is important to understanding channel form. In the Rogue River some of the heterogeneity in channel form and gravel sizes can be explained in the context of downstream hydraulic geometry, sediment links, anthropogenic activity and geology, but much of it remains unexplained.

5.1 Digital Photosieving Calibration

We show that BASEGRAIN does an acceptable job computing gravel sizes, as compared to hand-sampled study done by the USGS in 2011, and produces a far more complete data set requiring less time in the field as compared to hand-counting. Our statistical analysis shows no difference between the D_{50} and D_{84} populations. However, the use of BASEGRAIN does present some challenges. Any given clast must be comprised of a certain number of pixels for the processing algorithm to positively identify it and compute its size. Additionally, there must be sufficient contrast between clasts and interstitial for accurate distinction between any two adjacent grains. Poor contrast could have the effect of over estimating gravel sizes as unique particles would be lumped together. For all but five gravel bars we were able to control both potential sources of error with proper study design. Overlapping clasts, such as imbrication, are not possible to control with proper study design. The result of overlapping clasts would be a systematic decrease in the size of any given gravel. We recognize that this has the

potential to create inaccurate data, but our comparison with the USGS study suggests that it was not an issue on the Rogue River. We suggest that accepting a marginal decrease in the level of precision in exchange for the clear increase in data resolution and spatial scale is desirable in those studies where environmental factors are appropriate for implementation of BASEGRAIN or other digital photosieving techniques.

5.2 Spatial Patterns of Gravel Bars.

Gravel bars in the Rogue River do not exhibit clustering in their spatial distribution throughout the watershed. However, both D_{50} and D_{84} sizes reveal some statistically significant size-based clustering of large gravel sizes at the gravel bars between RKM 187 and 198, an area with no identified sediment links. Within the context of sediment links, we would expect that at important sediment sources there would be a lack of size-based clustering as the sudden increase in gravel size would be much different than the gravels upstream. Then immediately downstream of a new link some size-based clustering would be evident as the gravel sizes between the adjacent bars would likely be similar, any size decrease being a function of the gradual in-channel fining processes. However, this expectation is not met. Patterns of downstream fining along the Rogue River are not present at the reach scale nor are they reliably present between the identified sediment links. In the Rogue River, gravel sizes appear to be more a function of local conditions such as sediment supply, geologic composition, and the local channel form as it relates to shear stresses and transport rates. The downstream patterns of gravel sizes in the Rogue River are not generally explained by continuous downstream fining, discontinuous sediment links, or some combination of these principles (Figure 5).

5.3 Sediment Links

In his original paper Rice (1998) describes tributaries as continuously depositing new material in the mainstem resulting in a persistent geomorphic signal of the sediment link. These systems must therefore be transport limited, there is more material of a large enough size that not all of it can be mobilized during channel forming flow events. Conversely, landslides are interpreted as discrete events with the geomorphic signal diminishing over time. In supply limited systems such as the Rogue River, a geomorphic signal due to deposition at tributary confluences is less likely to occur as a discharge in a tributary of sufficient magnitude to deposit material into the Rogue River is likely to occur when discharge in the Rogue River is sufficient to immediately transport the material downstream. This suggests that tributaries generate temporally transient, timebound sediment links. This is supported by our findings at most of the tributary confluences. The most notable geomorphic evidence of sediment links in the Rogue River were at landslide deposits where the size of hillslope material greatly exceeded the transport capacity of the Rogue River. While some finer material associated with landslides and debris flows is transported downstream, the largest clasts remains in-channel creating many of the geomorphic signals expected at a sediment link, most notably a local increase in slope. The hillslope sediment links therefore exist as enduring, timeless sediment links.

We enriched our analytical approach to identifying statistically high slopes through the inclusion of named riffle and rapids. This is an alternative method for independently identifying the presence of high slopes which can help identify which sediment sources may be triggering an increase in slope; either through high magnitude,

low frequency events or continuous source of sediment. This is important given the inconsistent relationship between the statistical variables in our study and challenges associated with relying purely on statistical analysis (Ziliak & McCloskey, 2008). One would expect that the tributary sediment sources which have a named feature and a local increase in slope value larger than the median are likely initiation points for sediment links. The Applegate River, Evans Creek and Galice Creek are good examples of this, with named hydrologic features associated with a statistically meaningful increase in channel slope. Despite the channel-form evidence for active sediment links, the gravel sizes at the Applegate River confluence are smaller than the reach average and represent a decrease in gravel size compared to gravel bars upstream and downstream. We propose that we don't see a sediment size spike at Bear Creek, Jump-off Joe Creek and Grave Creek, is that sediment storage is occurring upstream of the confluence with the Rogue River and/or the downstream transport of deposited material by the Rogue River thus removing geomorphic evidence of the sediment link. Aerial imagery from NAIP show, and geologic maps classify extensive portions of the tributary channel as alluvial and unvegetated. We hypothesize that these gravels are not entering the Rogue River due to deposition prior to their confluence, with infrequent mobilization to the Rogue River occurring at flows sufficiently large that deposition does not occur in the main Rogue River. It is also possible that abrasion prior to entering the Rogue River results in gravels which are of a similar enough size that there is no discernable signal. Tributary sediment links therefore being timebound as discussed privously.

All the non-tributary sediment sources except four have a named riffle or rapid adjacent to where they intersect the active channel, which is confirmed with the statistical

analysis of slope. However, when considering non-tributary sediment sources, we noticed that in-channel morphology does not always align with the sediment links hypothesis. The landslide at RKM 58.32 has a named hydrologic feature, a statistically steeper slope, and higher unit stream power. However, at this location the cause of the rapid is bedrock, not colluvium from field observations. Similarly, the landslide at RKM 148.63, from field observations, is a combination of bedrock and hillslope deposits. This study cannot positively attribute a given gravel bar's presence to the adjacent hillslope. Some landslides, such as the one at RKM 148.63 and RKM 142.16 have large angular midstream boulders with no evidence of alluvial transportation supporting the observation of a hillslope process derived sediment link. Other bars adjacent to landslides do not.

Slope and the presence or absence of riffles and rapids should be linked, as riffles and rapids are defined, in part, by a local increase in slope. All of the sediment links which have a named riffle have a significantly steep slope except for Little Butte Creek and the landslide at RKM 82.17, neither of which have a significant slope result. However, not all sediment links reveal a significantly high slope value as expected. The inconsistency between on-the-water identified hydrologic features and the statistical slope analysis is potentially related to how the USGS generates its 10-meter elevation data and therefore how slopes were computed. Elevation data for the study area is based on the 1/3 arc-second DEM from the USGS. Vertical accuracy is based on the best available source data which, for the study area, is usually LiDAR based. For a small portion of the study area beginning just downstream of Mule Creek and extending to the end of the field study area LiDAR data is unavailable and the elevation data was likely

derived by the USGS using the 1:24,000 contour lines (Archuleta, Constance, Lowe, Mantey, & Phillips, 2017). The rapids at sediment links which either do not have a significant slope value compared to the median, or have a significantly low value all have low relief through the riffle and tend to be less than 40 meters long. Thus, the slope computation used in this study smooths the riffle to a low slope value which is not statistically different than the median, despite the fact that they are observable, named features.

5.4 Relative Depth

The samples for the depth analysis were conducted in the same manner as the other hydrogeomorphic variables. With depth, these included the range of depths before, at and after a sediment link. The analytical approach was such that this range of values was tested for its statistical relationship with all observations, but within-sample variation was not analyzed. How depth changes at a sediment link should reveal the presence of a pool-tail crest, suggesting a submerged delta deposit that may not be revealed based on channel slope or unit stream power. At Mule Creek there is a rapid decrease in depth at the confluence, indicative of a pool-tail crest (Heitke, Archer, & Roper, 2010). The Mule Creek signal is important because it doesn't show up as a significant sediment source in any of the other hydrogeomorphic variables. At the Mule Creek confluence depth decreases by five meters compared to the pool upstream of the confluence. The clear alluvial fan at the Rogue River's edge suggests that the change in depth is an indication of a submerged delta and a potentially important sediment link in the formation of the downstream gravel bar which has a D_{50} of 55.3mm and a D_{84} of 104.4, both of which are

larger than the nearest upstream bar. This indicates that there are some sediment link effects that are not discernable from our methods.

5.5 Historic Anthropogenic Context

The Galice Creek confluence has statistically significant high unit stream power and high slope in the mainstem despite the small watershed area, which runs counter to the predictive model proposed by the sediment links concept. Hydraulic mining started at the Old Channel Mine on Galice Creek in 1860 with written accounts claiming massive amounts of material being washed down daily (“Galice Creek - Oregon Gold Locations,” n.d.). Hydraulic mining likely delivered an abundance of material oversized for the tributary, to the Rogue River. The notable rapid, high slope, and high unit stream power here are likely the legacy of the volume and size of material washed into the Rogue River during mining operations. Our analysis suggests that Galice Creek is a potentially important sediment link, however the history of land-use in the area calls the geomorphic evidence in to question. The only section with an apparent trend in downstream fining begins at Galice Creek (RKM 134.9) with gravel sizes fining consistently to Galice Creek before increasing at the two landslides downstream of Grave Creek (RKM 148.62 and 153.64). Given the historical context of Galice Creek, we believe the downstream fining could be a function of the delivery of especially large material to the Rogue River as a byproduct of hydraulic mining. Galice Creek and the Flanagan Mine debris at RKM 113.63 have two of the largest D_{50} and D_{84} values of the sediment links with an adjacent gravel bar. Galice Creek has an important history of hydraulic mining which is likely a key source of the size of material at its confluence with the Rogue River, and the associated rapid. Likewise, the material from the Flanagan Mine are also comprised of

larger material than would be frequently transported and appear to result in an in-channel increase in gravel size.

Based on the watershed area and geology of the Applegate River, we would expect it to produce a clear sediment link with an increase in gravel sizes and likely a riffle or rapid at its confluence with the Rogue River due to the local increase in slope from the contribution of new alluvium. The statistically high-slope and named riffle at the Applegate River ends just upstream of the modern confluence. Examining aerial imagery from 1939 (georectified using NAIP imagery) we see that the Applegate River used to meet the Rogue River just upstream of the riffle in question (Figure 6). Since the 1939 imagery anthropogenic modification forced the Applegate River mouth downstream to its current location. This suggests that historically the Applegate River contributed enough material to form an alluvial deposit sufficient to create a riffle and sediment link.

Unfortunately, we do not have a good time constraint on when the occurred. Unlike at Galice Creek which has a sediment link signal because of human activity, the Applegate River may be missing the statistical high-slope signal because of human activity moving the channel. We cannot know what the gravel sizes at the historic confluence of the Applegate river were, but at the bar upstream of the modern confluence, adjacent to the historic confluence D_{50} size is the same, but the D_{84} is slightly larger than the D_{84} at the modern confluence (table 1).

The exaggerated signal at Gravel Creek, buried alluvial deposit at Mule Creek and spatially disjointed signal at the Applegate River all suggest that observing physical evidence of sediment links can be problematic. Channel modification and the overlying hydrologic conditions can enhance or hide a signal. The majority of the sediment links in

this study could not be consistently identified across all hydrogeomorphic variables measured. This challenge in signal identification is likely closely related to the challenges arising from readily available hyperscale data sets. As heterogeneity in a channel appears to increase with data resolution, what we think of as a geomorphic signal becomes harder to distinguish from natural variability, or noise. Frequently, observations of fluvial systems identify a variety of processes interacting at multiple spatial scales including sediment links, sediment breaks, evidence of legacy events and an overall patchwork of channel-forming process links (Carbonneau et al., 2012).

5.6 Additional Geomorphic Controls

The Applegate River and Grave Creek are the only large tributaries which have a gravel bar at the confluence and D_{84} and D_{50} values which are smaller than the reach average. Given the findings of Rice (1998) and the relative watershed sizes of these tributaries we would expect both tributaries to trigger an increase in gravel sizes. The sub-basin geology of these tributaries is comprised predominately of softer, mixed sedimentary rock. Additionally, they both flow through their own depositional valley before entering the Rogue River. Jump-off Joe Creek is also large enough that we would expect an increase in gravel size associated with the sediment link, but closest downstream gravel bar is roughly a kilometer away and the gravel sizes there are smaller than the study-area average. Both suggest that the depositional environment before the confluence, and softer geology in the tributary watershed more prone to fining result in a sediment link which is not expressed in gravel size. However, given the similarity between tributary lithologies and mainstem lithology we do not believe that tributary sub-basin geology is playing a major role in channel morphology.

The previous discussion has examined the role of tributary and non-tributary sediment links as external controls on channel morphology. However, autogenic processes also play a role in channel form. We see potential evidence of self-organized pool-riffle sequences in alluvial reaches. Sediment waves, or pulses, are also likely playing a role in channel form. While not explicitly tested in this study, these processes likely have some explanatory role in the portion of channel heterogeneity not previously explained. Depth, particularly in the alluvial sub-reach downstream of the confluence with the Applegate River, appears to exhibit a semi-regular trend between relatively deep and shallow reaches with a spacing of 400 to 1000 meters, roughly five to seven times the mean channel width (Knighton, 1998; Leopold et al., 1992). The hyperscale graph of slope (Figure 8) shows a similar pattern for slope. At the smallest window sizes alternating positive and negative correlation values, indicate alternating high and low slope, have a similar spatial frequency as depth. Like depth, the section of the Rogue River where this trend is clearest is in the alluvial portion downstream of the Applegate River.

In course alluvial rivers sediment tends to disperse downstream rather than translate downstream maintaining a wave-form (Sklar et al., 2009; Venditti et al., 2010). The deposition attributed to a sediment link, would increase bed elevation locally with the same effect on channel form as discussed at the end of section 1. Between the spatially episodic hillslope and continuous tributary sediment delivery, processes of dispersion and translation of the sediment will diminish the initial signal – potentially rendering the wave (sediment link) undetectable. In-channel storage where channel width increases or slope decreases, and the potential of (de)synchronization at tributaries could

also complicate the sediment links concept (K. B. Gran & Czuba, 2017). This study showed that at many of the confluences channel width was high and slope was low, relative to the study area, suggesting that local storage of sediment may be occurring. In-channel storage may also account for the subtle clustering of larger gravel sizes between RKM 187 and 198. In addition to the dispersion and storage of sediment the combined effects of multiple sediment contributions may also serve to enhance or depress the sediment link signal.

5.7 Hyperscale Graphs

The hyperscale graphs reveal the importance of the varying spatial extent of a given sediment link relative to larger spatial scale geologic controls. The hyperscale graphs displaying the full range of correlation windows (Figures 7 and 9) illustrate the relationship between larger-scale controls and their respective variables. Changes in the longitudinal relationship between any two variables appears to be related to the broad scale geologic controls, a similar finding and interpretation to that by Dietrich (2016). These broad-scale trends provide useful insight into the spatial scales at which trends such as downstream hydraulic geometry persist.

At smaller scales of correlation (Figures 8 and 10) the impact of local controls on channel form are more apparent. In figure 10 we would expect the presence of a pool-riffle channel-form to be most apparent. In some reaches such as between RKM 100 and RKM 160 there does appear to be a strong co-occurrence of named riffles and rapids (black lines) and local increases in slope (positive correlations). The distance over which the local increase in slope influences broader trends can be estimated by the vertical extent (y-axis) of the signal. The majority of the riffles and rapids with a positive

correlation only exert a signal which is quantifiable at the smallest window sizes. We believe that these are likely true indicators of the pool-riffle sequence in sections where alluvial processes dominate. High slope areas, such as at RKM 150, which have a signal persisting beyond the 10km window more frequently a function of bed-rock control. This interpretation of the pool-riffle sequence is similar to that by Carbonneau et al. (2012). At correlation windows below 10km the relationship between width and discharge appears dominated by large, seemingly isolated changes in width. In some areas such as between RKM 65 to 80 width does not vary downstream (Figure 5) so a relatively abrupt, small increase or decrease in width (RKM 68 and 72, respectively) would have a disproportionate impact on the hyperscale graph.

6.0 CONCLUSION

This study finds that the impact of tributary and non-tributary sediment sources on channel morphology was highly varied, depending on sediment source type and hydrogeomorphic variable being examined. The lack of consistent correlation between any given variable and a change in channel morphology suggests that for the Rogue River, a predictive model of sediment links as *primary* controls of channel morphology is in not appropriate, although some sediment links are evident. In the low-disturbance field sites used by Rice (1998), gravel size plays a key role in the identification of channel forming sediment links. Local controls on the Rogue River and its tributaries, in concert with the history of mining and land use, generate a scenario where sediment links may be expressed through some, but not necessarily all, of the hydrogeomorphic variables used here. Despite gravel size and tributary drainage area not being consistent indicators of sediment links, as suggested by Rice (1998), we do find several interesting signals such

as the role that historic anthropogenic activity appears to have in producing sediment links and submerged alluvial fan-like features as evidence of otherwise unapparent sediment links.

As our ability to measure rivers over larger distances and at higher resolutions improves, this spatially extensive and intensive data can be used to deepen our understanding of channel morphology across spatial scales. The hyperscale approach taken here allows for the simultaneous study of basin-scale patterns and local processes. The relationship between localized, autogenic process on channel form can be observed in the context of basin-wide trends in channel morphology. This offers the potential to deepen our understanding of how a single sediment wave (sediment link) may behave and inform pool-riffle sequences, and what that means for larger spatial-scale patterns such as downstream fining between sediment links.

Table 3. Gravel bar name, location and respective size thresholds. The D₅₀ sizes are generally course gravels while D₈₄ falls into the cobble classification. Normalized size classes are the observation at a given gravel bar divided by the average of all observations for that size threshold.

Gravel Bar Name	Location (RKM)	D ₅₀ (mm)	D ₈₄ (mm)	Normalized D ₅₀	Normalized D ₈₄
MidValley_GB02	46.36	62.40	112.10	1.08	1.13
MidValley_GB03	47.73	62.59	113.28	1.09	1.15
MidValley_GB04	49.07	59.07	96.31	1.02	0.97
MidValley_GB05	49.73	56.21	93.54	0.97	0.95
MidValley_GB06	50.49	59.06	101.64	1.02	1.03
MidValley_GB07	51.55	59.53	99.47	1.03	1.01
MidValley_GB08	65.31	55.85	98.28	0.97	0.99
MidValley_GB01	65.31	56.45	99.88	0.98	1.01
MidValley_GB09	74.15	62.62	108.00	1.09	1.09
MidValley_GB11	77.23	60.02	106.19	1.04	1.07
MidValley_GB12	77.41	66.06	116.89	1.15	1.18
MidValley_GB13	79.04	58.69	99.26	1.02	1.00
MidValley_GB14	82.80	55.01	93.30	0.95	0.94
MidValley_GB15	83.81	53.00	91.86	0.92	0.93
MidValley_GB16	85.76	57.32	95.91	0.99	0.97
MidValley_GB17	85.96	58.69	99.59	1.02	1.01
MidValley_GB18	86.38	57.41	97.56	1.00	0.99
MidValley_GB19	91.73	58.91	97.82	1.02	0.99
MidValley_GB21	95.11	64.33	118.74	1.12	1.20
MidValley_GB22	96.49	60.02	105.00	1.04	1.06
MidValley_GB23	101.83	53.63	93.72	0.93	0.95
MidValley_GB24	103.41	54.62	89.18	0.95	0.90
MidValley_GB25	103.78	52.19	66.24	0.90	0.67
RecSec_GB01	108.96	52.41	89.45	0.91	0.90
RecSec_GB02	111.14	56.56	98.98	0.98	1.00
RecSec_GB04	113.96	62.37	111.99	1.08	1.13
RecSec_GB05	115.91	59.07	104.25	1.02	1.05
RecSec_GB06	116.50	53.94	93.63	0.94	0.95
RecSec_GB08	117.73	52.19	71.24	0.90	0.72
RecSec_GB09	118.95	52.19	71.24	0.90	0.72
RecSec_GB11	124.11	55.30	97.52	0.96	0.99
RecSec_GB12	128.41	53.91	103.68	0.93	1.05
RecSec_GB13	128.50	57.64	99.54	1.00	1.01
RecSec_GB15	130.25	51.05	72.52	0.89	0.73
RecSec_GB16	131.29	52.68	82.97	0.91	0.84
RecSec_GB17	134.60	60.02	120.50	1.04	1.22
RecSec_GB18	135.09	53.91	109.80	0.93	1.11
RecSec_GB19	138.48	54.04	97.48	0.94	0.99
RecSec_GB20	139.73	58.69	110.18	1.02	1.11
W_SR_GB01	142.30	53.30	89.54	0.92	0.91
W_SR_GB02	145.89	53.24	72.58	0.92	0.73
W_SR_GB03	148.01	52.19	71.26	0.90	0.72
W_SR_GB04	149.68	57.32	93.68	0.99	0.95
W_SR_GB05	153.11	54.83	91.65	0.95	0.93
W_SR_GB06	164.91	67.31	133.73	1.17	1.35
W_SR_GB07	166.64	0.00	0.00	0.00	0.00
W_SR_GB09	174.10	56.45	105.41	0.98	1.07
W_SR_GB11	177.39	52.19	64.70	0.90	0.65
W_SR_GB12	181.75	55.29	104.42	0.96	1.06
W_SR_GB13	187.30	54.16	96.03	0.94	0.97
W_SR_GB18	193.03	85.70	151.35	1.49	1.53
W_SR_GB19	193.88	65.54	121.61	1.14	1.23
W_SR_GB20	194.28	61.85	116.26	1.07	1.18
W_SR_GB21	195.98	55.60	95.75	0.96	0.97
W_SR_GB22	197.91	59.91	103.61	1.04	1.05
W_SR_GB24	204.49	57.32	96.58	0.99	0.98

Table 4. Statistical output table for all of the tributaries and landslides for all hydrogeomorphic variables. We take a p-value < 0.05 to indicate a statistically significant result as compared to the study area median value.

RKM	Name	Tributaries - Width				Tributaries - Unit Stream Power				Tributaries - Slope				Tributaries - Relative Depth Model			
30.17	Reece Creek	f-test	42.46	p-value	0.00	f-test	34.89	p-value	0.00	f-test	10.34	p-value	0.00				
40.84	Little Butte Creek	f-test	32.11	p-value	0.00	f-test	21.62	p-value	0.00	f-test	6.489	p-value	0.01				
46.91	Snider Creek	f-test	63.73	p-value	0.00	f-test	30.92	p-value	0.00	f-test	3.387	p-value	0.06	f-test	-3210112	p-value	1.00
49.83	Bear Creek	f-test	13.18	p-value	0.00	f-test	34.30	p-value	0.00	f-test	31.93	p-value	0.00	f-test	-3204587	p-value	1.00
77.23	Evans Creek	f-test	2.056	p-value	0.15	f-test	35.15	p-value	0.00	f-test	41.37	p-value	0.00	f-test	-3215240	p-value	1.00
103.78	Applegate River	f-test	187.36	p-value	0.00	f-test	12.25	p-value	0.00	f-test	74.62	p-value	0.00	f-test	-3227247	p-value	1.00
122.84	Jump-off Joe Creek	f-test	3.70	p-value	0.05	f-test	2.256	p-value	0.13	f-test	0.198	p-value	0.65				
134.91	Galice Creek	f-test	0.27	p-value	0.60	f-test	15.08	p-value	0.00	f-test	15.11	p-value	0.00	f-test	-3205673	p-value	1.00
148.07	Grave Creek	f-test	30.84	p-value	0.00	f-test	71.83	p-value	0.00	f-test	83.75	p-value	0.00	f-test	-3211041	p-value	1.00
181.46	Mule Creek	f-test	21.26	p-value	0.00	f-test	11.38	p-value	0.00	f-test	1.406	p-value	0.23	f-test	-3203885	p-value	1.00
216.81	Illinois River	f-test	48.57	p-value	0.00	f-test	39.08	p-value	0.00	f-test	95.99	p-value	0.00				
RKM		Other Sed Sources - Width				Other Sed Sources - Unit Stream Power				Other Sed Sources - Slope				Tributaries - Relative Depth Model			
50.27	Bank Erosion	f-test	133.03	p-value	0.00	f-test	42.76	p-value	0.00	f-test	54.99	p-value	0.00	f-test	-3248931	p-value	1.00
52.74	LS1	f-test	3.19	p-value	0.07	f-test	21.64	p-value	0.00	f-test	89.68	p-value	0.00	f-test	-3218668	p-value	1.00
58.32	LS1B	f-test	0.72	p-value	0.39	f-test	34.77	p-value	0.00	f-test	264.91	p-value	0.00	f-test	-3317631	p-value	1.00
71.20	LS2	f-test	54.22	p-value	0.00	f-test	69.44	p-value	0.00	f-test	105.41	p-value	0.00	f-test	-3224778	p-value	1.00
82.17	LS3	f-test	15.45	p-value	0.00	f-test	12.52	p-value	0.00	f-test	3.74	p-value	0.06	f-test	-3237431	p-value	1.00
87.86	LS4	f-test	0.092	p-value	0.76	f-test	3.066	p-value	0.07	f-test	2.30	p-value	0.12				1.00
113.63	Mine Tailings	f-test	118.43	p-value	0.00	f-test	264.06	p-value	0.00	f-test	239.38	p-value	0.00				1.00
121.93	LS5	f-test	0.79	p-value	0.37	f-test	2.82	p-value	0.09	f-test	50.90	p-value	0.00	f-test	-3230671	p-value	1.00
142.16	LS6	f-test	3.13	p-value	0.07	f-test	33.84	p-value	0.00	f-test	31.86	p-value	0.00	f-test	-3211833	p-value	1.00
148.62	LS7	f-test	53.99	p-value	0.00	f-test	59.65	p-value	0.00	f-test	59.83	p-value	0.00	f-test	-3205991	p-value	1.00
153.64	LS8	f-test	52.52	p-value	0.00	f-test	7.20	p-value	0.01	f-test	34.95	p-value	0.00	f-test	-3219850	p-value	
203.75	LS9	f-test	96.68	p-value	0.00	f-test	0.14	p-value	0.70	f-test	44.33	p-value	0.00	f-test	-3283365	p-value	
209.58	LS10	f-test	101.79	p-value	0.00	f-test	8.29	p-value	0.00	f-test	172.33	p-value	0.00				
218.44	LS11	f-test	211.60	p-value	0.00	f-test	1.83	p-value	0.17	f-test	117.77	p-value	0.00				

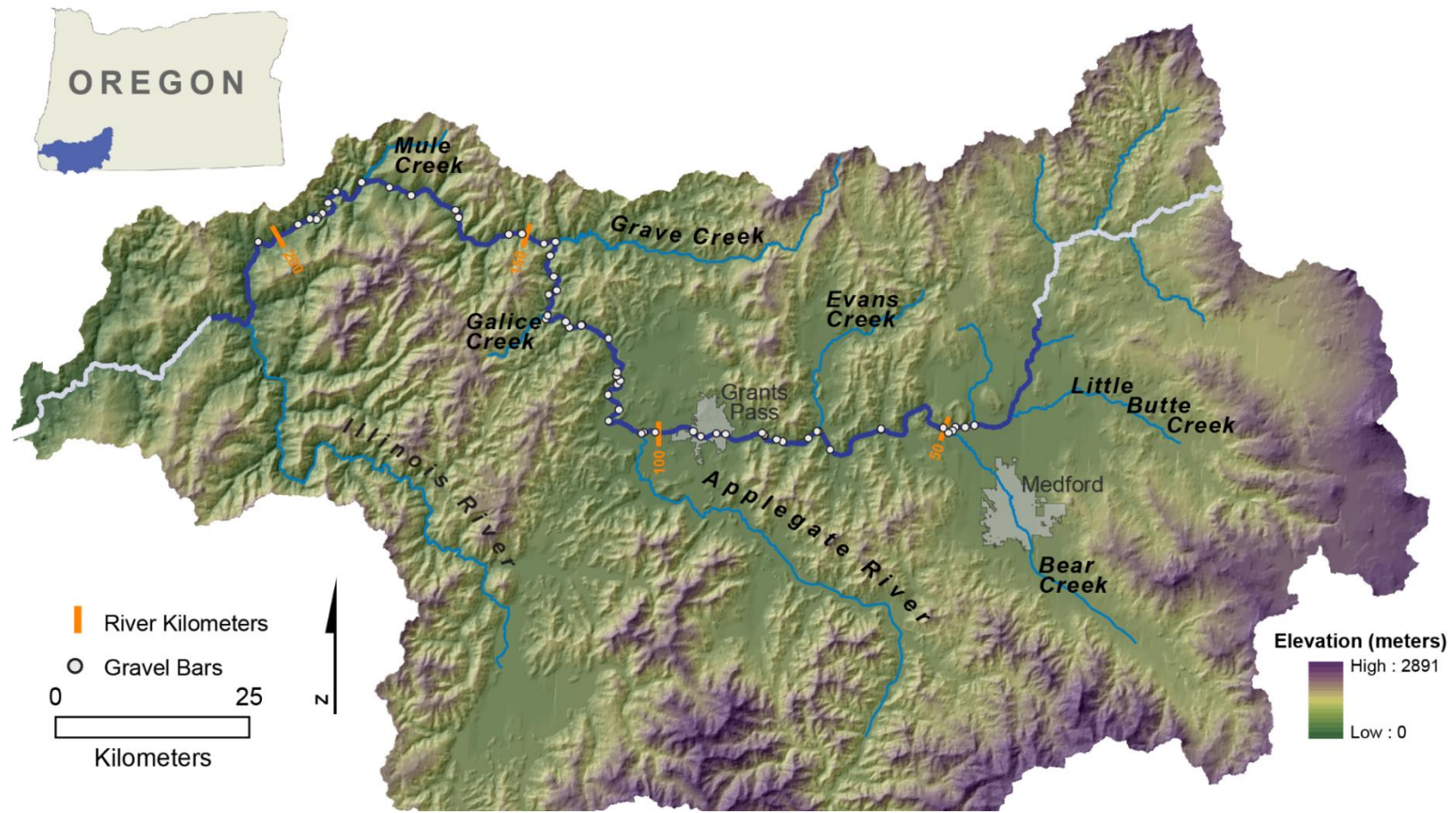


Figure 7. Rogue River watershed location in Oregon (upper left) and a detailed map of the study area. Gravel bar sample locations, tributaries and Grants Pass are also labeled. The GIS portion of the analysis is comprised of the darker blue streamline. Field work is approximated by the location of gravel bar samples.

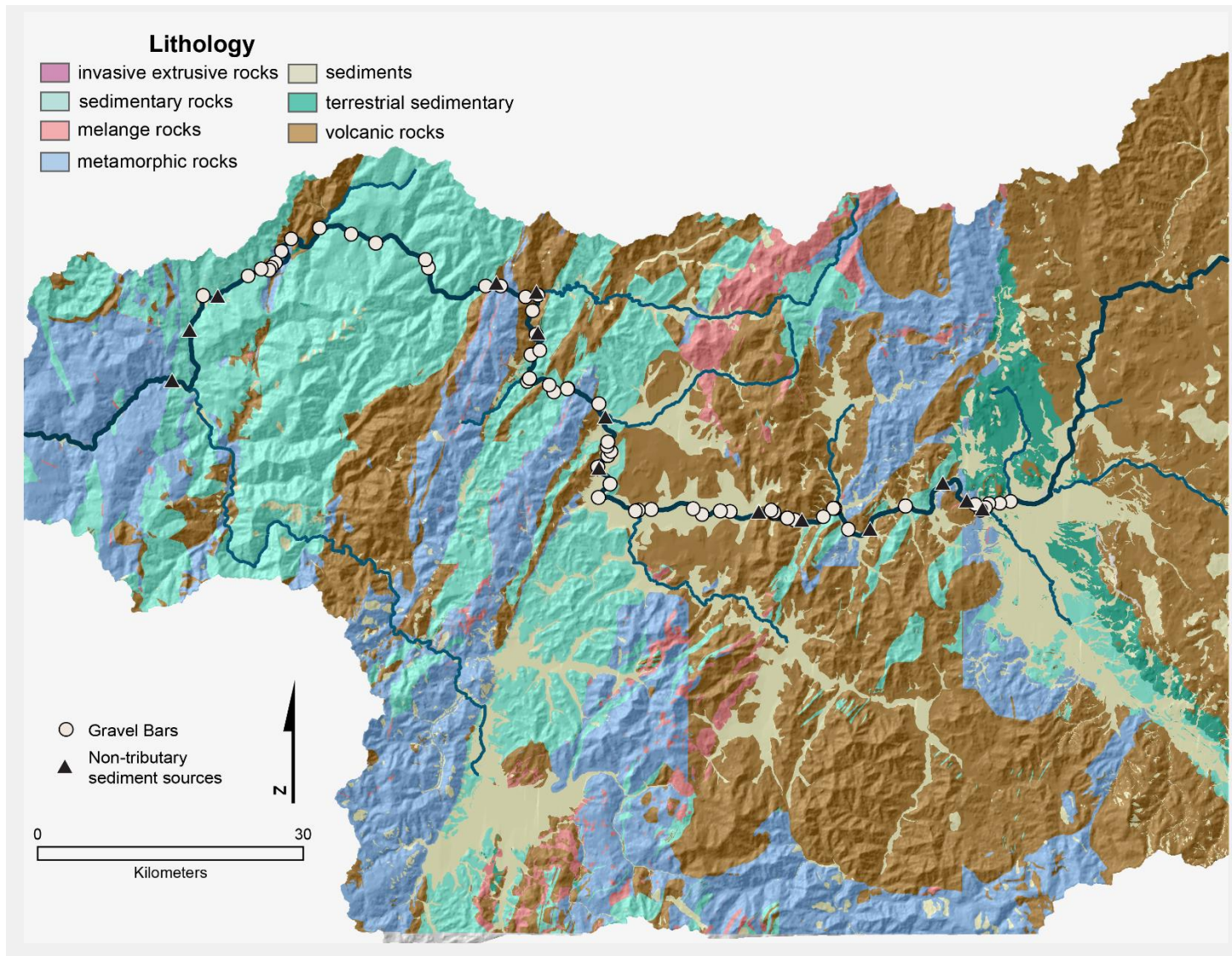


Figure 8. General geologic units of the Rogue River study area and the locations of gravel bars (circles), tributaries and non-tributary sediment sources (triangles) (Archuleta, Constance, Lowe, et al., 2017).

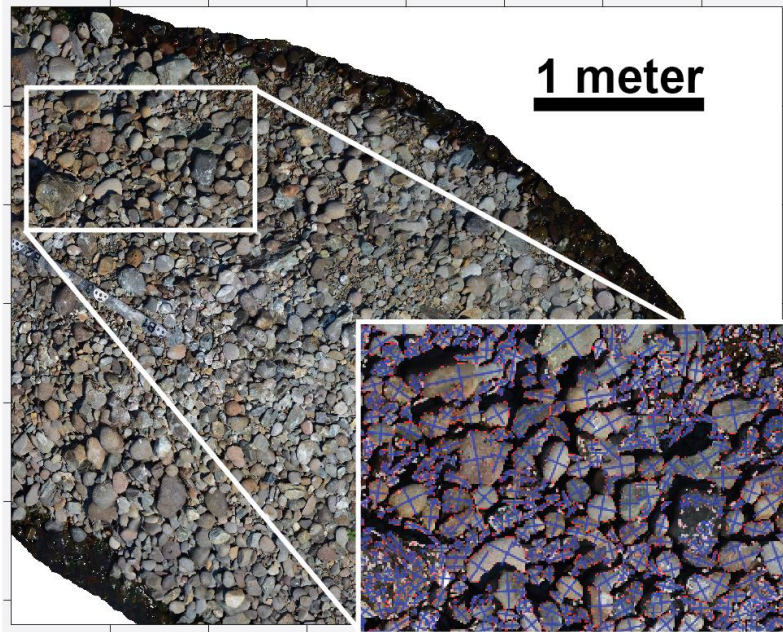


Figure 9. Comparison images of a portion of gravel bar 'MidValley_14'. On the left is the partitioned image from BaseGrain. Blue lines show the location of the a and b axes used in the computation. The right image shows the original photograph of the same area.

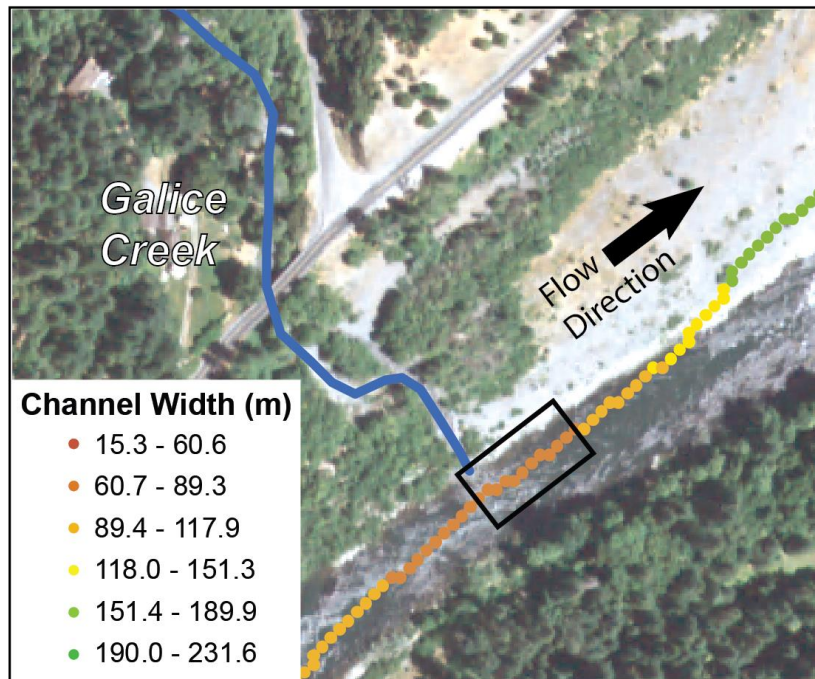


Figure 10. An example of the sampling method for the statistical analysis looking at the confluence of Galice Creek and the Rogue River. The black rectangle shows the extent of an 80-meter sample, here sampling active-channel widths. The selection of width values here will be compared to all width values.

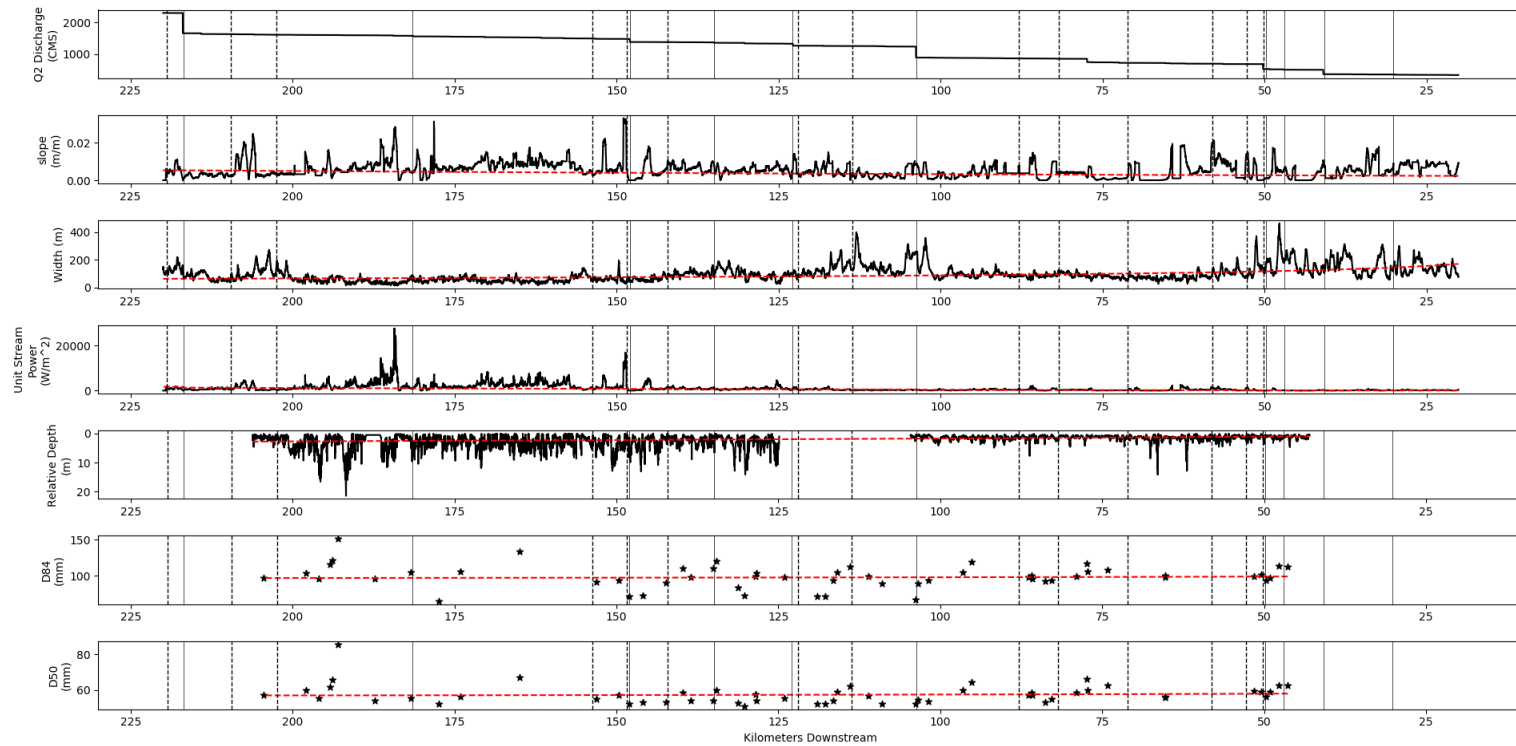


Figure 11. The hydrogeomorphic variables discharge, slope, width, unit stream power, depth, D_{84} and D_{50} for the Rogue River. Flow direction is from right to left. The red dashed lines show the downstream hydraulic geometry best-fit equations. Width, depth and each gravel size are computed using a power function. Slope is computed as an exponential function. Unit stream power is computed using the downstream hydraulic geometry equation prediction from the other variables. Vertical lines show the location of potential sediment links. Solid lines are tributary locations and dashed lines show non-tributary sediment sources.

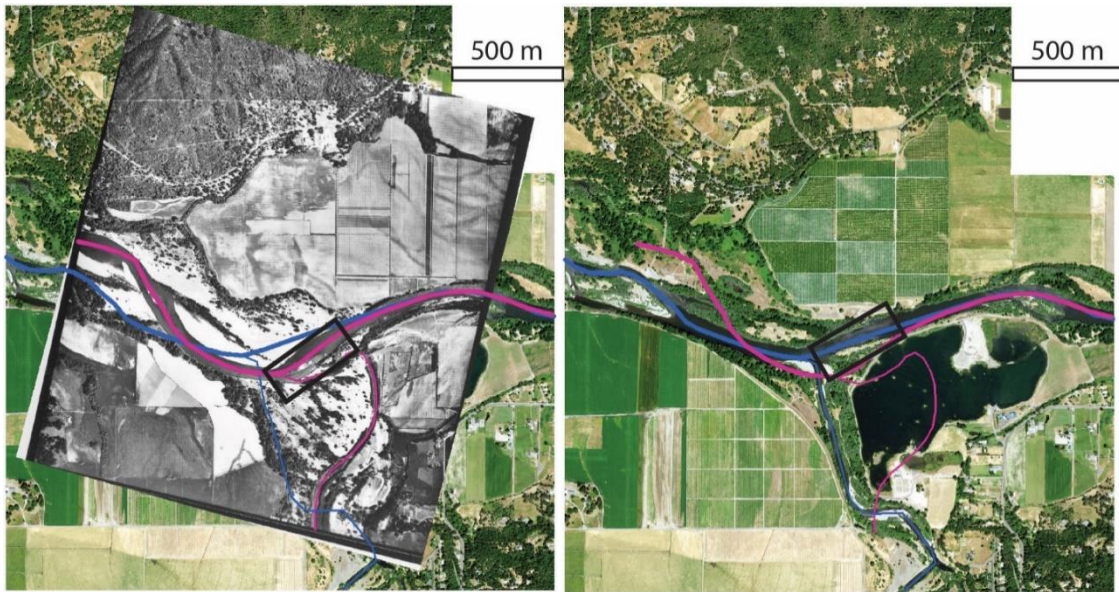


Figure 12. Historical imagery from 1939 (left) and current NAIP imagery (right) showing the shift in the confluence of the Applegate River (entering from the south) and the Rogue River (flowing right to left). The riffle associated with the confluence of the two rivers is outlined in black.

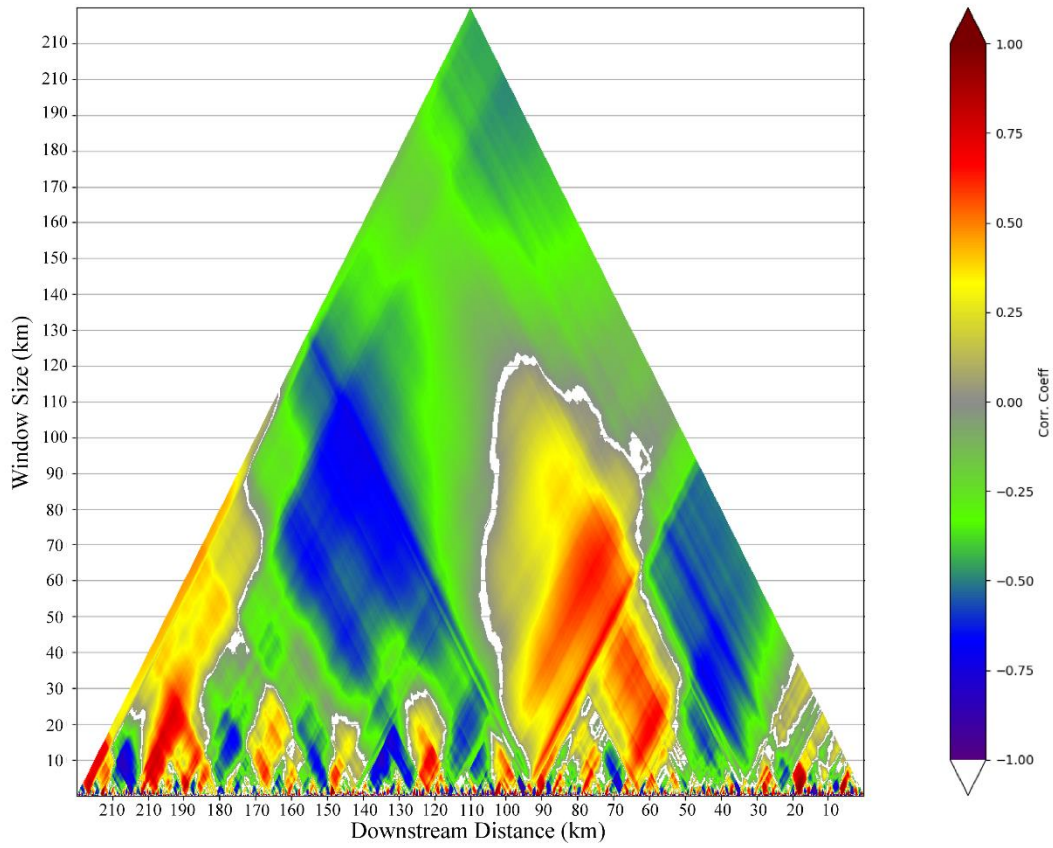


Figure 13. Hyperscale correlation coefficients for width and the computed Q_2 discharge. Gaps in the data occur where the correlation is not statistically significant ($p=0.01$).

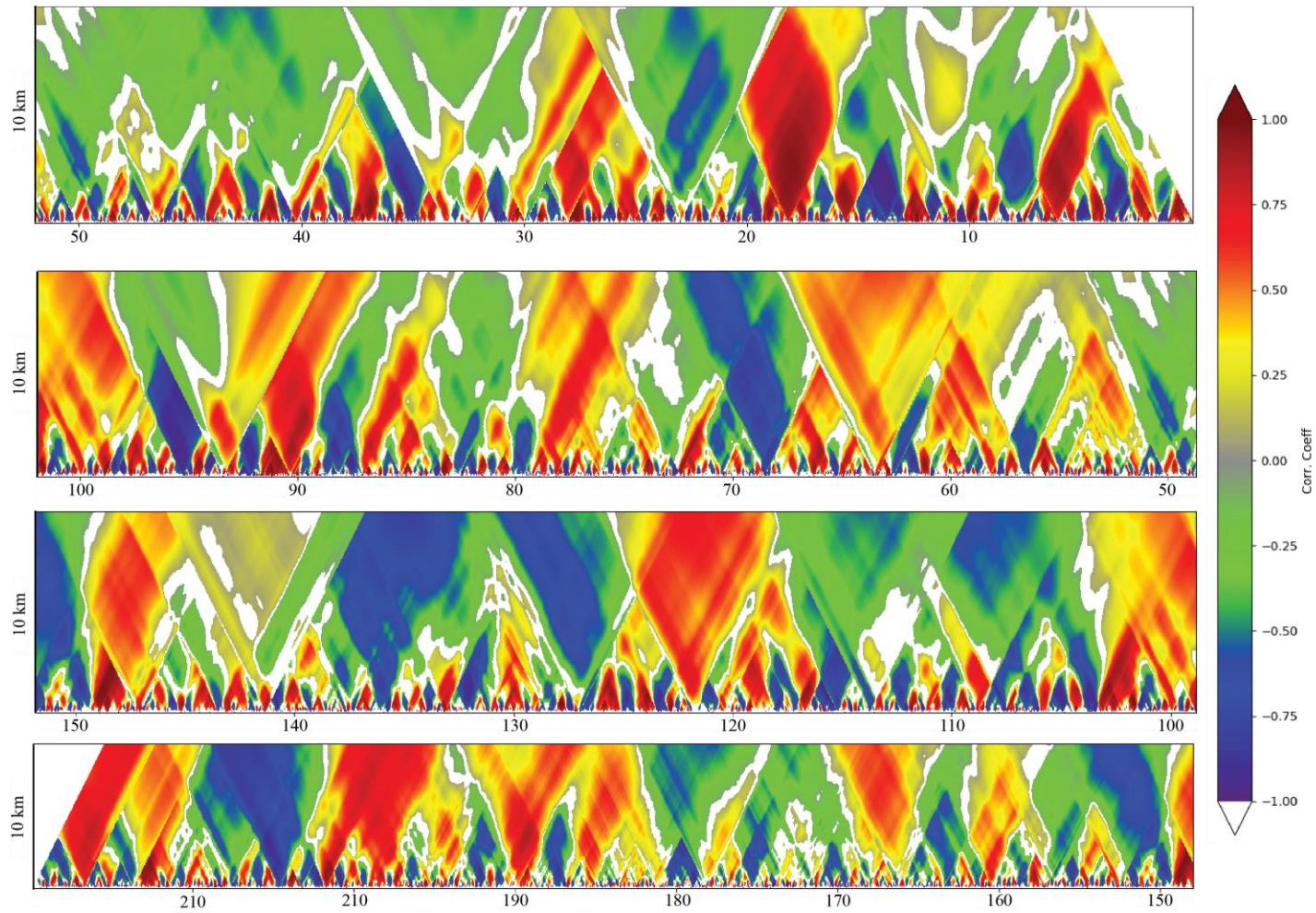


Figure 14. A close-up view of the 10 km and below window size examining the correlation between width and discharge. The study area begins in the upper right, and flows right to left through each row. The black diagonal lines show the location of named riffles and rapids.

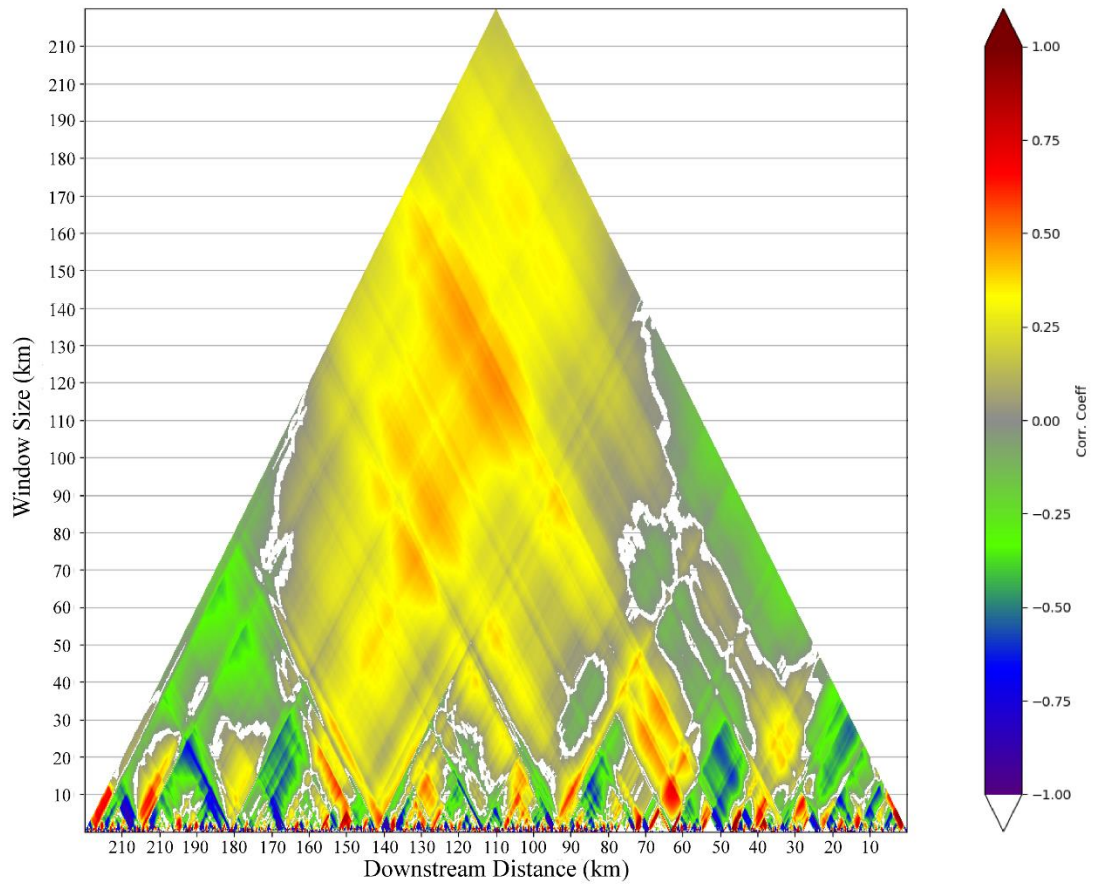


Figure 15. Hyperscale correlation coefficients for slope and the computed Q_2 discharge. Gaps in the data occur where the correlation is not statistically significant ($p=0.01$).

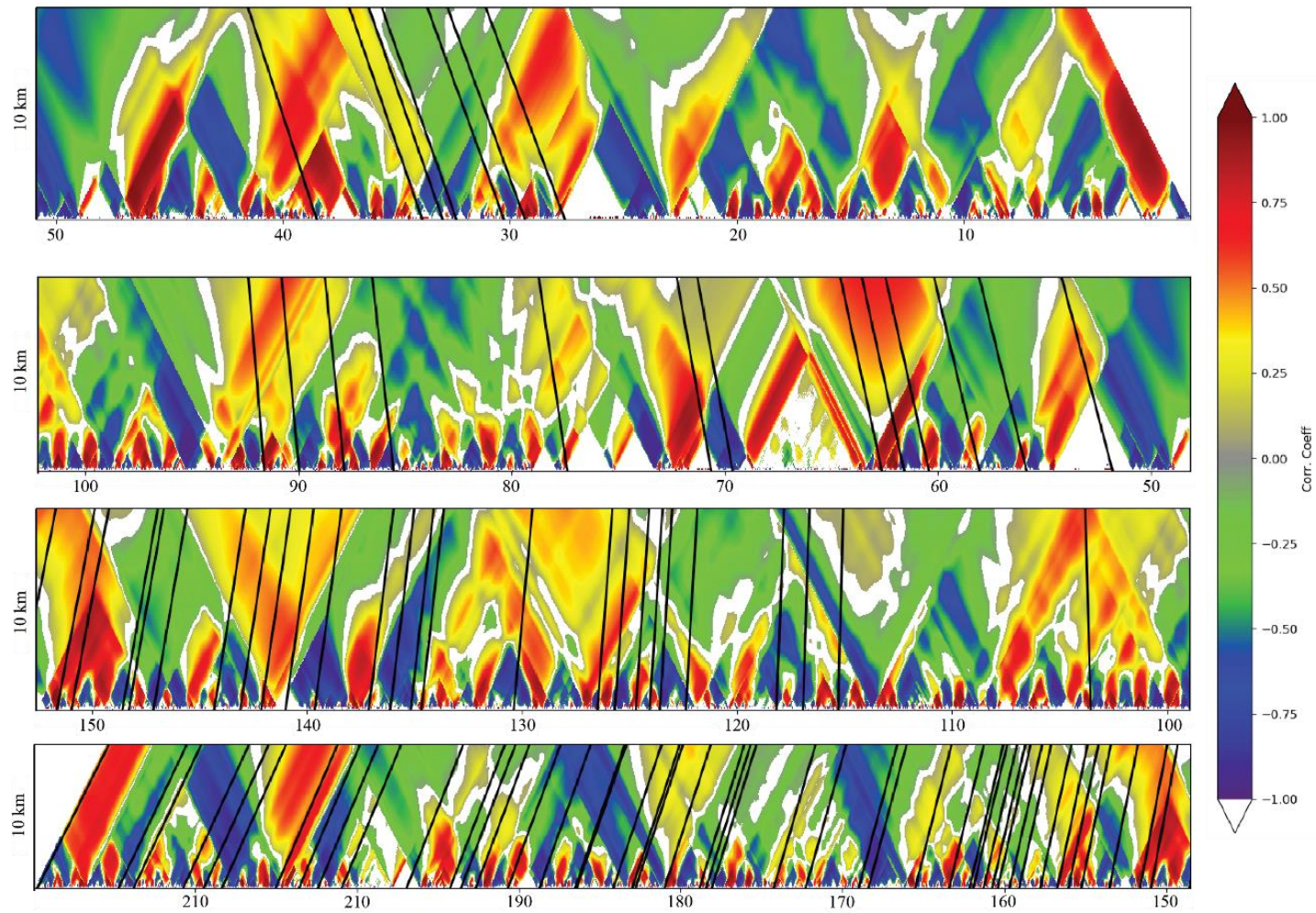


Figure 16. A close-up view of the 10 km and below window size examining the correlation between slope and discharge. The study area begins in the upper right, and flows right to left through each row. The black diagonal lines show the location of named riffles and rapids.

BRIDGE: CHAPTER 3: A RIVERSCAPE MAPPING APPROACH TO THE
SEDIMENT LINKS CONCEPT AND CHAPTER 4: VIDEO STRUCTURE-FROM-
MOTION: DEVELOPING A METHOD FOR CONTINUOUS MAPPING OF WATER
SURFACE ROUGHNESS

Chapters 2 and 3 take a hyperscale approach to data collection, measuring a variety of hydrogeomorphic variables at scales from a centimeter to meters over 200 kilometers of the Rogue River. Conversely, our ability to map hydraulic processes (waves, riffles, eddy separation zones) are only effect at channel unit scales, 10s of meters or larger. This represents a fundamental mis-match in data resolution between channel form, measured at centimeters and channel hydraulics, measured at 10s of meters. Chapter 4 seeks to develop a method which would allow mapping of channel hydraulics with the same spatial resolution as channel morphology.

CHAPTER IV

VIDEO STRUCTURE-FROM-MOTION: DEVELOPING

A METHOD FOR CONTINUOUS MAPPING OF WATER SURFACES

INTRODUCTION

The analysis and classification of water surfaces is applied in a variety of contexts in the study of fluvial geomorphology, hydrology and ecology. In ecology we have seen recent success in large scale classification of flow types (Amy S. Woodget, Visser, Maddock, & Carbonneau, 2016). These broad classifications do not address the three-dimensional nuance in flow type within the broader classifications of pool, riffle, rapid, and glide. The relationship between channel morphology and water surface patterns, sometimes termed flow biotopes, has been used to define unique habitat units (Harvey & Clifford, 2009; Harvey et al., 2008; Marcus, 2002; Zavadil et al., 2012). Flow biotope theory is founded on the idea that surface flow structures are related to channel morphology and that by identifying different flow structures it is possible to map certain unique habitat types in a fluvial system based on the visible flow characteristics present.

Most mapping applications of biotope concepts have looked at differentiating general hydraulic classifications such as riffles, runs, pools and glides with airborne or satellite imagery (Harvey & Clifford, 2009; Marcus, 2002). More recent work has continued to look at reach-scale classification of surface flow types using an unmanned aerial vehicle (UAV) and SfM-based approach (Amy S. Woodget et al., 2016). The study by Woodget et al. (2016) shows that there can be accurate classification of different flow

types from surface features. Digital elevation models of the water surface have the potential to make the classification of different flow types more robust.

Three-dimensional water surface elevation information is used in a variety of river applications. Having some form of water surface elevation map is one of the steps in creating 3D riverine topobathymetry via remote sensing; it is the surface from which remotely sensed water depths are subtracted to produce bed elevations (Dietrich, 2016a). Over larger areas and lower resolutions, airborne and satellite-based radar maps of water surfaces are used for monitoring flood inundations and are a critical input to future remote-sensing of river discharges at a global scale (Biancamaria, Lettenmaier, & Pavelsky, 2016). Digital elevation models of surface flow characteristics have the potential to improve computational fluid dynamics models by allowing model results to be directly comparable to high accuracy field data. Among other things, this has the potential to help us improve hydraulic models by allowing the comparison of observed water surface patterns in natural settings and flumes to those generated by hydraulic models. This will also enrich current field calibration techniques which include the 3D flow fields but cannot account for surface hydraulics (Parsapour-Moghaddam & Rennie, 2018) or use morphologic change maps to compute hydraulic conditions which then are used as a check for hydraulic models (Elina, Petteri, Matti, & Hannu, 2013; Grimaldi, Li, Pauwels, & Walker, 2016).

There have been a variety of approaches to mapping water surfaces. These include radar, sonar and camera-based laser distance sensors (CLDS) (Altenau et al., 2017; Flener et al., 2013; Höfle, Vetter, Pfeifer, Mandlbürger, & Stötter, 2009). These approaches are broadly effective at differentiating land, vegetation, and water. However,

they are not capable of mapping small-area variations in water surfaces within the inundated portion of a fluvial system. In addition, many of these approaches rely on active remote sensing which can increase costs (Flener et al., 2013; Milan, Heritage, Large, & Entwistle, 2010) or requires complicated custom-fabricated equipment (Bandini, Jakobsen, Olesen, Reyna-Gutierrez, & Bauer-Gottwein, 2017; English, 2009; Marcus, 2012).

Previous attempts at mapping water surfaces have included using multiple cameras taking a single photograph at the same time, which is termed instantaneous Structure-from-Motion (iSfM) (Dietrich & Fonstad, 2012). These attempts worked well in slow moving systems. However, our initial testing revealed that time gaps between when different cameras captured their images was often long enough for the water surface to change shape sufficiently, thus preventing photogrammetric alignment.

In highly controlled natural and lab based environments there have been some successful experiments using two to three cameras with a wired camera trigger (J. H. Chandler, Ferreira, Wackrow, & Shiono, 2014; J. Chandler et al., 2008; Ferreira, Chandler, Wackrow, & Shiono, 2017). In general, this approach produces accurate models of the moving free-surface. However, extensive set up of the cameras on both sides of the bank and the wired control system limit the size of river areas where these approaches could be used, and likely prevents broader spatial mapping applications. Chandler et al. (2008) and Ferreira et al. (2017) also used seeding of the water surface with biodegradable paper. This improved water surface reconstruction and allowed for the addition of particle image velocimetry computation, but seeding limits the application of their approach more broadly. Even with the success of Chandler, Ferreira and others,

there is a need for a 3D water surface mapping method that is composed of inexpensive, off-the-shelf components, has robustness to changing field mapping conditions, and includes a straightforward process of data capture and analysis.

The objective of our study is to develop a straightforward method for creating reliable digital elevation models of the moving free surface. Our novel approach uses multiple cameras fixed in space relative to each other recording video. We use coincident frames from video taken from each camera which are processed using well-established principles of SfM to create digital elevation models of the moving free surface. We term this new method Video Structure-from-Motion (vSfM). Given the novel approach of our method, we use a progressive approach to developing and testing vSfM, applying it to increasingly complicated surfaces with the ultimate goal of developing a workflow which would allow future researchers to video record thousands of meters of river in order to create continuous 3D water surface map.

RESEARCH DESIGN

Methods Development Strategy:

Traditionally when developing a new method data are validated against an established method. However, there is no accepted standard method for mapping patterns of water surface elevation and roughness at the spatial scale and resolution of vSfM. The moving water surface precludes by-hand in situ measurements as the water surface is inherently transient and therefore hard to measure without disrupting the flow paths. Additionally, standing in swift moving water can present a safety hazard. Our approach

builds on those of Chandler et al. (2008, 2014) and Ferreira et al. (2017) and aims to create a viable workflow which could be implemented in a variety of field settings.

We develop our approach relying on a series of progressive experiments designed to build confidence in the method while checking data quality at each step. Our approach begins with a comparison of photographs vs video frames in a controlled environment. We then develop a method of introducing spatial scale into the model without ground control, which we test on static horizontal surfaces before moving to dynamic surfaces; first a calm pool, then increasingly rough water surfaces. Figure 1 shows our workflow in the development of vSfM.

Our camera array consisted of five GoPro Hero 4 Silver cameras controlled via GoPro's Bluetooth remote (Figure 4). We chose these cameras because they are designed to perform in wet and rugged conditions characteristic of river systems, relatively inexpensive, widely available, and have off-the-shelf remote-control compatibility for up to 50 cameras. Despite the option of higher frame rates, we chose to use 60fps for our videos as it is a widely available frame rate across camera systems. We feel off-the-shelf usability is important to encourage broad application and allows other researches to begin with a relatively small initial investment that can be readily scaled up to more cameras.

Camera Synchronization

Instantaneous Structure-from-Motion as developed by Dietrich and Fonstad (2012) relies on a single photograph from a number of cameras taken simultaneously. When applied to quickly moving water having delays (even microdelays) between the images means the water surface will change and SfM derived 3D surface reconstruction

will be unsuccessful or of poor quality. We informally tested the difference in timing between each camera when triggering a single image by photographing a stopwatch. The results of this experimentation revealed timing discrepancies of up to a second. This led to the development of frame-synced video. We use a “clapperboard” – like used in the motion picture industry to sync audio and video – positioned in front of the array of cameras. Before beginning to record, someone positioned themselves such that the clapperboard was visible in all cameras. After beginning to record video, they closed the clapperboard.

All frames were extracted using the free software *Free Video to JPG Converter* v.5.0.1. (www.free-video-to-jpg-converter.en.softonic.com). After the video was split into individual frames, we determined the frame number of the sync frame. The sync frame is the first frame where the clapperboard is closed as seen in each video. The frame number of the sync frame provides a reference point that allows us to determine which frame number from all videos occurs at the same time. The sync frame ensures that each of the frames used in model reconstruction is from the same point in time, regardless of slight differences in video start time. The individual frames of the video serve as our photographs and can now be processed using standard SfM workflow (Fonstad et al., 2013; M. R. James & Robson, 2012; Westoby et al., 2012). SfM processing used the Agisoft Photoscan Professional v1.4. (AgiSoft, 2019) Before aligning the photos, we added the focal length for the GoPro cameras using the camera settings option in Photoscan to help counteract lens distortion.

Static Surface and Scale Tests

In order to begin our progressive validation of this approach, we first tested the effectiveness of our workflow on static, horizontal surfaces because it allowed us to evaluate our method using the accepted approach of comparing the modeled surface to an independently verifiable truth. We used a best-fit horizontal plane computed in CloudCompare (CloudCompare, 2018) following the assumption that in the model area the surface should be flat.

We also used the test on static, horizontal surfaces to develop an approach to filtering and correcting discrepancies in point location relative to the true surface. As has been examined in previous SfM literature, some error in the z direction and doming, a systematic curving of the modeled surface, were anticipated given the limited number of cameras and the functional necessity that they be close together; in general these doming errors are a function of camera height, camera arrangement and camera properties (M. R. James & Robson, 2014; Javernick, Brasington, & Caruso, 2014). Our camera array set up the cameras in a “W” pattern (Figure 4) to follow best practice for minimizing surface error in SfM. To quantify the quality of the model we examined the severity of doming as indicated by the value of coefficients in a best-fit 2.5D plane and the variance of points in Z as compared to that 2.5D plane (Table 1). Larger vertical variance suggests that more points fall above and below the true surface. The coefficients in the best-fit plane describe the nature of curvature of the plan. Larger coefficients therefore indicate a more heavily domed model and poorer overall model quality.

For a DEM to be analytically meaningful it must have scale. Given the dynamic nature of the water surfaces, ground control is not a viable option. Because our cameras are not equipped with GPS a direct georeferencing approach as described by Carbonneau

and Dietrich (2017) is not possible. As an alternative, we implement an approach based on relative camera distance prior to point cloud generation. Our approach is conceptually similar to direct georeferencing. Rather than back-calculating relative camera locations using GPS coordinates of each photograph to introduce scale, we directly input relative camera positions. Within the PhotoScan workflow we defined the distances between pairs of cameras measured from the camera array. The resulting model is scaled based on the distance between each of the cameras, with the scale being transferred to the model during photo alignment and point triangulation. To determine the accuracy of our relative camera position approach, scale bars were placed on the static surfaces. We compared the known distance between points in X, Y, and Z with the distances measured in the completed model, checking accuracy along X, Y, and Z as well as across axis (figure 3). Here, X refers to the horizontal dimension in the original images and Y refers to the vertical dimension. Relative to the camera array, X parallels the camera orientation and Y begins closest to the camera array and extends away from the camera array.

Dynamic Surface Tests

We applied the method developed for static, horizontal surfaces to dynamic water surfaces, relying on SfM best-practice for minimizing error (M. R. James & Robson, 2012, 2014). We conducted the dynamic surface tests in a progressive manner, increasing water surface complexity with each successful model. The first dynamic surface test looked at a flat water-surface. We included scale bars in the area of focus to further validate scale and we anticipated more complicated lighting as a result of the water surface. After confirming static, horizontal water surfaces resulted in adequate models we

floated a short reach of river so that the camera array and water surface were both moving over an approximately one kilometer reach of the Willamette River in Eugene, Oregon.

The first test of a dynamic surface was flat water. We recorded a short period of video, syncing the cameras as described above. In principle a SfM-based model of a flat surface should be the same regardless of the nature of the surface. This test allowed a direct comparison to the static horizontal surface. A visual check of the camera displays ensured that the camera array was oriented such that the cameras couldn't see through the water to ensure that model reconstruction was of the water surface and not the channel bottom.

The second part of the dynamic test was a down-river test, floating a short reach of the Willamette River in Eugene, Oregon. The section of river we chose included flat sections, riffles, and rapids. For the downriver test we suspended a scale bar visible at the bottom of the frame in each camera so that we could check that our approach to within-model scale worked consistently in a variety of hydraulic conditions. The resulting video was approximately 30 minutes long. For the purposes of this study, we chose specific frames in the video with a variety of hydrologic water surface features, lighting conditions, and water surface glare.

We created water surface models from 10 points in time from the downriver float portion of the test. The first four models were built from carefully selected photosets which did not have glare, had good visual contrast of the water surface, and represented flat water, glides, riffles, and rapids. The second set of six models were built using photosets based on a randomly selected frames from the total number of frames extracted from the movie (>100,000 frames). All models had similar issues with doming and noise

as those seen in the static surface models. We followed the process outlined in the *Point Cloud Post-Processing* section (below) to remove doming and vertical noise successfully for all models.

In-situ measurements of the hydrologic features we measured was not possible or safe. However, it is crucial to be able to demonstrate that the water surfaces models we created are a function of the water surface itself and not random noise in the point cloud. To achieve this, we compared water surface models separated by 2 frames (1/30th of a second). From the extracted frames, the major water surface form doesn't visually appear to change perceptibly over this time scale suggesting that the models should be nearly identical. To test the effectiveness of our model we compared three water surfaces, each separated by two frames. A mesh of the point cloud in the middle of the set was created, leaving the other two (-2 frames and +2 frames) as point clouds. To assess the effectiveness of our approach, we computed signed distances between the point cloud and the reference mesh.

Point Cloud Post-Processing

As expected, the limited number of cameras with relatively large lens distortion leads to some surface doming and noise in the surfaces of the models. To generate accurate models, it was necessary to correct for the doming and remove noise in the Z direction of the static and dynamic surfaces. This process was done manually in CloudCompare Version 2.8. The process functions similar to detrending processes used on elevation data because the water surface, on average, should be flat. This step corrects doming in the model by applying the signed vertical offset distance of each point based on its location on the best-fit plane. Figure 5 shows the magnitude of doming before and

after the doming correction process. The vertical relationship between any two points along the Z-axis is maintained so that water surface patterns aren't lost, but neither is the vertical noise relative to the true surface. After the 2.5D transformation it was possible to address noise in the point cloud, defined here as points which fall above or below the true water surface. This presents a relatively simple challenge in flat, horizontal surfaces and a more complex computational challenge as applied to complex water surfaces. The noise filter in Cloud Compare considers the distance between a given point and the underlying surface comprised of the surrounding points. We took any point greater than one standard deviation above or below the estimated surface as noise and the point was removed. This makes it well-suited to filtering out noise in applications where the desired surface is irregular because the number of adjacent points to be considered in constructing the underlying reference surface is user defined.

RESULTS

Our methodologic approach quantified success at each step of vSfM development. For the static and dynamic horizontal surfaces, we gaged success with the standard deviation and mean error in Z from a best-fit horizontal plane as single values and examine their spatial pattern. The severity of doming was estimated by comparing the coefficients of the 2.5D best-fit plane, where larger coefficients indicate a more curved surface (Table 1). To assess accuracy of scale we compared the measured distance between points to the distance between the same points in the model. We considered distances along X, Y, and Z as well as across axes. Our objective was to constrain the magnitude of error given our approach to creating local scale within each model.

Camera Timing

A series of tests with the cameras all facing a stopwatch revealed that the time difference was often less than $1/30^{\text{th}}$ of a second but was sometimes as much as $1/2$ a second. The inconsistent nature of the timing error prevented us from considering vSfM from still photographs as a viable option with current off-the-shelf inexpensive equipment. As such, we switched our approach to shooting video from all the cameras. Each video frame is of lower resolution than the still images, but the temporal rate between each frame is very consistent and precise. The use of video allows us to account for the subtle and unpredictable differences in camera start time and ensure that all of the frames that we used for surface reconstruction all occurred at the same point in time.

In many riffles and rapids, the water surface changed enough in $1/2$ second for surface reconstruction to be unsuccessful. In our tests using the GoPro cameras shooting at 60fps controlled using a Bluetooth remote, the sync-frame frame numbers were within 2-5 frames ($1/30$ - $1/12$ second); however some were as large as 20 frames ($1/3$ second) (Figure 2). This Bluetooth-controlled video start is therefore not simultaneous to the degree required for vSfM, so we retain the clapperboard approach for syncing the video frames from the different cameras.

Flat & Horizontal Surface Results (Static and Dynamic)

Before and after applying the 2.5D transformation we computed the standard deviation of model points in the Z direction to a best-fit plane. For both the static surface and dynamic surface the standard deviation before correction was 0.02 meters. The coefficients of the best-fit plane reached zero after transformation which means that the

surface curvature decreased to negligible (Table 1). In addition, we looked at the spatial distribution of variance in Z. As can be seen in Figure 5, the most variance in the z direction between the model and a best-fit plan were located on the edges of the model where there is little image overlap and therefore poor photogrammetric point alignment which leads to a larger range of vertical error.

The final quality check looked at the effectiveness of using the measured distance between cameras as an input in the SfM model building process as a means of creating scale within the model. We measured distances in X, Y, and Z along and across axes. The maximum error was 0.15 meters and the minimum error was 0.02 meters. Figure 3 shows the field measured and model measured distances. For the static and dynamic horizontal surfaces, error was larger in the direction paralleling the camera look angle, which we termed the Y direction.

Dynamic Surface Results

Dynamic surface model reconstruction was successful for a variety of surfaces including flat moving water (glide), small riffles (wave height <5cm), and rapids with wave heights >50 cm. Additionally, we were able to successfully reconstruct surfaces from images in full sun, shade, and partial shade (Figure 6). Within each model the error in reconstructed scale, as compared to the scale bars, was less than 10%.

Our approach to confirming that the water surfaces we produced were a function of the actual water surface rather than a function of randomness in the point cloud relied on comparing models built from frames +/- 1/30th of a second apart. The results show that the differences between each point cloud and the reference mesh are evenly distributed

across the water's surface. This indicates a random distribution of uncertainty within the model, noise in the Z direction. The nature of the error in the Z direction is also normally distributed around a mean of -0.01 meters for the -2 frames point cloud and the +2 frames point cloud, indicating that within a water surface model points are evenly distributed above and below the true water surface. Figure 7 shows the signed difference between each point cloud and the reference mesh. The lack of systematic differences between a given model (+ or – two frames) and the reference model suggest that patterns of water surface roughness are being accurately represented. Systematic or spatially concentrated differences would suggest that either a large portion of the modeled water surface was actually a function of random error in the modeling process or that the noise reduction process functioned inconsistently.

DISCUSSION

Our work here has shown that by using multiple cameras fixed relative to each other it is possible to reconstruct 3D models of the water surfaces in a variety of hydraulic and lighting conditions. Our scientific approach was designed to progressively build trust in vSfM by assessing model quality at each stage of method development. The progressive approach allowed us to assess and refine fieldwork techniques and point cloud post-processing methods at each step, creating a viable and widely adoptable workflow (Figure 8). In principle, our approach would allow a 3D surfaces to be constructed for every successive frame – yielding 60 3D models per second. This would be an enormous advance in understanding high-temporal resolution changes in earth surface dynamics. However, the automation of the approach to allow this level of truly 4D mapping does not yet exist.

A consistent challenge in vSfM was a result of the limited number of images used to create each model. In Agisoft Photoscan, like most SfM software, the picture the software uses as a starting point for the iterative process of pixel alignment is chosen randomly. When creating models using large photo sets the starting photograph plays a less significant role in model reconstruction. The initial photo is likely to have many adjacent overlapping photographs and thus a larger number of invariant pixels to build the surface model from. When creating a model using only five images, the overlap of images with a sufficiently high degree of overlap to facilitate the initial camera alignment is limited. Given our camera array, the footprint from the middle camera (top row, center) has the highest degree of overlap in field of view with adjacent cameras. In practice, this meant that for some sets of images it was necessary to repeat the initial photo alignment step multiple times until the starting image had sufficient overlap with the adjacent images for there to be enough invariant points for model reconstruction. After successful sparse point cloud creation included all five photographs, we were able to proceed normally as outlined in the methods. Increasing the number of individual cameras within the array would likely solve this problem (M. R. James & Robson, 2014).

Image Composition

Glare off the water surface consistently resulted in poor to no alignment of photos. Glare is a function of the sun–water–camera relationship and occurs when sunlight is scattered off the surface of the water. This results in full saturation of some or part of the image, appearing white. From the models we built, glare only prevented model reconstruction when it comprised more than approximately $1/3^{\text{rd}}$ of the image within two or more of the photographs. When the amount of the image with glare was less than

roughly 1/3rd of the image, we were able to successfully reconstruct models of the water surface by masking out the portion of the image with glare. This did result in an overall decrease in model area. With the camera array mounted on a boat we had some control over the camera – water – sun angle relationship which allowed us to minimize the glare present in the surface by orienting the boat such that the camera’s incidence angle to the water was parallel to that of the sun, that is, the sun behind the cameras. Conducting field work on overcast days with diffuse light would also solve this problem.

In our preliminary tests, we found reconstruction failed where the majority of the image was comprised of fully aerated water. Fully aerated water results in similar photographic issues as glare. The air bubbles refract light and over-saturate the image. In addition, fully aerated water lacks the contrast necessary for SfM to reconstruct depth. Our early testing of vSfM looked specifically at sections of fully aerated, highly turbulent rapids. In all of our attempts to build models of fully aerated rapids, the non-aerated background and foreground portions produced accurate models, but the highly-aerated rapids never produced useful models. Additional research such as employing contrast enhancing pre-processing of images before alignment is needed.

Point Cloud Post-processing

Post-processing of our point clouds was a necessary step in removing the residual doming in the model and decreasing the noise in the Z direction, leaving a clearer model surface. We developed our point cloud post-processing steps on the static and dynamic horizontal surfaces. These surfaces were relatively straightforward in their post-processing, but provided us with an opportunity to develop an effective approach to post-processing because we were able to assume that each surface was flat. This step was

necessary in developing an approach which we could consistently apply to the more complicated dynamic water surfaces.

For all horizontal surfaces the 2.5D transformation resulted in a decrease in all coefficients of the surface with very little change in the standard deviation of points relative to the surface (table 1). This means that detrending the surface was an effective means of removing doming without altering the shape of the point cloud, as indicated by the generally static standard deviation of points. The larger challenge in post-processing of the dynamic water surfaces was in noise reduction. There are a variety of approaches to filtering point cloud data and it continues to be an area of active research (Schall, Belyaev, & Seidel, 2008; Sithole & Vosselman, 2004; Zaman, Wong, & Ng, 2017). We chose a straight-forward algorithm which allows the user to iteratively filter points based on the characteristics of the model. Because our point densities tended to be low, we felt that a filtering algorithm which required user input best. This provides the opportunity for monitoring of data quality during the filtering process. The point cloud filtering stage was the most time intensive, and as such future research would benefit from automation.

Scale

Our approach to creating scale was to use the known distances between cameras in the array. This approach is similar to direct georeferencing proposed by Carbonneau and Dietrich (2017) where the relative positions of each camera are used to scale the model rather than independent ground control. As part of the alignment phase, Photoscan computes relative distances between images. We explicitly input the distance between each image prior to photograph alignment. Model scale is generated in the same way, but doesn't require the back calculation of between-camera distances using GPS data.

The structure of the errors within the model matches what would be expected based on the oblique angle of all cameras to the surface. The ground control targets located nearer the center of the model had errors roughly half those which included targets furthest from the cameras. The error along the X-axis was 0.07 meters and diagonal across the X-Y axes of 0.02 meters. Considering our camera array, the X-axis has the best photogrammetric overlap which leads to the lower errors. In the vertical (Z-axis) direction, the error was 0.1 meters. Because the cameras angle was not nadir there is some foreshortening in the images. The result is that along the Y-axis of the image (the axis with the most severe foreshortening distortion) distances at the top of the image appear further away resulting in a distortion of the model & an overestimation of the true distance. Increasing the height of the camera array above the water, and thus allowing for a more nadir camera angle, would help mitigate this issue.

Surface Tests

Our comparison of three point clouds generated from video frames +/- 1/30th of a second corroborate our qualitative assessment of the quality of the reconstructed water surfaces. Our underlying assumption is that micro-scale differences in the model are a function of micro-scale changes in the water surface or noise in the model. Systematic and concentrated differences in model structure would suggest that model reconstruction wasn't effective or that there were errors in our noise filtering workflow resulting in distortion. The spatial variability of error between the compared and reference point clouds was randomly distributed throughout the overlapping area (figure 7). This is what we would expect when comparing two identical surfaces. If the pattern of error were concentrated in a certain location within the model it would indicate that our

reconstruction of the water surface was not reliable. A systematic error would be indicative of photos capturing the same transient water feature not reproducing the same modeled water surface. Because there were no spatial patterns in the error of our models, we conclude that vSfM does result in high quality models (Figure 7). This analysis also confirms that our noise reduction process is capable of removing some of the unwanted noise from the point cloud without altering the resulting water surface. Had point cloud post-processing steps altered the point cloud to the extent it no longer represented the true water surface it would be apparent as systematic error in our comparison of point clouds. This would likely manifest as a systematic flattening of the overall model as points from wave crests and troughs would be preferentially removed due to the nature of the filtering approach.

Future Work

This work introduces vSfM as a viable approach that relies on a well-established SfM-based surface reconstruction approach to model water surfaces. Refinement of some aspects of the method outlined here are important in encouraging broad application.

As it stands, post-processing of the point clouds to remove doming and reduce noise within the point cloud is a necessary step. It is possible that increasing the number of cameras in the array and increasing the height of the cameras above the water will decrease the need for post-processing. Given our testing we don't see an immediate solution to the necessity of manual post-processing of the point clouds.

Our study looked at a small section of the Willamette River in Oregon. Using the GPS on the boat we were able to manually compute where each water surface model was

within the study area by matching the video time-stamp to the GPS time-stamp. This approach does not result in a viable option for continuous mapping. Video frames do not natively carry the same Exif metadata as still photos from digital cameras. Developing software that would match the GPS location of each video frame based on recording time to the time-stamped on-board GPS, and writing the coordinates to the Exif data within each extracted image would greatly simplify the georeferencing process, and would allow for more streamlined and accurate mapping of water surfaces; leading to the production of water surface elevation maps.

Given the height above the water surface of our cameras, the area of each model is far too small, relative to the size of the test river, for general use in mapping hydraulically-defined habitat unit classification for medium and large rivers. Increasing the camera-to-water surface height with a UAV has the potential to alleviate this issue, allowing the camera array to cover the entire channel. This could be accomplished with a single UAV and a camera array suspended below it on a line, or a small swarm of UAVs flying in unison. For truly continuous mapping of water surface roughness for medium and large rivers, an aerial approach is likely necessary to capture channel width scale patterns of water surface roughness.

CONCLUSION

Currently there are no widely applicable and efficient methods which allow for the accurate mapping of water surfaces with the scale and precision necessary for large-area mapping of patterns of water surface roughness at the scale of waves and other hydraulic features. A robust and easily transferable method for mapping water surfaces would have important implications for hydraulically-defined habitat units, remote sensing

of water depth, and the validation of hydraulic models. Here, we have developed a method for producing accurate DEMs of water surfaces in a variety of hydraulic conditions as well as stream types. Our method is capable of creating scaled models without the use of scale bars or ground control points, which allows it to be implemented in channels where independent scale is unobtainable due to hydraulic conditions.

Despite the success of our method, further development and testing is needed for it to become widely adoptable. The post-processing of the point cloud data is time intensive and challenging to apply without the influence of user subjectivity. Additionally, our approach does not include georeferencing data. Future work using boats and UAVs, using high-precision GPS-enabled cameras, would help introduce the georeferenced data for true water surface mapping. In addition, more experimentation with the point cloud post-processing workflow will be important to improve the quality of the resulting model and decrease the amount of manual manipulation of the point cloud. Automation of the 3D model creation process, applied to successive video frames, would allow truly 4D datasets of changing water (and other earth) surfaces.

Figure 1: The process we used to develop a workflow for vSfM. Each box represents a distinct step in developing the method (e.g. syncing the cameras, optimizing photogrammetric overlap). Within each box, the workflow was iterative until a satisfactory result was attained.

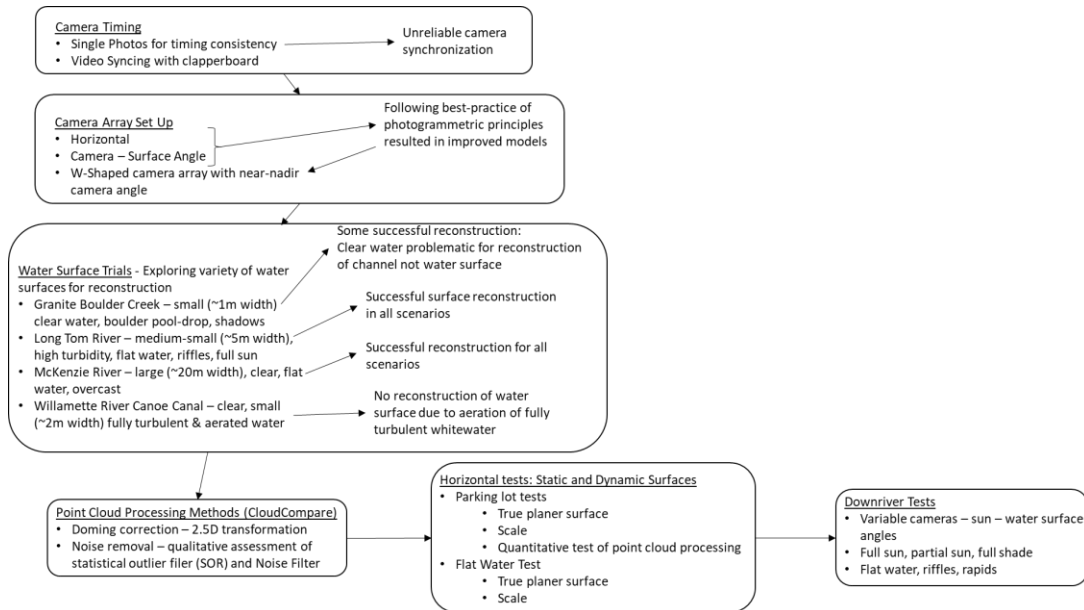


Figure 2: The frequency distribution of differences in sync frames between each of the five GoPro cameras used. Frame differences were computed as the difference in sync frame between any two cameras (eg: C1-C2; C1-C3, C2-C3 etc). In this figure n = 90.

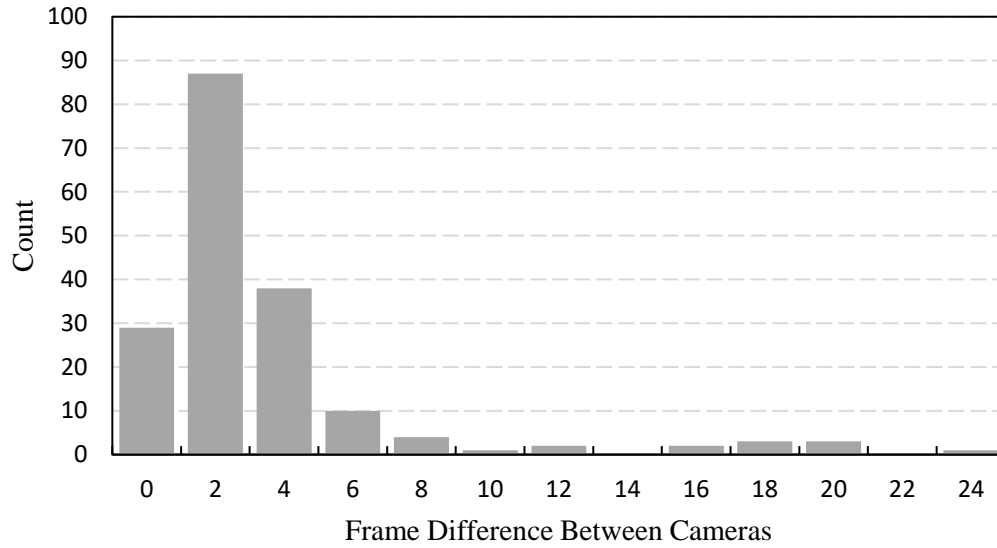


Figure 3: Measured vs modeled distances between ground control targets. The location of each target within the area can be seen below the table.

Ground Control Targets	Known Distance (m)	Model Distance (m)	Difference (m)
16-36	1.4	1.38	0.02
16-22	2.12	1.99	0.13
16-13	2.55	2.48	0.07
13-22	2.08	1.98	0.1
22-36	2.34	2.19	0.15
Ground to scale bar (z)	1.41	1.51	-0.1




Figure 4: Photo of the raft with the W shaped camera array. The top bar is the base for three cameras, and the two vertical poles are the base for the two remaining cameras. The fiberglass poles extending behind the boat hold a meter-long scale bar used to test the scale of resulting water surface DEMs.



Figure 5: This figure looks at the doming within the point cloud before and after the 2.5D doming correction. The top row (A & B) are for the static surface. The lower row (C & D) are for the flat water surface. Note difference in spatial scale between A/B and C/D

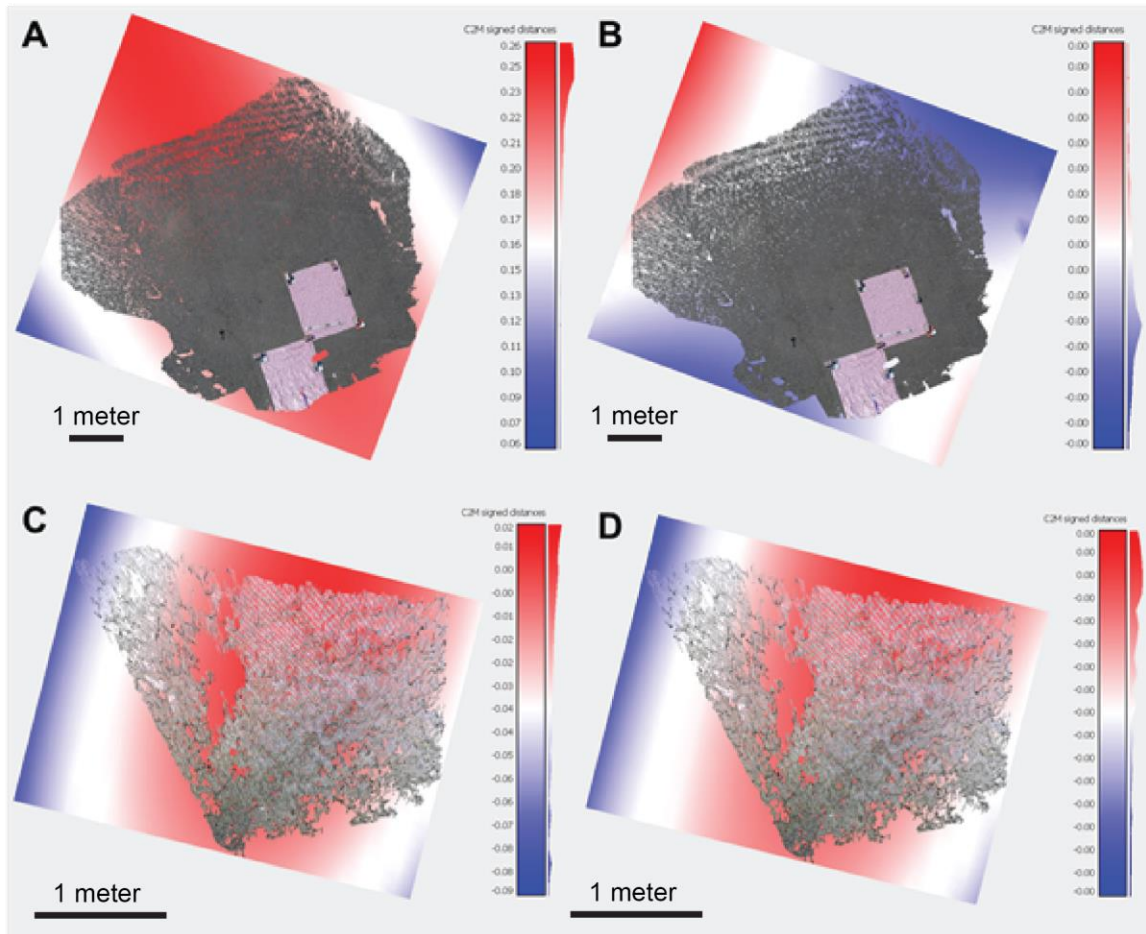


Figure 6: Figures A, B and C are from video used to create water surface models. Images are arranged to match the camera orientation. (A) shows a section of flat water in full sun. (B) shows a partially shaded section with a mean wave height of approximately 0.20 meters. (C) shows a full sun section with wave heights of approximately 0.50 meters. In C, note the back side of the wave has no reconstruction as this wave face was not visible given the camera height and orientation.

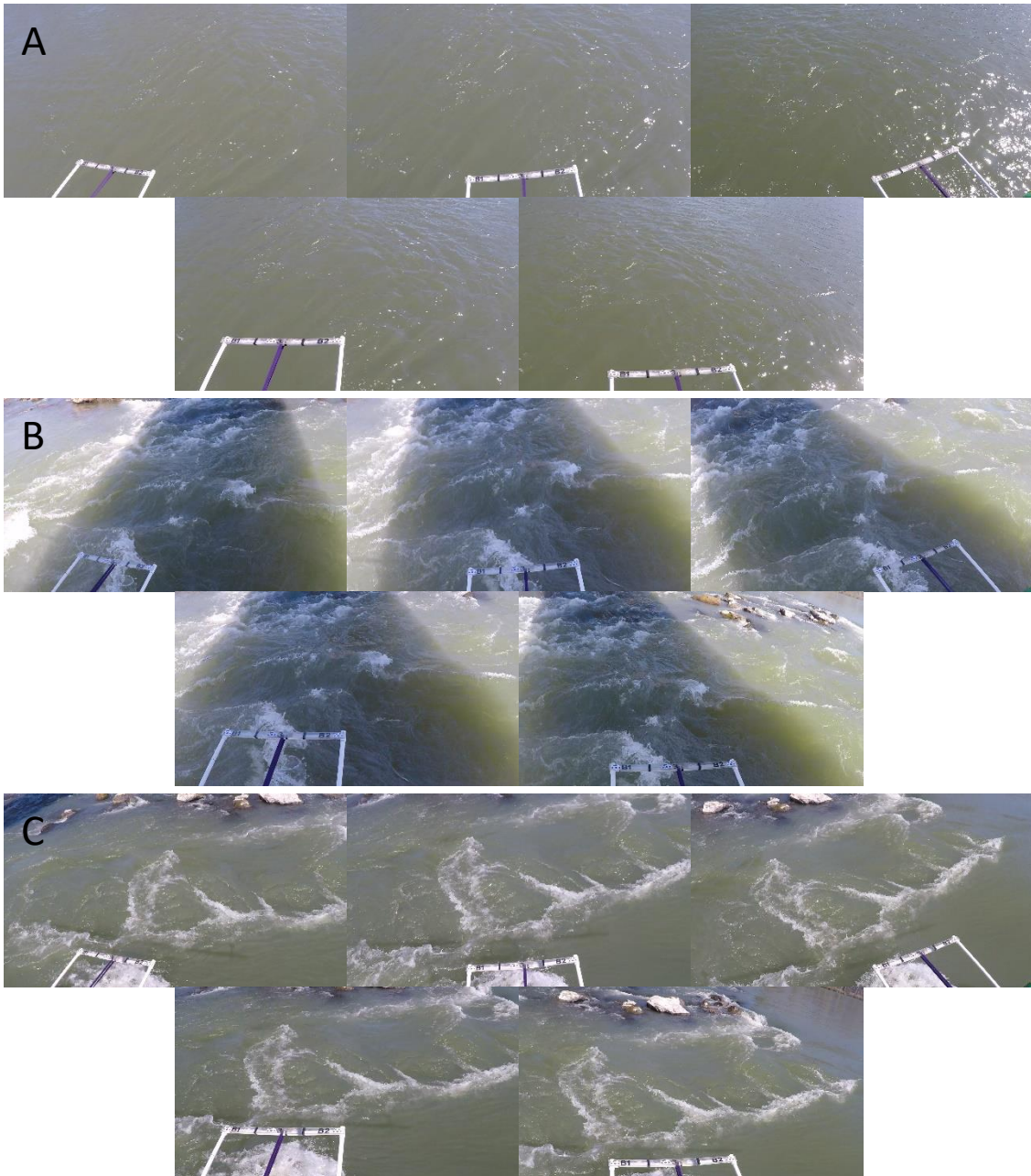
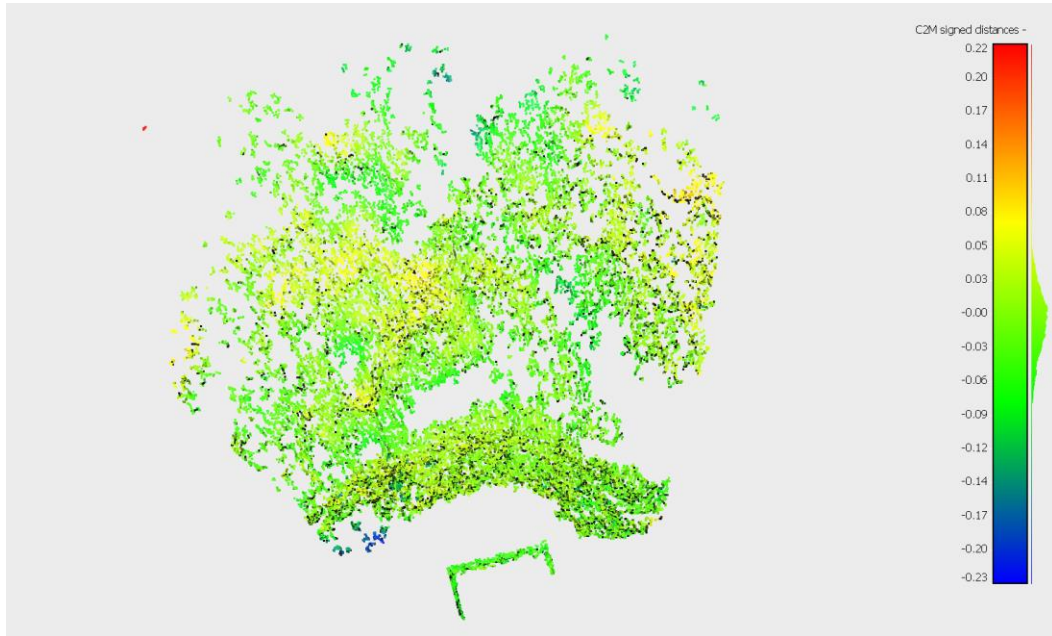


Figure 7: This figure shows the signed distance between the reference mesh and +/- 2 frame point clouds as part of the dynamic surface test from the bank onto the Willamette River. The frequency distribution of the errors is displayed vertically along the color ramp of error values.

+2 Frames



-2 Frames

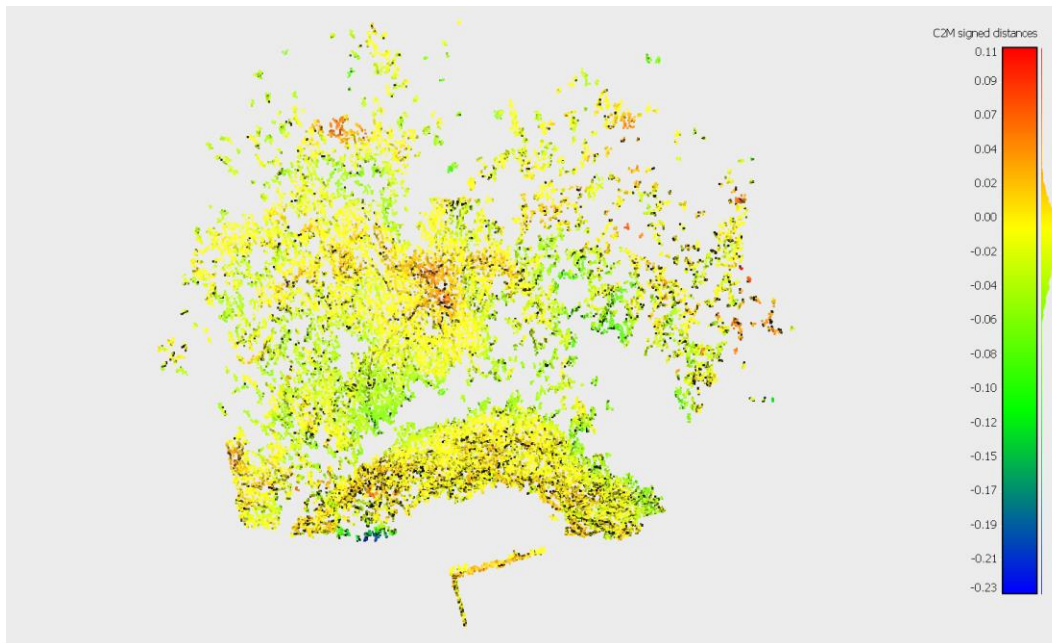


Figure 8: The workflow we recommend using when applying ViSfM in future applications

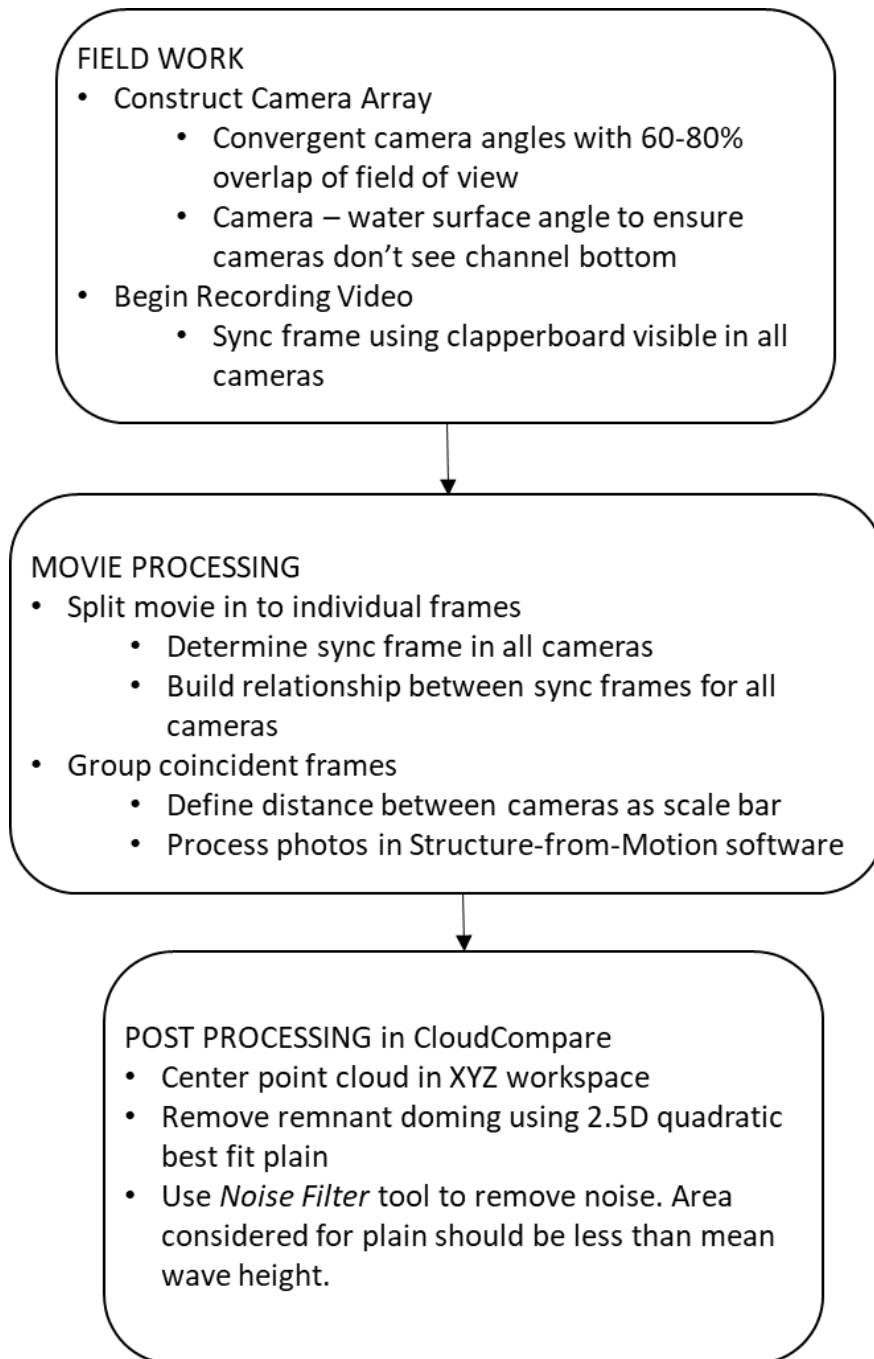


Table 1: 2.5D best fit equations before (Pre) and after (Post) transformation for the static and dynamic horizontal surfaces. Here, we take the coefficients as a metric for the severity of curvature in the surface where the larger coefficients (pre-transformation) indicate more doming of the surface.

Transform	Std Dev Plane	Quadratic Equation
Static Horizontal Surface		
Pre	0.020	$z = 0.02 + -0.001x + 0.001y + -0.002x^2 + -0.004xy + -0.003y^2$
Post	0.010	$z = -3.9e^{-7} + 6.4e^{-8}x + -1.4e^{-8}y + 7.9e^{-8}x^2 + 2.6e^{-8}xy + 2.8e^{-8}y^2$
Horizontal Water Surface		
Pre	0.020	$z = 0.01 + -0.002x + 0.003y + -0.003x^2 + 0.0008xy + -0.0008y^2$
Post	0.020	$z = 3.9e^{-8} + -3.6e^{-8}x + 7.4e^{-9}y + 3.1e^{-8}x^2 + 7.1e^{-8}xy + -6.0e^{-8}y^2$

CHAPTER V: SUMMARY

The goal of this research is to improve our understanding of downstream patterns of channel width, depth, slope, unit stream power and gravel sizes in the context of natural and anthropogenic controlling forces. In addition, this dissertation works to develop a method for mapping water surface roughness at a process scale; the same scale I map morphologic variables. Chapters two and three of this dissertation use a combination of field collected Structure-from-Motion (SfM) and depth data, and aerial imagery, LiDAR and NED data to map 200 kilometers of channel width, depth and slope on the Rogue River. The SfM data was used to compute gravel sizes for all exposed gravel bars in the study area. Chapter four sought to develop a novel method for generating maps of patterns of water surface roughness at the spatial scale of the hydraulic processes responsible for waves, riffles, and holes. The goal was to be able to map hydraulic process with the same spatial resolution as we measure channel morphology. Chapter four was grounded in the common application of SfM, but rather than relying on a single camera moving through space collecting photographs multiple cameras recording video were used. Individual frames were separated and those were used to create the maps of water surface roughness following the standard SfM processing workflow.

The spatially intensive and extensive dataset generated offered insight into how channel form may change at the scale of lateral channel constrictions hundreds of meters long to individual gravels comprising a gravel bar. What this research revealed is a complex fluvial environment, some of which is explained by the anthropogenic and natural controls included in this research. However, much of the complexity observed

was not directly attributable to confining margins or sediment sources, which suggests that some other mechanism(s) are responsible for channel form. Using data from the hyperscale analysis in Chapter III, I suggest that the timing and dispersion patterns of sediment waves may help explain what is otherwise unexplained heterogeneity.

Taken together, the findings of Chapters II and III serve to explain much of the spatial variation in channel morphology along the Rogue River. Current and historic anthropogenic modification of the fluvial environment combine with tributary, hillslope and geologic processes to form a complex river system. What is not seen in the Rogue River are the clear, large scale longitudinal patterns which are frequently used as the basis by which disturbances to a fluvial system are measured. The findings of Chapters II and III of this dissertation suggest that disturbances should be taken in the context of a wide range of natural variability. Field observations of a riffle sequence at a tributary confluence may appear significant in the field, but statistical analysis could reveal that this local disturbance is not meaningful in the context of the full river. The high-resolution dataset and statistical analysis produced for Chapters II and III, in conjunction with a hyperscale analysis, suggest that the processes responsible for channel form are only partially explained through the sediment links concept. External controls on channel form, such as tributaries or landslides, which we would expect to generate a quantifiable signal in channel form do not always do so. Other processes, such as the movement, dispersion and storage of sediment waves may help explain some of the “missing” signals.

Improvements in the spatial and temporal resolution of geomorphic data sets allows geomorphologists to measure channel form across spatial scales – allowing

empirical observations into form at the computational scale of processes moving individual grains. However, moving from channel form to hydraulics to habitat still proves difficult due to the fundamental gap in spatial resolution between channel form and hydraulic processes. Chapter IV of this dissertation began to develop a method for mapping hydraulic processes, as express through patterns of water surface roughness at the same spatial resolution as the processes which form them.

Future research stemming from this dissertation will further develop our ability to map fluvial environments with high spatial resolution at watershed spatial scales. Through this research I hope to increase our understanding of how natural and anthropogenic external forces operate in conjunction with the natural sorting processes within a channel. This research will potentially have important applications for river restoration practitioners and managers alike. Improved understanding of the mechanics between sediment movement in a channel, and at what spatial scales changes in channel form may be observed, would likely have important implications. Restoration activities such as dam removal frequently release a large sediment wave, and many Stage 0 projects also introduce large volumes of material into the channel. In addition, I hope to continue developing methods for mapping patterns of water surface roughness. Continuing this research is bound to improve our understanding of the relationship between channel form and hydraulic process and improve the effectiveness of hydraulically defined habitat units.

REFERENCES CITED

- AgiSoft PhotoScan Professional (Version 1.4.x) (Software). (2018). Retrieved from <http://www.agisoft.com/downloads/installer/>
- Altenau, E. H., Pavelsky, T. M., Moller, D., Lion, C., Pitcher, L. H., Allen, G. H., ... Smith, L. C. (2017). AirSWOT measurements of river water surface elevation and slope: Tanana River, AK. *Geophysical Research Letters*, 44(1), 2016GL071577. <https://doi.org/10.1002/2016GL071577>
- Archuleta, C. M., Constance, E. W., Arundel, S. T., Lowe, A. J., Mantey, K. S., & Phillips, L. A. (2017). U.S. Geological Survey, The National Map, 3DEP products and services: The National Map. <https://doi.org/https://doi.org/10.3133/tm11B9>.
- Archuleta, C. M., Constance, E. W., Lowe, A. J., Mantey, K. S., & Phillips, L. A. (2017). The National Map Seamless Digital Elevation Model Specifications. In U.S. Geological Survey Techniques and Methods, Book 11.
- Bagnold, R. A. (1966). An Approach to the sediment Transport Problem from General Physics. USGS Professional Paper, 422-J.
- Bandini, F., Jakobsen, J., Olesen, D., Reyna-Gutierrez, J. A., & Bauer-Gottwein, P. (2017). Measuring water level in rivers and lakes from lightweight Unmanned Aerial Vehicles. *Journal of Hydrology*, 548, 237–250. <https://doi.org/10.1016/j.jhydrol.2017.02.038>
- Bedient, P. B., & Huber, W. C. (2002). *Hydrology and Floodplain Analysis*. Prentice-Hall, Inc., Upper Saddle River.
- Biancamaria, S., Lettenmaier, D. P., & Pavelsky, T. M. (2016). The SWOT Mission and Its Capabilities for Land Hydrology. *Surveys in Geophysics*. <https://doi.org/10.1007/s10712-015-9346-y>
- Blanton, P., & Marcus, A. W. (2009). Railroads, roads and lateral disconnection in the river landscapes of the continental United States. *Geomorphology*, 112(3–4), 212–227. <https://doi.org/10.1016/j.geomorph.2009.06.008>

- Blanton, P., & Marcus, A. W. (2013). Transportation infrastructure, river confinement, and impacts on floodplain and channel habitat, Yakima and Chehalis rivers, Washington, U.S.A. *Geomorphology*, 189, 55–65.
<https://doi.org/10.1016/j.geomorph.2013.01.016>
- Brandt, S. A. (2000). Classification of geomorphological effects downstream of dams. *Catena*, 40(4), 375–401. [https://doi.org/10.1016/S0341-8162\(00\)00093-X](https://doi.org/10.1016/S0341-8162(00)00093-X)
- Carbonneau, P. E., & Dietrich, J. T. (2017). Cost-effective non-metric photogrammetry from consumer-grade sUAS : implications for direct georeferencing of structure from motion photogrammetry. *Earth Surface Processes and Landforms*, 486(September 2017), 473–486. <https://doi.org/10.1002/esp.4012>
- Carbonneau, P. E., Fonstad, M. A., Marcus, A. W., & Dugdale, S. J. (2012). Making riverscapes real. *Geomorphology*, 137(1), 74–86.
<https://doi.org/10.1016/j.geomorph.2010.09.030>
- Chandler, J. H., Ferreira, E., Wackrow, R., & Shiono, K. (2014). Water surface and velocity measurement-river and flume. *The International Archives of Photogrammetry, Remote Sensing and Spatial Information Sciences*, 40(5), 151.
<https://doi.org/10.5194/isprsarchives-XL-5-151-2014>
- Chandler, J., Wackrow, R., & Sun, X. (2008). Measuring a dynamic and flooding river surface by close range digital photogrammetry. *Silk Road for Information from Imagery*, (January), 211–216. Retrieved from
<http://nora.nerc.ac.uk/4294/2/ChandlerBeijing.pdf>
<http://floodflows.lboro.ac.uk/publications/WaterSurface2JC.pdf>
http://www.isprs.org/proceedings/XXVII/congress/8_pdf/2_WG-VIII-2/09.pdf
<http://nora.nerc.ac.uk/id/eprint/4294>
- Chang, F. J., & Chung, C. H. (2012). Estimation of riverbed grain-size distribution using image-processing techniques. *Journal of Hydrology*, 440–441, 102–112.
<https://doi.org/10.1016/j.jhydrol.2012.03.032>
- CloudCompare (version 2.x) [GPL software]. (2018). Retrieved from
<http://www.cloudcompare.org/>

- Detert, M., Kadinski, L., & Weitbrecht, V. (2018). On the way to airborne gravelometry based on 3D spatial data derived from images. *International Journal of Sediment Research*. <https://doi.org/10.1016/j.ijsrc.2018.02.001>
- Detert, M., & Weitbrecht, V. (2013). User guide to gravelometric image analysis by basegrain. *Advances in Science and Research*, ISBN 978-1(January), 1789–1795.
- Detert, M., & Weitbrecht, V. (2012). Automatic object detection to analyze the geometry of gravel grains—a free stand-alone tool. *River Flow 2012*, (August 2016), 595–600. Retrieved from http://people.ee.ethz.ch/~vawweb/publications/river_engineering_division_vaw/2012_3125.pdf
- Dietrich, J. T. (2016a). Bathymetric Structure from Motion: Extracting shallow stream bathymetry from multi-view stereo photogrammetry. *Earth Surface Processes and Landforms*. <https://doi.org/10.1002/esp.4060>
- Dietrich, J. T. (2016b). Riverscape mapping with helicopter-based Structure-from-Motion photogrammetry. *Geomorphology*, 252, 144–157. <https://doi.org/10.1016/j.geomorph.2015.05.008>
- Dietrich, J. T., & Fonstad, M. A. (2012). Mapping Land and Water Surface Topography with Instantaneous Structure from Motion. In *American Geophysical Union, Fall Meeting*. San Francisco.
- Elina, K., Petteri, A., Matti, V., & Hannu, H. (2013). Spatial and Temporal Distribution of Fluvio-morphological Processes on a Meandering Point Bar During a Flood Event. *Hydrology Research*, 44(6), 1022–1039. <https://doi.org/10.2166/nh.2013.091>
- English, J. T. (2009). Effectiveness of Extracting Water Surface Slopes from LiDAR Data Within the Active Channel. University of Oregon, Eugene, OR. Retrieved from https://scholarsbank.uoregon.edu/xmlui/bitstream/handle/1794/9168/English_John_Thomas_MS_Win09.pdf;sequence=1

- Fausch, K., Torgersen, C., Baxter, C., & Li, H. (2002). Landscapes to Riverscapes: Bridging the Gap between Research and Conservation of Stream Fishes. *BioScience*, 52(6), 483–498. [https://doi.org/10.1641/0006-3568\(2002\)052\[0483:lrbtg\]2.0.co;2](https://doi.org/10.1641/0006-3568(2002)052[0483:lrbtg]2.0.co;2)
- Ferguson, R. I., Cudden, J. R., Hoey, T. B., & Rice, S. P. (2006). River system discontinuities due to lateral inputs: Generic styles and controls. *Earth Surface Processes and Landforms*, 31(9), 1149–1166. <https://doi.org/10.1002/esp.1309>
- Ferreira, E., Chandler, J., Wackrow, R., & Shiono, K. (2017). Automated extraction of free surface topography using SfM-MVS photogrammetry. *Flow Measurement and Instrumentation*. <https://doi.org/10.1016/j.flowmeasinst.2017.02.001>
- Fisher, G. B., Amos, C., Bookhagen, B., Burbank, D., & Godard, V. (2012). Channel widths, landslides, faults, and beyond: The new world order of high-spatial resolution Google Earth imagery in the study of earth surface processes. *The Geological Society of America*, 492(July), 1–22. [https://doi.org/10.1130/2012.2492\(01\)](https://doi.org/10.1130/2012.2492(01)).
- Fisher, G. B., Bookhagen, B., & Amos, C. B. (2013). Channel planform geometry and slopes from freely available high-spatial resolution imagery and DEM fusion: Implications for channel width scalings, erosion proxies, and fluvial signatures in tectonically active landscapes. *Geomorphology*, 194, 46–56. <https://doi.org/10.1016/j.geomorph.2013.04.011>
- Flener, C., Vaaja, M., Jaakkola, A., Krooks, A., Kaartinen, H., Kukko, A., ... Alho, P. (2013). Seamless Mapping of River Channels at High Resolution Using Mobile LiDAR and UAV-Photography. *Remote Sensing*, 5(12), 6382–6407. <https://doi.org/10.3390/rs5126382>
- Fonstad, M. A., Dietrich, J. T., Courville, B. C., Jensen, J. L., & Carbonneau, P. E. (2013). Topographic structure from motion: A new development in photogrammetric measurement. *Earth Surface Processes and Landforms*, 38(4), 421–430. <https://doi.org/10.1002/esp.3366>
- Fonstad, M. A., & Marcus, A. W. (2010). High resolution, basin extent observations and implications for understanding river form and process. *Earth Surface Processes and Landforms*, 35(6), 680–698. <https://doi.org/10.1002/esp.1969>

- Fryirs, K. A., Wheaton, J. M., & Brierley, G. J. (2016). An approach for measuring confinement and assessing the influence of valley setting on river forms and processes. *Earth Surface Processes and Landforms*, 41(5), 701–710. <https://doi.org/10.1002/esp.3893>
- Galice Creek - Oregon Gold Locations. (n.d.). Retrieved from <http://www.oregongold.net/tag/galice-creek/>
- Garcia Lugo, G. A., Bertoldi, W., Henshaw, A. J., & Gurnell, A. M. (2015). The effects of lateral confinement on gravel bed river morphology. *Water Resources Research*, 51, 7145–7158. <https://doi.org/10.1002/2014WR017081>
- Gran, K. B., & Czuba, J. A. (2017). Sediment pulse evolution and the role of network structure. *Geomorphology*, 277, 17–30. <https://doi.org/10.1016/j.geomorph.2015.12.015>
- Gran, K., & Montgomery, D. R. (2001). Downstream Variations in the Width of Bedrock Channels Downstream variations in the width of bedrock channels, 37(April), 1841–1846. <https://doi.org/10.1029/2000WR900393>
- Grant G.E., O'Connor, J., & Safran, E. (2016). Excursions in fluvial (dis)continuity. *Geomorphology*. <https://doi.org/10.1016/j.geomorph.2016.08.033>
- Grant G.E., & Wolff, A. L. (1991). Long-term Patterns of Sediment Transport after Timber Harvest, Western Cascade Mountains, Oregon, USA. *Sedimentation and Stream Water Quality in a Changing Environment: Trends and Explanations*, 203, 31–40.
- Grimaldi, S., Li, Y., Pauwels, V. R. N., & Walker, J. P. (2016). Remote Sensing-Derived Water Extent and Level to Constrain Hydraulic Flood Forecasting Models: Opportunities and Challenges. *Surveys in Geophysics*. <https://doi.org/10.1007/s10712-016-9378-y>

- Han, B., & Endreny, T. A. (2014). River Surface Water Topography Mapping at Sub-Millimeter Resolution and Precision with Close Range Photogrammetry: Laboratory Scale Application. *IEEE Journal of Selected Topics in Applied Earth Observations and Remote Sensing*, 7(2), 602–608.
<https://doi.org/10.1109/JSTARS.2014.2298452>
- Harrelson, C. C., Rawlins, C. L., & Potyondy, J. P. (1994). Stream Channel Reference Sites: An Illustrated Guide to Field Technique. U.S. Forest Service Rocky Mountain Forest and Range Experiment Station General Technical Report RM-245.
- Harvey, G. L., & Clifford, N. J. (2009). Microscale Hydrodynamics and Coherent Flow Structures in Rivers: Implications for the characterization of physical habitat. *River Research and Applications*, 22(June 2008), 1085–1095.
<https://doi.org/10.1002/rra>
- Harvey, G. L., Clifford, N. J., & Gurnell, A. M. (2008). Towards an ecologically meaningful classification of the flow biotope for river inventory, rehabilitation, design and appraisal purposes. *Journal of Environmental Management*, 88(4), 638–650. <https://doi.org/10.1016/j.jenvman.2007.03.039>
- Heitke, J. D., Archer, E. K., & Roper, B. B. (2010). Effectiveness Monitoring for Streams and Riparian Areas: Sampling Protocol for Stream and Channel Attributes. Retrieved from <http://www.fs.fed.us/biology/fishecology/emp>
- Hey, R. D. (1979). Flow Resistance in Gravel-Bed Rivers. *Journal of Hydraulic Division, ASCE*, 105, 365–379.
- Höfle, B., Vetter, M., Pfeifer, N., Mandlbürger, G., & Stötter, J. (2009). Water surface mapping from airborne laser scanning using signal intensity and elevation data. *Earth Surface Processes and Landforms*, 34(12), 1635–1649.
<https://doi.org/10.1002/esp.1853>
- Hugenholtz, C. H., Whitehead, K., Brown, O. W., Barchyn, T. E., Moorman, B. J., LeClair, A., ... Hamilton, T. (2013). Geomorphological mapping with a small unmanned aircraft system (sUAS): Feature detection and accuracy assessment of a photogrammetrically-derived digital terrain model. *Geomorphology*, 194, 16–24. <https://doi.org/10.1016/j.geomorph.2013.03.023>

- Jacobson, R. B., Cron, E. D., & McGeehin, J. P. (1989). Slope Movements Triggered by Heavy Rainfall, November 3-5, 1985, in Virginia and West Virginia. *Geologic Society of America*, 1–13.
- James, L. A., & Marcus, A. W. (2006). The human role in changing fluvial systems: Retrospect, inventory and prospect. *Geomorphology*, 79(3–4), 152–171. <https://doi.org/10.1016/j.geomorph.2006.06.017>
- James, M. R., & Robson, S. (2012). Straightforward reconstruction of 3D surfaces and topography with a camera: Accuracy and geoscience application. *Journal of Geophysical Research: Earth Surface*, 117(3), 1–17. <https://doi.org/10.1029/2011JF002289>
- James, M. R., & Robson, S. (2014). Mitigating systematic error in topographic models derived from UAV and ground-based image networks. *Earth Surface Processes and Landforms*, 39(10), 1413–1420. <https://doi.org/10.1002/esp.3609>
- Javernick, L., Brasington, J., & Caruso, B. (2014). Modeling the topography of shallow braided rivers using Structure-from-Motion photogrammetry. *Geomorphology*. <https://doi.org/10.1016/j.geomorph.2014.01.006>
- Jones, K. L., O'Connor, J. E., Keith, M. K., Mangano, J. F., & Wallick, R. J. (2011). Preliminary assessment of channel stability and bed-material transport in the Rogue River Basin, Southwestern Oregon.
- Knighton, A. D. (1998). *Fluvial Forms and Processes: A New perspective*. Hodder Education.
- Lane, E. W. (1955). Importance of fluvial geomorphology in hydraulic engineering. *Proceedings: American Society of Civil Engineers*, 81(745).
- Langhammer, J., Lendzioch, T., Miřijovskỳ, J., & Hartvich, F. (2017). UAV-based optical granulometry as tool for detecting changes in structure of flood depositions. *Remote Sensing*, 9(3). <https://doi.org/10.3390/rs9030240>

- Leidecker, M. (2015). *The Rogue River - A Comprehensive Guide from Prospect to Gold Beach* (2nd ed.). Sacramento: Idaho River Publications LLC.
- Leopold, L. B., & Maddock, T. J. (1953). *The Hydraulic Geometry of Stream Channels and Some Physiographic Implications*. Geological Survey Professional Paper 252, 57.
- Leopold, L. B., Wolman, M. G., & Miller, J. P. (1992). *Fluvial Processes in Geomorphology*. Dover Publications. [https://doi.org/10.1016/0022-1694\(65\)90101-0](https://doi.org/10.1016/0022-1694(65)90101-0)
- Lisle, T. F. (1987). *Channel Morphology and Sediment Transport in Steepland Streams*. *Erosion and Sedimentation on the Pacific Rim*, 165, 287–298.
- Marcus, A. W. (2002). Mapping of stream microhabitats with high spatial resolution hyperspectral imagery. *Journal of Geographical Systems*, 4, 113–126. <https://doi.org/10.1007/s101090100079>
- Marcus, A. W. (2012). Remote Sensing of the Hydraulic Environment in Gravel-Bed Rivers. In *Gravel-Bed Rivers: Processes, Tools, Environments*. <https://doi.org/10.1002/9781119952497.ch21>
- Milan, D. J., Heritage, G. L., Large, A. R. G., & Entwistle, N. S. J. (2010). Mapping hydraulic biotopes using terrestrial laser scan data of water surface properties. *Earth Surface Processes and Landforms*, 35(8), 918–931. <https://doi.org/10.1002/esp.1948>
- Millidine, K. J., Malcolm, I. A., & Gibbins, C. N. (2010). *The Potential of Digital Photogrammetry for Characterising Streambed Grain-Size Distributions in Fish Habitat Studies: A Feasibility and Limitations Report*. Marine Scotland Science Report, 1–20.
- Montgomery, D. R., & Buffington, J. (1998). Channel processes, classification, and response. In R. J. Naiman & R. E. Bilby (Eds.), *River Ecology and Management* (pp. 13–42). Springer. Retrieved from <http://duff.ess.washington.edu/grg/publications/pdfs/montgomery-buff-1998.pdf>

- Montgomery, D. R., & Buffington, J. M. (1997). Channel-reach morphology in mountain drainage basins. *Bulletin of the Geological Society of America*.
[https://doi.org/10.1130/0016-7606\(1997\)109<0596:CRMIMD>2.3.CO;2](https://doi.org/10.1130/0016-7606(1997)109<0596:CRMIMD>2.3.CO;2)
- Parsapour-Moghaddam, P., & Rennie, C. D. (2018). Calibration of a 3D Hydrodynamic Meandering River Model Using Fully Spatially Distributed 3D ADCP Velocity Data. *Journal of Hydraulic Engineering*, 144(4).
- Paul, M. J., & Meyer, J. L. (2008). Streams in the Urban Landscape. *Urban Ecology*, 207–231. <https://doi.org/doi:10.1146/annurev.ecolsys.32.081501.114040>
- Pechenick, A., Rizzol, D. M., Morrissey, L. A., Garvey, K., Underwood, K., & Wemple, B. (2014). A multi-scale approach to assess the hydrological connectivity of road and stream networks. *Earth and Planetary Science Letters*, 39(July), 1538–1549.
<https://doi.org/10.1002/esp.3611>
- Petts, G. E. (1985). Impounded Rivers: Perspectives for Ecological Management. *Environmental Conservation*, 12(04), 380.
<https://doi.org/10.1017/S0376892900034718>
- Petts, G. E., & Gurnell, A. M. (2005). Dams and geomorphology: Research progress and future directions. *Geomorphology*, 71(1–2), 27–47.
<https://doi.org/10.1016/j.geomorph.2004.02.015>
- Phillips, J. D. (1989). Fluvial Sediment Storage in Wetlands. *Water Resources Bulletin*, 25, 867–873.
- Rice, S. P. (1998). Which tributaries disrupt downstream fining along gravel-bed rivers? *Geomorphology*, 22(1), 39–56. [https://doi.org/10.1016/S0169-555X\(97\)00052-4](https://doi.org/10.1016/S0169-555X(97)00052-4)
- Rice, S. P., & Church, M. (1998). Grain size along two gravel-bed rivers: statistical variation, spatial pattern and sedimentary links. *Earth Surface Processes and Landforms*, 23(4), 345–363. [https://doi.org/10.1002/\(SICI\)1096-9837\(199804\)23:4<345::AID-ESP850>3.0.CO;2-B](https://doi.org/10.1002/(SICI)1096-9837(199804)23:4<345::AID-ESP850>3.0.CO;2-B)

- Rice, S. P., Greenwood, M. T., & Joyce, C. B. (2001). Tributaries, sediment sources, and the longitudinal organization of macroinvertebrate fauna along river systems. *Canadian Journal of Fisheries and Aquatic Sciences*, 58(4), 824–840. <https://doi.org/10.1139/f01-022>
- Rosgen, D. L. (1994). A classification of natural rivers. *Catena*, 22(3), 169–199. [https://doi.org/10.1016/0341-8162\(94\)90001-9](https://doi.org/10.1016/0341-8162(94)90001-9)
- Schall, O., Belyaev, A., & Seidel, H.-P. (2008). Robust filtering of noisy scattered point data. <https://doi.org/10.1109/pbg.2005.194067>
- Schumm, S. A. (1985). Patterns of Alluvial Rivers. *Annual Review of Earth and Planetary Sciences*, 13, 5–27. <https://doi.org/10.1146/annurev.earth.13.1.5>
- Simon, A., & Rinaldi, M. (2006). Disturbance, stream incision, and channel evolution: The roles of excess transport capacity and boundary materials in controlling channel response, 79, 361–383. <https://doi.org/10.1016/j.geomorph.2006.06.037>
- Sithole, G., & Vosselman, G. (2004). Experimental comparison of filter algorithms for bare-Earth extraction from airborne laser scanning point clouds. *ISPRS Journal of Photogrammetry and Remote Sensing*. <https://doi.org/10.1016/j.isprsjprs.2004.05.004>
- Sklar, L. S., Fadde, J., Venditti, J. G., Nelson, P., Aleksandra Wydzga, M., Cui, Y., & Dietrich, W. E. (2009). Translation and dispersion of sediment pulses in flume experiments simulating gravel augmentation below dams. *Water Resources Research*. <https://doi.org/10.1029/2008WR007346>
- Stock, J. D., & Montgomery, D. R. (1999). Geologic constraints on bedrock river incision using the stream power law. *Journal of Geophysical Research: Solid Earth*. <https://doi.org/10.1029/98jb02139>
- Surian, N., & Rinaldi, M. (2003). Morphological response to river engineering and management in alluvial channels in Italy. *Geomorphology*, 50(4), 307–326. [https://doi.org/10.1016/S0169-555X\(02\)00219-2](https://doi.org/10.1016/S0169-555X(02)00219-2)

- Tamminga, A., Hugenholtz, C., Eaton, B., & Lapointe, M. (2015). Hyperspatial Remote Sensing of Channel Reach Morphology and Hydraulic Fish Habitat Using an Unmanned Aerial Vehicle (UAV): A First Assessment in the Context of River Research and Management. *River Research and Applications*, 31(3), 379–391. <https://doi.org/10.1002/rra>
- Thorp, J. H., Flotemersch, J. E., DeLong, M. D., Casper, A. F., Thoms, M. C., Ballantyne, F., ... Haase, C. S. (2010). Linking Ecosystem Services, Rehabilitation, and River Hydrogeomorphology. *BioScience*. <https://doi.org/10.1525/bio.2010.60.1.11>
- Thorp, J. H., Thoms, M. C., & DeLong, M. D. (2006). The riverine ecosystem synthesis: Biocomplexity in river networks across space and time. *River Research and Applications*. <https://doi.org/10.1002/rra.901>
- Vannote, R. L., Minshall, G. W., Cummins, K. W., Sedell, J. R., & Gushing, C. E. (1980). The river continuum concept. *Canadian Journal of Fisheries and Aquatic Sciences*.
- Venditti, J. G., Dietrich, W. E., Nelson, P. A., Wydzga, M. A., Fadde, J., & Sklar, L. S. (2010). Effect of sediment pulse grain size on sediment transport rates and bed mobility in gravel bed rivers. *Journal of Geophysical Research: Earth Surface*. <https://doi.org/10.1029/2009JF001418>
- Westoby, M. J., Brasington, J., Glasser, N. F., Hambrey, M. J., & Reynolds, J. M. (2012). “Structure-from-Motion” photogrammetry: A low-cost, effective tool for geoscience applications. *Geomorphology*, 179, 300–314. <https://doi.org/10.1016/j.geomorph.2012.08.021>
- Wolman, M. G., & Miller, J. P. (1960). Magnitude and Frequency of Forces in Geomorphic Processes. *The Journal of Geology*, 68(1), 54–74. <https://doi.org/10.1086/626637>
- Woodget, A. S., Fyffe, C., & Carbonneau, P. E. (2018). From manned to unmanned aircraft: Adapting airborne particle size mapping methodologies to the characteristics of sUAS and SfM. *Earth Surface Processes and Landforms*, 43(4), 857–870. <https://doi.org/10.1002/esp.4285>

- Woodget, Amy S., Austrums, R., Maddock, I. P., & Habit, E. (2017). Drones and digital photogrammetry: from classifications to continuums for monitoring river habitat and hydromorphology. *Wiley Interdisciplinary Reviews: Water*, 4(4), e1222. <https://doi.org/10.1002/wat2.1222>
- Woodget, Amy S., Visser, F., Maddock, I., & Carbonneau, P. E. (2016). The Accuracy and Reliability of Traditional Surface Flow Type Mapping: Is It Time For A new Method of Characterizing Physical River Habitat? *River Research and Applications*, 32, 1902–1914. <https://doi.org/10.1002/rra>
- Zaman, F., Wong, Y. P., & Ng, B. Y. (2017). Density-based denoising of point cloud. In *Lecture Notes in Electrical Engineering*. https://doi.org/10.1007/978-981-10-1721-6_31
- Zavadil, E. A., Stewardson, M. J., Turner, M. E., & Ladson, A. R. (2012). An evaluation of surface flow types as a rapid measure of channel morphology for the geomorphic component of river condition assessments. *Geomorphology*, 139–140, 303–312. <https://doi.org/10.1016/j.geomorph.2011.10.034>
- Ziliak, S., & McCloskey, D. N. (2008). *The Cult of Statistical Significance: How the Standard Error Costs Us Jobs, Justice, and Lives*. University of Michigan Press.